ABSTRACT

Title of dissertation: QUANTUM GATE AND QUANTUM STATE PREPARATION THROUGH NEIGHBORING OPTIMAL CONTROL

Yuchen Peng, Doctor of Philosophy, 2016

Dissertation directed by: Dr. Frank Gaitan
Laboratory for Physical Sciences
Professor Victor Yakovenko
Department of Physics

Successful implementation of fault-tolerant quantum computation on a system of qubits places severe demands on the hardware used to control the many-qubit state. It is known that an accuracy threshold P_a exists for any quantum gate that is to be used for such a computation to be able to continue for an unlimited number of steps. Specifically, the error probability P_e for such a gate must fall below the accuracy threshold: $P_e < P_a$. Estimates of P_a vary widely, though $P_a \sim 10^{-4}$ has emerged as a challenging target for hardware designers. I present a theoretical framework based on neighboring optimal control that takes as input a good quantum gate and returns a new gate with better performance. I illustrate this approach by applying it to a universal set of quantum gates produced using non-adiabatic rapid passage. Performance improvements are substantial comparing to the original (unimproved) gates, both for ideal and non-ideal controls. Under suitable conditions detailed below, all gate error probabilities fall by 1 to 4 orders of magnitude below the target threshold of 10^{-4}.

After applying the neighboring optimal control theory to improve the performance of quantum gates in a universal set, I further apply the general control theory in a two-step procedure for fault-tolerant logical state preparation, and I illustrate this procedure by preparing a logical Bell state fault-tolerantly. The two-step preparation procedure is as follow: Step 1 provides a one-shot procedure using neighboring optimal control theory to prepare a physical qubit state which is a high-fidelity approximation to the Bell state $|\beta_{01}\rangle = 1/\sqrt{2}\,(|01\rangle + |10\rangle)$. I show that for ideal (non-ideal) control, an approximate $|\beta_{01}\rangle$ state could be prepared with error probability $\epsilon \sim 10^{-6}$ (10^{-5}) with one-shot local operations. Step 2 then takes a block of p pairs of physical qubits, each prepared in $|\beta_{01}\rangle$ state using Step 1, and fault-tolerantly prepares the logical Bell state $\left|\overline{\beta_{01}}\right\rangle$ for the C_4 quantum error detection code.

QUANTUM GATE AND QUANTUM STATE PREPARATION THROUGH NEIGHBORING OPTIMAL CONTROL

by

Yuchen Peng

Dissertation submitted to the Faculty of the Graduate School of the
University of Maryland, College Park in partial fulfillment
of the requirements for the degree of
Doctor of Philosophy
2016

Advisory Committee:
Professor Victor Yakovenko, Chair/Advisor
Dr. Frank Gaitan, Co-Advisor
Professor Christopher Lobb
Professor Frederick Wellstood
Professor Jacob Taylor
Professor Christopher Jarzynski

Preface

The main purpose of this thesis is to study the application of neighboring optimal control (NOC) in quantum computation. Two applications of neighboring optimal control theory are discussed: (i) quantum gate preparation, and (ii) logical quantum state preparation.

The structure of this thesis is as follow. In Chapter 1 I review some background knowledge of quantum computing that are required for the rest of the discussion. The general theory of neighboring optimal control is introduced in Chapter 2, which takes as input a good quantum gate, and returns a new gate with better performance. In Chapter 3 I illustrate the NOC approach by applying it to improve the gate performance of all quantum gates in a universal set produced using a form of non-adiabatic rapid passage, known as twisted rapid passage (TRP). I examine both ideal and non-ideal controls, and show that under suitable conditions, all gate error probabilities fall well below the target gate error probability threshold of 10^{-4}. In Chapter 4 I introduce a two-step procedure for logical quantum state preparation. In Step 1, the general NOC theory is applied to prepare a high-fidelity approximation to a target physical qubit state. Taking these high-fidelity approximated states as input, in Step 2 I then introduce a quantum circuit that fault-tolerantly prepare

the target logical state. I illustrate this procedure by fault-tolerantly prepare a logical Bell state $\left|\overline{\beta_{01}}\right\rangle = 1/\sqrt{2}\left(\left|\overline{01}\right\rangle + \left|\overline{10}\right\rangle\right)$. For completeness, Appendix A briefly reviews the form of the non-adiabatic rapid passage used to produce the initial universal set of quantum gates examined in Chapter 3 and to provide the input nominal control for physical Bell state preparation in Chapter 4, and Appendix B describes the noise model and simulation protocol that are used to examine phase jitter effects in the non-ideal control discussion for both gate preparation and state preparation.

Dedication

To my wife and my parents.

Acknowledgements

The little work I have done during my Ph.D. study would never be possible without the help and support I received from many people. My vocabularies are always too limited to express my gratitude towards them.

First I would like to thank Frank Gaitan, my advisor. Over the past four years, Frank has been providing insightful directions for my research, and endless patience in answering my endless questions. It is a privilege for me to have had the opportunity to work with Frank. From him, I learned the spirit of a scientific researcher.

I would also like to thank Victor Yakovenko, my co-advisor, and Fred Wellstood. Victor and Fred have been giving substantial suggestions on my research projects described in this thesis, which have improved the quality and integrity of this thesis. I am grateful to Chris Jarzynski, Chris Lobb and Jake Taylor, for serving on my dissertation committee and for their valuable advices on my thesis.

The UMD Department of Physics has been a big family and a source of inspiration for me. Special thanks are due to Peter Shawhan, my academic advisor, who has always been there with extraordinary patience and kindness to provide me help and guidance. And to Ted Jacobson. I was the teaching assistant of Ted during

the very first semester of my graduate school and, being a novice back then, Ted taught me the very first lesson about what a real physicist should look like. I also owe thanks to Jane Hessing, Pauline Rirksopa and Jessica Crosby, for helping me through the countless form fillings during my whole graduate school years.

I have been receiving numerous help and support from the colleagues that I worked with at LPS. I would like to thank Charles Tahan for providing the computational resources used to obtain the numerical simulation results of my research projects, and Rusko Ruskov for the many helpful discussions I have with him.

I would like to thank my parents, Xin Peng and Lin Qin. Being a Ph.D. student abroad I was only able to visit them every second year. And each time I come back, I can see that they look apparently older than the last time I saw them. I feel sorry for not being able to accompany them through all these time. Hope that this thesis can make them proud of their son.

I own the most thank you to Chen Li, my wife, and my best friend. Being together with me through all the sunny and stormy days, you are the reason that my life is always robustly beautiful against the ups and downs. And moreover, you make me a better person, and make me want to achieve a better life with you.

Table of Contents

List of Tables

List of Figures

List of Abbreviations

1-Prep	1-Preparation
AWG	Arbitrary Waveform Generators
CBS	Computational Basis States
CNOT	Controlled-NOT
EC	Error Correction
ECC	Error-correcting Code
ED	Error Detection
EOM	Equation of Motion
exRec	Extended Rectangle
FTQC	Fault-tolerance Quantum computing
LPS	Laboratory for Physical Sciences
NOC	Neighboring Optimal Control
QC	Quantum Computation
QECC	Quantum Error-correcting Code
QT	Quantum Teleportation
Rec	Rectangle
TRP	Twisted Rapid Passage
UMD	University of Maryland

Chapter 1: Introduction to Quantum Computation

In computational complexity theory [1,2], an algorithm for solving a particular problem is considered as efficient, if the resources (such as time and hardware) it takes to solve the problem grow polynomially in the size of the input to the problem. A problem is tractable [2] if an efficient algorithm to solve it exists. On the other hand, to solve problems for which no efficient classical algorithms are known, even a relatively small size of inputs would require a huge amount (super-polynomial, typically exponential) of computational resources. A well-known example for such problems is factoring large numbers [3]. In fact, it is the difficulty of this problem that leads to the belief in the security of the famous RSA public-key cryptosystem, as inverting the encryption process of RSA is closely related to the problem of factoring large numbers [4].

Perhaps one of the most amazing recent predictions of quantum mechanics is that quantum systems can be exploited to provide huge computational power in certain situation. That is, by making use of quantum properties such as interference and entanglement, a quantum computer could provide an exponential speed-up in solving some problems for which no efficient classical algorithm is known. Examples for such speed-up include Shor's algorithm for the problem of factoring large numbers

[5].

The theory of quantum computation involves the study of such computational systems. In the recent decades, proposals on implementation of quantum computation using many different physical systems have been raised, among which are ion traps, optical photons, nuclear spins and superconducting systems [6–9]. With that said, significant technical obstacles still stand in the way towards the goal of building a practical quantum computer. One of the major difficulties is that quantum computers tend to be much more susceptible to errors than classical computers. This is for two reasons. First, modern computer hardwares are extremely reliable, with a typical failure rate below one error in 10^{17} operations [10]. It is presently very hard to control multiple interfering quantum systems to that precision. Second, modern digital computers store information in discrete values of 0 and 1, and achieve considerable fault-tolerance automatically by resetting values back to 0 or 1 depending on which one is closer. In contrast, quantum information is stored in a quantum computer as a state vector that lives in a Hilbert space, and the amplitudes are allowed to take continuous values, thus naively making the digital technique inapplicable.

In this Chapter I review some concepts of quantum computation that are necessary for the discussions in this thesis. Section 1.1 introduces the basic concepts of the circuit model of quantum computation, including qubits, quantum gates and quantum circuits. Following that, Section 1.2 defines the concept of universal set of quantum gates, from which a quantum computer being able to execute gates can simulate any quantum computation to any desired accuracy. Section 1.3 then introduces the important concept of fault-tolerant quantum computation [11]. I

give an example of quantum error-correcting code, which protects the data stored in qubit against noise by redundant encoding [12]. I close the Chapter by discussing the quantum threshold theorem. If the quantum gate error probability is below a threshold, the process of error correction will remove more error than was produced, thus ensuring that quantum computation can continue for an arbitrary number of operations. For a more detailed introduction to quantum computation, the reader is referred to Nielsen and Chuang's textbook on quantum computation [10].

1.1 Qubits, Gates, and Circuits

Just as a classical computer is built from a classical digital circuit, a quantum computer is built from a quantum circuit. In this section I briefly review the basic elements of a quantum circuit: the quantum bits, for storing quantum information, and the quantum gates, for manipulating the state of the quantum bits, and describe the diagram notations for the quantum computation circuits.

1.1.1 Quantum Bits

In a classical computer, the basic unit for information storing and processing is bit. A bit can take two discrete values: logical zero 0, or logical one 1. In a quantum computer, the analog for a bit is a *qubit*, short for quantum bit. A single qubit could in principle be realized by any two-level quantum system. A qubit has two basis states, state $|0\rangle$ and state $|1\rangle$, corresponding to logical 0 and logical 1 of a bit, respectively. A common choice is to denote $|0\rangle$ as the ground state of the

system and $|1\rangle$ as an excited state. In addition to these two states, a single qubit can in general be in any quantum superposition of the two basis states:

$$|\psi\rangle = \alpha\,|0\rangle + \beta\,|1\rangle\,. \tag{1.1}$$

where the coefficients α and β are complex numbers satisfying the normalization condition $|\alpha|^2 + |\beta|^2 = 1$. Therefore, the state $|\psi\rangle$ of a qubit is a unit vector in a two-dimensional Hilbert space H_2. The two states $|0\rangle$ and $|1\rangle$ are known as the computational basis states (CBS), which form an orthonormal basis for this vector space. In matrix notion, I write the state $|\psi\rangle$ as

$$|\psi\rangle = \alpha\,|0\rangle + \beta\,|1\rangle = \begin{pmatrix} \alpha \\ \\ \beta \end{pmatrix}, \tag{1.2}$$

where I implicitly write $|0\rangle$ as $(1,0)^T$ and $|1\rangle$ as $(0,1)^T$ (here T represents matrix transpose).

The superposition property is a fundamental difference between a quantum computer and a classical one. The difference between the possible states for a single classical bit and for a single qubit can be visualized using a Bloch sphere (see Figure 1.1). Since a state is normalized, I rewrite the superposition state $|\psi\rangle$ as

$$|\psi\rangle = e^{i\gamma}\left(\cos\frac{\theta}{2}\,|0\rangle + e^{i\phi}\sin\frac{\theta}{2}\,|1\rangle\right), \tag{1.3}$$

where γ, θ, ϕ are real numbers. The overall phase factor $e^{i\gamma}$ can be ignored for a single qubit since it does not have observable effects. On the sphere, a classical bit can only be at either the "north pole" or the "south pole", where $|0\rangle$ and $|1\rangle$ are respectively. In contrast, a qubit can be represented by any point on the entire sphere's surface.

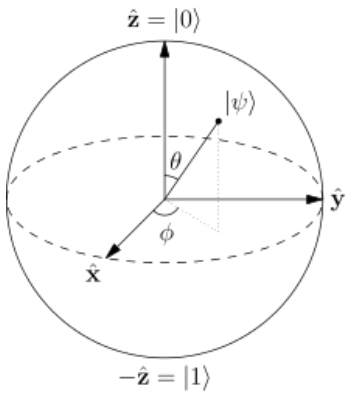

Figure 1.1: The Bloch sphere representation of a qubit [13].

For a two-qubit system, the computational basis states are constructed by taking the direct product of the two single-qubits computational basis states. That is, a two-qubit system has four computational basis states (CBS): $|00\rangle$, $|01\rangle$, $|10\rangle$, $|11\rangle$, where I rewrite $|0\rangle\,|0\rangle$ as $|00\rangle$, $|0\rangle\,|1\rangle$ as $|01\rangle$ and so on. The possible states for a pair of qubits are superpositions of these four computational basis states:

$$|\psi_2\rangle = \alpha_{00}\,|00\rangle + \alpha_{01}\,|01\rangle + \alpha_{10}\,|10\rangle + \alpha_{11}\,|11\rangle\,. \tag{1.4}$$

where the coefficients satisfy the normalization condition $|\alpha_{00}|^2 + |\alpha_{01}|^2 + |\alpha_{10}|^2 + |\alpha_{11}|^2 = 1$. Geometrically, the two-qubit state $|\psi_2\rangle$ is a unit vector in a four dimensional Hilbert space.

In general, for an n-qubit system, where $n \geq 2$, the computational basis states are constructed by taking all possible direct products of the n single-qubit computational basis states:

$$|x_1 x_2 \cdots x_n\rangle = |x_1\rangle \otimes |x_2\rangle \otimes \cdots |x_n\rangle \tag{1.5}$$

where $x_1, \cdots, x_n = 0, 1$. The total number of CBS states for the n-qubit system is 2^n. Therefore, the state space for the n-qubit system is a 2^n dimensional Hilbert

space H_2^n, which is the direct product of the n single-qubit Hilbert space H_2

$$H_2^n = H_2 \otimes H_2 \otimes \cdots \otimes H_2. \tag{1.6}$$

Note that the dimensionality of the state space grows exponentially with the number of qubits. In contrast, for an n-bit classical computer the classical "state space" has dimension n, which only grows linear with the number of bits.

In addition to superposition, another non-trivial property of a quantum system is entanglement [14]. Multiple-qubit states could be classified as separable or non-separable, *i.e.* whether or not the state can be decomposed as a direct product of single-qubit states. For example, the following two-qubit state

$$\frac{1}{2}\left(|00\rangle + |01\rangle + |10\rangle + |11\rangle\right) = \frac{1}{2}\left(|0\rangle + |1\rangle\right)\left(|0\rangle + |1\rangle\right) \tag{1.7}$$

is separable. On the other hand, there are states that cannot be written as direct product of single-qubit states. For instance, the following two-qubit state

$$\frac{1}{\sqrt{2}}\left(|00\rangle + |11\rangle\right) \tag{1.8}$$

cannot be decomposed as the product of single-qubit states. Such a state is said to be entangled. The entangled state in Eq. (1.8) is known as one of the four Bell states. Because of their entanglement property, the Bell states are an essential resource in quantum teleportation [15], which is a key ingredient for some schemes of fault-tolerant quantum computing. I will discuss this in Chapter 4.

Table 1.1: The truth table for the classical two-bit controlled-NOT gate ($CNOT$).

Input	Output
00	00
01	01
10	11
11	10

1.1.2 Quantum Gates

In a classical computer, the information stored in bits is manipulated by logical gates. A logic gate enacts a Boolean function on the information input, converting it to the output result. The action of a logical gate is defined by its truth table. For examples, the truth table for a single-bit gate, the NOT gate X, is simply $0 \to 1$ and $1 \to 0$; on the other hand, for a two-bit gate, the controlled-NOT gate $CNOT$, has truth table showed in Table 1.1.

The analog in a quantum computer is quantum gates. To apply a quantum gate on a qubit, a classical control field $\mathbf{F}(t)$ is applied to the qubit for a chosen time T. The evolution of the qubit state $|\psi\rangle$ is then governed by Schrodinger equation

$$i\hbar \frac{d}{dt} |\psi(t)\rangle = H[\mathbf{F}(t)] |\psi(t)\rangle , \tag{1.9}$$

where $H[\mathbf{F}(t)] = H(t)$ is the Hamiltonian. Because of the Schrodinger dynamics, the starting or "input state" of the qubit $|\psi_{in}\rangle$ and the ending or "output state"

$|\psi_{out}\rangle$ are related by a unitary transformation

$$|\psi_{out}\rangle = U\,|\psi_{in}\rangle\,. \tag{1.10}$$

The effect of this unitary transformation is to apply a quantum gate on the input state $|\psi_{in}\rangle$, converting to the output state $|\psi_{out}\rangle$. Therefore, a quantum gate can be represented by a unitary matrix: a 2×2 unitary matrix for single-qubit gate, a 4×4 unitary matrix for two-qubit gate, and so on. Note that this unitarity requirement for quantum gates implies some crucial differences with classical gates: for example, a classical gate may be reversible or irreversible, while all quantum gates must be reversible.

The follow up are examples of a few important quantum gates:

1. The NOT Gate X, which has the same form as the Pauli matrix σ_x:

$$X \equiv \begin{pmatrix} 0 & 1 \\ 1 & 0 \end{pmatrix}. \tag{1.11}$$

The action of the X gate is to interchange the amplitudes of $|0\rangle$ and $|1\rangle$ of the single-qubit input state. Suppose $|\psi\rangle = \alpha\,|0\rangle + \beta\,|1\rangle$ is the input state, the output state from the X gate is

$$X \begin{pmatrix} \alpha \\ \beta \end{pmatrix} = \begin{pmatrix} \beta \\ \alpha \end{pmatrix}. \tag{1.12}$$

Note that the eigenstates for the X gate are $|\pm\rangle \equiv 1/\sqrt{2}(|0\rangle \pm |1\rangle)$, with eigenvalue ± 1, respectively. These two states form another orthonormal basis for the state space, which is know as the X-basis.

2. The Z gate, which has the same form as the Pauli matrix σ_z:

$$Z \equiv \begin{pmatrix} 1 & 0 \\ 0 & -1 \end{pmatrix}. \tag{1.13}$$

The action of the Z gate is to flip the sign of the $|1\rangle$ component of the input single-qubit state, while remaining the $|0\rangle$ component untouched. In other words, the CBS states $|0\rangle$ and $|1\rangle$ are the eigenvector of the Z gate with eigenvalues $+1$ and -1, respectively. Therefore the CBS is also known as the Z-basis.

3. The Hadamard gate H:

$$H \equiv \frac{1}{\sqrt{2}} \begin{pmatrix} 1 & 1 \\ 1 & -1 \end{pmatrix}. \tag{1.14}$$

The action of the Hadamard gate is to perform a transform between the Z basis states and the X basis states: it converts $|0\rangle$ to $|+\rangle = 1/\sqrt{2}, (|0\rangle + |1\rangle)$, and $|1\rangle$ to $|-\rangle = 1/\sqrt{2}(|0\rangle - |1\rangle)$. This action can be visualized using the Bloch sphere representation: the Hadamard gate first performs a rotation on the single-qubitinput state about the $\hat{y}$ axis by 90°, and then another rotation about the $\hat{x}$ axis by 180°.

4. The two-qubit controlled-NOT gate U_{CN}:

$$U_{CN} \equiv \begin{pmatrix} 1 & 0 & 0 & 0 \\ 0 & 1 & 0 & 0 \\ 0 & 0 & 0 & 1 \\ 0 & 0 & 1 & 0 \end{pmatrix} = \frac{1}{2}(I + \sigma_z) \otimes I + \frac{1}{2}(I - \sigma_z) \otimes \sigma_x, \tag{1.15}$$

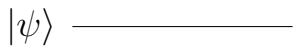

Figure 1.2: The diagram notation of a quantum wire is a straight line, with time progressing from left to right.

where I is the 2×2 identity matrix.

The action of the U_{CN} gate on a two-qubit input state is to use the first qubit as control and the second qubit as target. If the control qubit is in state $|0\rangle$, the target qubit state is left untouched; on the other hand, if the first qubit is in state $|1\rangle$, a NOT gate is acted on the target qubit state.

1.1.3 Quantum Circuits

The basic elements in a quantum circuit are the qubits and the quantum gates. A quantum circuit is an abstract pictural representation of a quantum computation. It is formed by quantum wires which carry quantum information stored in the qubit around, and quantum operations such as quantum gates and measurements that manipulate the quantum information and provide readout [10]. In this subsection I describe the diagram notions for these elements.

Quantum wires are the world lines for qubits. A quantum wire for a single qubit is represented by a single straight line in the circuit diagram, with the initial state on the left, evolving to the right as time progresses (see Figure 1.2).

A *Quantum gate* is usually represented by a square box applied to its target qubits. A little different notation is used for the controlled-U gate, which is a

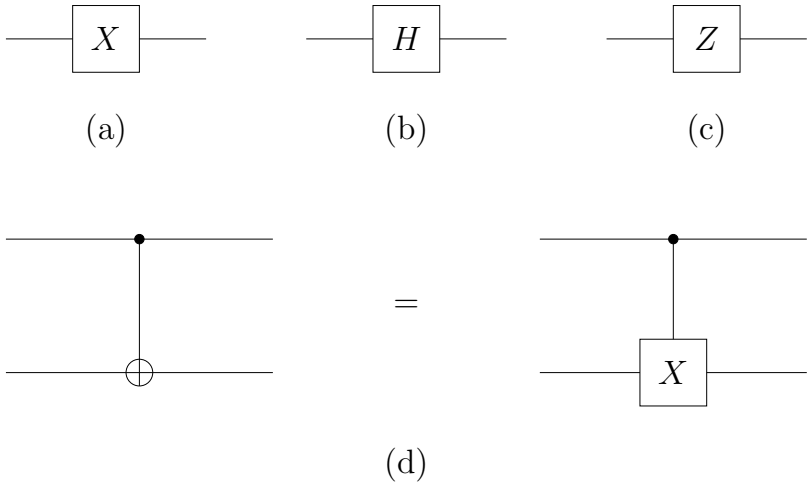

Figure 1.3: The diagram notations of some common quantum gates: (a) the NOT gate X, (b) the Hadamard gate H, (c) the Z gate, and (d) two representations for the controlled-NOT gate U_{CN}.

multiple qubit gate that has several qubits as control and k ($k \geq 1$) qubits as target. An example presented before is the controlled-NOT gate. The action of the controlled-U gate is to apply the gate U to the target qubits if the control qubit is in $|1\rangle$ state, while leaving the target qubits untouched if the control qubit is in $|0\rangle$ state. The diagram notation for a controlled-U gate consists of solid dots on the control qubits, and a boxed gate U on the target qubits, with a straight line connecting the two. Figure 1.3 shows the notation for some common quantum gates.

Quantum measurements. In quantum mechanics, an observable is associated with a Hermitian operator A, *i.e.* $A^\dagger = A$. One can decompose the observable A by its eigenvalues:

$$A \equiv \sum_m \lambda_m |\psi_m\rangle \langle\psi_m| , \tag{1.16}$$

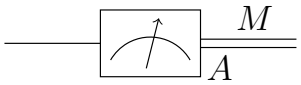

Figure 1.4: The diagram notation of measuring the observable A. The measurement result is represent by M on the double-line.

where λ_m is the m^{th} eigenvalue of the observable A, with corresponding eigenvector $|\psi_m\rangle$.

If one performs a measurement of the observable A on a qubit in state $|\psi\rangle$ (which is sometimes referred as "measure in the A-basis"), the result obtained is a probabilistic value M, whose possible values are the eigenvalues λ_m of A. The probability that measurement result λ_m occurs is given by

$$p(m) = \langle\psi|\ \psi_m\rangle \langle\psi_m|\ \psi\rangle\,, \tag{1.17}$$

and the post-measurement state is given by

$$\frac{\langle\psi_m|\ \psi\rangle\ |\psi_m\rangle}{\sqrt{\langle\psi|\ \psi_m\rangle \langle\psi_m|\ \psi\rangle}} = \frac{\langle\psi_m|\ \psi\rangle\ |\psi_m\rangle}{\sqrt{p(m)}}. \tag{1.18}$$

As shown in Figure 1.4, the diagram notation for measurement in the A-basis is a meter with A at its bottom-right. The result M of measurement is classical information, and the output is distinguished from a qubit state by a double-line wire.

1.2 Universal Set of Quantum Gates

An important concept for classical computers is a universal set of logical gates, which is a set of finite number of logical gates such that every Boolean function can

be implemented using gates in this set. A well-known universal set consists of a two-bit the $NAND$ gate.

For quantum computers, a similar conclusion applies [16]. A finite set $\mathcal{G}_U$ of quantum gates is said to be universal, if an arbitrary quantum gate can be approximated to any precision using a finite series of gates in $\mathcal{G}_U$ [17]. A well-known set [18] of universal quantum gates consists of the Hadamard gate H, the phase gate S, the $\pi/8$ gate T and the two-qubit CNOT gate U_{CN}. The phase gate S and the $\pi/8$ gate T are single qubit gates and are defined as follow:

$$S \equiv \begin{pmatrix} 1 & 0 \\ 0 & i \end{pmatrix}; \quad T \equiv \begin{pmatrix} 1 & 0 \\ 0 & \exp(i\pi/4) \end{pmatrix}. \tag{1.19}$$

In Chapter 3 I discuss a different universal set of quantum gates.

There are two main reasons that people are particularly interested in the universal set of quantum gates rather than an arbitrary quantum gate. First, the computational complexity of a quantum algorithm may be represented by the size of its circuit implementation, in which only gates from a given universal set are allowed. Second, it is sufficient to use the quantum gates in the universal set to implement universal computation. In particular, when the gates are noisy and fault-tolerance is to be studied, it is sufficient to study the fault-tolerant implementation for the quantum gates in the universal set.

1.3 Quantum Error Correction and Fault-tolerant Quantum Computation

So far I have only discussed ideal qubits and quantum operations. The physical implementations of quantum computation devices are subject to various types of errors. A qubit can become thermally equilibrated with the environment and can be subject to phase randomization due to decoherence. These timescales are characterized by the relaxation time T_1 and the decoherence time T_2, respectively. The quantum gates can only be executed with a limited precision, and the quantum measurement may be faulty, and so on. It thus becomes desirable to study whether it is possible to (i) protect the information stored in qubits against noise, and (ii) conduct reliable quantum computation when only a faulty set of universal operations is available. The field of quantum error-correcting codes and fault-tolerant quantum computation has been developed to study this question, and the answer provided is a "yes": in principle, quantum computation can tolerate a finite amount of noise and still retain its computational advantages.

In this Section I review some important results of quantum error correction and fault-tolerant quantum computation. Section 1.3.1 gives an overview of the quantum error correction theory and the stabilizer formalism. Section 1.3.2 reviews the fault-tolerance protocol for quantum computation. And finally, Section 1.3.3 summarizes the results and presents the quantum error threshold theorem.

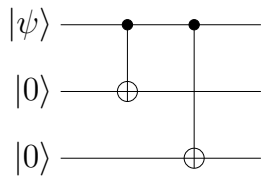

Figure 1.5: The encoding quantum circuit for the 3-qubit bit-flip code.

1.3.1 Quantum error-correcting Codes

Quantum error-correcting codes protect quantum states against noise by encoding them with redundancy. Before going into the conceptual details about the theory, I first illustrate the basic idea of quantum error-correcting codes using a few simple examples.

One important error that could occur to a single-qubit state is the bit-flip error, that the single-qubit state $|\psi\rangle = \alpha|0\rangle + \beta|1\rangle$ is taken to the state $X|\psi\rangle = \alpha|1\rangle + \beta|0\rangle$. One way to protect the information stored in the single-qubit state against bit-flip error is to encode every single-qubit state $|\psi\rangle$ with a corresponding three-qubit logical state $|\overline{\psi}\rangle$. This involves substituting the single-qubit CBS states $|0\rangle$ and $|1\rangle$ with the logical CBS states $|\overline{0}\rangle$ and $|\overline{1}\rangle$ (codewords):

$$|0\rangle \rightarrow |\overline{0}\rangle \equiv |000\rangle\,; \quad |1\rangle \rightarrow |\overline{1}\rangle \equiv |111\rangle\,. \tag{1.20}$$

This encoding process must be done for all superposition states and can be done using the circuit presented in Figure 1.5.

Suppose one perfectly encodes the single-qubit state $|\psi\rangle = \alpha|0\rangle + \beta|1\rangle$ into $|\overline{\psi}\rangle = \alpha|\overline{0}\rangle + \beta|\overline{1}\rangle$. The encoded three-qubit state $|\overline{\psi}\rangle$ is then sent through a noisy channel, in which a single bit-flip error may occur to one of the three qubits

with probability p. The error correction on $\left|\overline{\psi}\right\rangle$ is done by the following two-step procedure:

1. Syndrome measurement: one performs two measurements on the encoded state, the first of the observable $Z_1Z_2 \equiv Z \otimes Z \otimes I$, and the second of the observable Z_2Z_3. Measuring Z_1Z_2 gives $+1$ if the first and second qubits are the same, and -1 otherwise. Similarly, measuring Z_2Z_3 gives $+1$ if the second and third qubits are the same, and -1 otherwise. Therefore this gives four possible syndromes (I use the pair (m_1, m_2), $m_1, m_2 = \pm 1$ to represent the measurement results of Z_1Z_2 and Z_2Z_3). Then, to $\mathcal{O}(p)$

$$\begin{aligned} &(+1,+1): \text{ no bit-flip error occurs;} \\ &(+1,-1): \text{ bit-flip error occurs to the third qubit;} \\ &(-1,+1): \text{ bit-flip error occurs to the first qubit;} \\ &(-1,-1): \text{ bit-flip error occurs to the second qubit;} \end{aligned} \tag{1.21}$$

2. Recovery: once one of the four syndromes is detected, one can apply the proper action to recover the initial state as follow: if the measurement result $(+1,+1)$ occurs, do nothing; if the measurement result $(+1,-1)$ occurs, flip the third qubit by applying X to it; if the measurement result $(-1,+1)$ occurs, flip the first qubit; and if the measurement result $(-1,-1)$ occurs, flip the second qubit.

This error-correction procedure works given that bit-flip error occurs on at most one of the three qubits, which happens with probability $1 - 3p^2 + 2p^3$. The

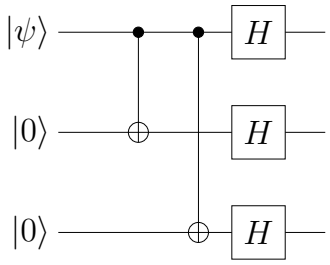

Figure 1.6: The encoding quantum circuit for the 3-qubit phase-flip code.

probability of two or three qubit error occurring, which would not be corrected is $3p^2 - 2p^3$, which is smaller than p if $p < 1/2$. In other words, the error is corrected to $\mathcal{O}(p)$. Therefore, for sufficiently small p ($p < 1/2$), the error-correcting code reduces the error probability from $\mathcal{O}(p)$ to $\mathcal{O}(p^2)$.

Another interesting single-qubit error is the phase-flip error, that the single-qubit state $|\psi\rangle = \alpha|0\rangle + \beta|1\rangle$ is taken to the state $Z|\psi\rangle = \alpha|0\rangle - \beta|1\rangle$, flipping the relative phase between $|0\rangle$ and $|1\rangle$. It can be shown that the bit-flip error and the phase-flip error are related: in the X-basis, the operator Z takes $|+\rangle \equiv (|0\rangle + |1\rangle)/\sqrt{2}$ to $|-\rangle \equiv (|0\rangle - |1\rangle)/\sqrt{2}$, and vice versa, *i.e.* the phase-flip in the Z-basis acts like a bit-flip in the X-basis. Therefore, the error-correcting procedure to protect against phase-flip error works just like that for bit-flip error, but within the X-basis. For example, consider the logical basis states $|\overline{0}\rangle = |+++\rangle$ and $|\overline{1}\rangle = |---\rangle$. The encoding circuit for the phase-flip error-correcting code is presented in Figure 1.6 (recall that the Hadamard gate accomplishes transform between the Z-basis and the X-basis):

The error syndrome measurement and recovery procedure is similar to that for the bit-flip error as well, by replacing Z_1Z_2 with $H^{\otimes 3}Z_1Z_2H^{\otimes 3} = X_1X_2$ and

Z_2Z_3 with $H^{\otimes 3}Z_2Z_3H^{\otimes 3} = X_2X_3$. For example, if the measurement of X_1X_2 yields $+1$ and X_2X_3 yields -1, this indicates a phase-flip occurs on the third qubit, and applying a Z operator to the third qubit recovers the state from the phase-flip error. The phase-flip error-correcting code also corrects phase-flip error to $\mathcal{O}(p)$.

Combining the 3-qubit bit-flip error-correcting code and the 3-qubit phase-flip error-correcting code together, one ends up with a 9-qubit code, known as the Shor code [12]. The codewords of the Shor code are given by

$$\begin{aligned} |0\rangle \to \left|\overline{0}\right\rangle &= \frac{(|000\rangle + |111\rangle)(|000\rangle + |111\rangle)(|000\rangle + |111\rangle)}{2\sqrt{2}}; \\ |1\rangle \to \left|\overline{1}\right\rangle &= \frac{(|000\rangle - |111\rangle)(|000\rangle - |111\rangle)(|000\rangle - |111\rangle)}{2\sqrt{2}}. \end{aligned} \tag{1.22}$$

Figure 1.7 shows the quantum circuit for encoding a single-qubit state $|\psi\rangle$ using the codewords of the Shor code. The encoding process is done via first encoding the single qubit state using the phase-flip code: $|0\rangle \to |+++\rangle$ and $|1\rangle \to |---\rangle$, and then encoding each of these three-qubit states using the bit-flip code: $|+\rangle \to (|000\rangle + |111\rangle)/\sqrt{2}$ and $|-\rangle \to (|000\rangle - |111\rangle)/\sqrt{2}$. By construction, the Shor code is able to detect and correct the single-qubit bit and phase flip errors. I now show that the Shor code protects against an arbitrary single-qubit error.

Assume that an arbitrary error occurs to the i^{th} qubit of the 9-qubit code $\left|\overline{\psi}\right\rangle$, taking it to $E\left|\overline{\psi}\right\rangle$, where E is a unitary operator, which only affects the i^{th} qubit state while leaving the other qubit states untouched. One can expand E as a linear combination of the identity I_i, the bit-flip X_i, the phase-flip Z_i, and the product of bit-flip and phase-flip X_iZ_i:

$$E = e_0I_i + e_1X_i + e_2Z_i + e_3X_iZ_i. \tag{1.23}$$

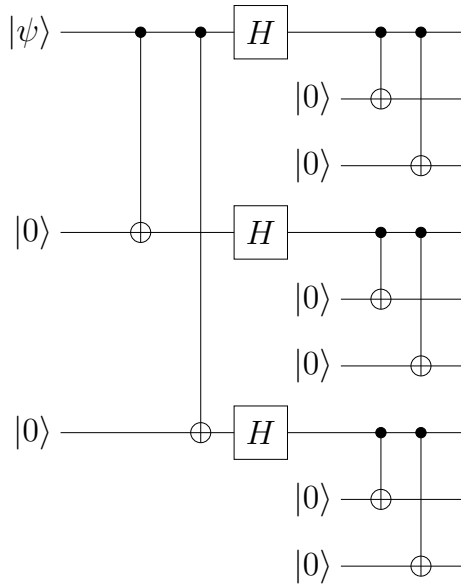

Figure 1.7: The encoding quantum circuit for the Shor code.

The state $E\left|\overline{\psi}\right\rangle$ can thus be written as a superposition of the four states: $\left|\overline{\psi}\right\rangle$, $X_i\left|\overline{\psi}\right\rangle$, $Z_i\left|\overline{\psi}\right\rangle$ and $X_iZ_i\left|\overline{\psi}\right\rangle$. After error syndrome measurement, the post-error state $E\left|\overline{\psi}\right\rangle$ collapses into one of these four states, and one can thus perform corresponding recovery operation to recover the original state $\left|\overline{\psi}\right\rangle$. I note that although the errors can take forms in a continuum, the error-correcting procedure which is able to correct a discrete set of errors, known as the error basis, can correct an arbitrary error that can be written as a linear combination of the error basis. A useful error basis is the n-qubit Pauli group $\mathcal{P}_n$, which consists of the 4^n tensor products of Pauli matrices σ_x, σ_y, σ_z and the 2×2 identity I, together with an overall phase of ± 1 and $\pm i$. Any n-qubit unitary operator could be expressed as a linear combination of the elements in the Pauli group $\mathcal{P}_n$.

I now summarize some conclusions about quantum error-correction illustrated by the examples above. In general, quantum error-correction protects the infor-

mation stored in k-qubit quantum states against a set of error. It does this by encoding them into a quantum error-correcting code, which is a 2^k dimensional subspace C of a 2^n dimensional Hilbert space H_2^n, where $n > k$ to provide redundancy. The subspace C is known as the code space, or the $[n, k]$ error-correcting code, whose basis states are known as the basis codewords. The states in the code space are called the logical states, and the unitary operations on the logical states as the logical gates, to distinguish them from the original unencoded k-qubit states and quantum gates. For example, for a code that encodes k qubits, the logical operator $\overline{Z}_j$, $j = 1, ..., k$ plays the role of a logical Pauli σ_z operator on the j^{th} logical qubit state, if $\overline{Z}_j \left|\overline{x_1, ..., x_{j-1}, 0, x_{j+1}, ..., x_k}\right\rangle = \left|\overline{x_1, ..., x_{j-1}, 0, x_{j+1}, ..., x_k}\right\rangle$, and $\overline{Z}_j \left|\overline{x_1, ..., x_{j-1}, 1, x_{j+1}, ..., x_k}\right\rangle = -\left|\overline{x_1, ..., x_{j-1}, 1, x_{j+1}, ..., x_k}\right\rangle$, where $x_1, ..., x_k = 0, 1$.

Assume that the original (unencoded) state is subject to an error probability of $\mathcal{O}(p)$. After the encoding process, a syndrome measurement is applied to diagnose the type of error that occurs to the code. It is required that different error syndromes label different orthogonal subspaces of the Hilbert space H_2^n, which means (1) that different correctable errors are distinguishable, and (2) that orthogonal codewords $|c\rangle$, $|c'\rangle$ are mapped to orthogonal states $E|c\rangle$, $E|c'\rangle$, so that the erroneous states can be corrected. This requirement is summarized as the quantum error-correction condition: suppose $\{\left|\overline{\psi}_i\right\rangle\}$ are the basis codewords for a quantum code $C(S)$, and $\mathcal{E}$ is a set of unitary operations known as the error set, such that $\forall E \in \mathcal{E}$ can be written as a linear combination of a basis $\{E_a\}$. Then $\mathcal{E}$ is a correctable set of errors

for the code $C(S)$ if the quantum error-correction condition

$$\left\langle \overline{\psi}_i \right| E_a^\dagger E_b \left| \overline{\psi}_j \right\rangle = A_{ab}\delta_{ij} \tag{1.24}$$

holds for all $E_a, E_b \in \{E_a\}$, where A_{ab} is a Hermitian matrix. For a code that is able to correct a set of errors $\mathcal{E}$, once the error syndrome is determined, one can apply an operation corresponding to the error syndrome to reduce the error probability in the output encoded state to $\mathcal{O}(p^{t+1})$, where the error probability p is below a threshold, and t is the number of errors that the code is able to correct. In this subsection I assume that error-correction operations are faultless; in the case that error-correction operations are themselves faulty, a fault-tolerant protocol is required, which is discussed in the following subsection.

Another important concept for a quantum error-correcting code is the distance d. Define the weight of an operator in $\mathcal{P}_n$ to be the number of tensor factors which are not I. The distance d of a code is defined as the minimal weight of operator E, such that the following equation

$$\left\langle \overline{\psi}_i \right| E \left| \overline{\psi}_j \right\rangle = A(E)\delta_{ij} \tag{1.25}$$

is violated, where $\{\overline{\psi}_i\}$ is a basis for the code, and $A(E)$ is a Hermitian matrix independent of i and j. In other words, the distance of a code is the minimum number of single-qubit Pauli operations it takes to get from one codeword to another. By replacing E in Eq. (1.25) by $E_a^\dagger E_b$ which have equal weights t, immediately from Eq. (1.24) it yields that for $t \leq \lfloor (d-1)/2 \rfloor$, the errors $\{E_a\}$ are correctable, where the floor function $\lfloor x \rfloor$ refers to the greatest integer that is no larger than x. Thus,

a code with distance d can correct up to $t = \lfloor (d-1)/2 \rfloor$ errors. A quantum error-correcting code that uses n qubits to encode a k-qubit state, and has distance d, is denoted by $[n, k, d]$. For example, the Shor code shown in the previous example is a $[9, 1, 3]$ error-correcting code.

Describing an error-correcting code by its codewords can be clumsy. Gottesman [19] developed a formalism that is able to provide a compact description of a wide class of quantum codes, known as the stabilizer formalism. To define the stabilizer formalism, I next to review a few essential concepts. A state $|\psi\rangle$ is said to be stabilized by an operator M if it is the eigenstate of M with eigenvalue 1, *i.e.* $M|\psi\rangle = |\psi\rangle$. A stabilizer S is a Abelian subgroup of $\mathcal{P}_n$, such that $\forall M \in S$ and $\forall |\psi\rangle \in C(S)$, then M fixes $|\psi\rangle$, where $C(S)$ is a subspace of H_2^n. For the subspace $C(S)$ to be nontrivial, *i.e.* it contains state other than the null vector $\mathbf{0}$, it is required that $-I \notin S$, which also indicates that $\pm iI \notin S$.

I can now give the formal definition of stabilizer code: let $C(S)$ be a 2^k dimensional non-trivial subspace of H_2^n, which is stabilized by S, then $C(S)$ is called an $[n, k]$ stabilizer code, and S is the stabilizer of $C(S)$.

There is one last concept I need to define: the generators of a group S are a subset of elements of S such that every element of S can be expressed as the product of finitely many generators and their inverse (here I require that the generators are independent, *i.e.* one generator cannot be expressed as the product or inverse of the other generators). For example, for the single-qubit Pauli group P_1

$$\mathcal{P}_1 \equiv \{\pm I, \pm iI, \pm X, \pm iX, \pm Y, \pm iY, \pm Z, \pm iZ\}, \tag{1.26}$$

the generators are simply the Pauli matrices. Given the generators of a group every element in the group can be specified. For an $[n, k]$ stabilizer code $C(S)$, its stabilizer S has $(n-k)$ independent generators $g_1, ..., g_{n-k}$, and I write $S = \langle g_1, ..., g_{n-k} \rangle$.

A merit of the stabilizer formalism is that to specify the error-correction properties of a stabilizer code $C(S)$, it is sufficient to specify the generators g's of its stabilizer S. To see this, I use the $[9, 1, 3]$ Shor code as an example, which has 8 independent generators as shown in Eq. (1.27) below:

$$\begin{aligned}
g_1 &= Z_1 Z_2 I_3 I_4 I_5 I_6 I_7 I_8 I_9 \\
g_2 &= I_1 Z_2 Z_3 I_4 I_5 I_6 I_7 I_8 I_9 \\
g_3 &= I_1 I_2 I_3 Z_4 Z_5 I_6 I_7 I_8 I_9 \\
g_4 &= I_1 I_2 I_3 I_4 Z_5 Z_6 I_7 I_8 I_9 \\
g_5 &= I_1 I_2 I_3 I_4 I_5 I_6 Z_7 Z_8 I_9 \\
g_6 &= I_1 I_2 I_3 I_4 I_5 I_6 I_7 Z_8 Z_9 \\
g_7 &= X_1 X_2 X_3 X_4 X_5 X_6 I_7 I_8 I_9 \\
g_8 &= I_1 I_2 I_3 X_4 X_5 X_6 X_7 X_8 X_9.
\end{aligned} \tag{1.27}$$

Given the generators, the stabilizers $S = \langle g_1, ..., g_8 \rangle$ of the Shor code is fully determined, and the code space $C(S)$ is the two-dimensional subspace that is stabilized by S.

In principle, any two orthonormal vectors in the space $C(S)$ can be chosen as the logical computational basis states, and I determine the logical computational basis states as follow: first, choose the logical $\overline{Z} \in \mathcal{P}_9$, such that $\overline{Z}$ is independent and commutes with all the generators $g_1, ..., g_8$. It can be verified that the following

choice of $\overline{Z}$

$$\overline{Z} = X_1 X_2 X_3 X_4 X_5 X_6 X_7 X_8 X_9 \tag{1.28}$$

satisfies the condition. I then choose the logical computational basis states $|\overline{x}\rangle$, $x = 0, 1$ to be the states with stabilizer

$$\left\langle g_1, ..., g_8, (-1)^x \overline{Z} \right\rangle, \tag{1.29}$$

such that $\overline{Z}\left|\overline{0}\right\rangle = \left|\overline{0}\right\rangle$ and $\overline{Z}\left|\overline{1}\right\rangle = -\left|\overline{1}\right\rangle$. This choice just yields the codewords in Eq. (1.22). In addition, I choose the logical $\overline{X} \in \mathcal{P}_9$ such that $\overline{X}^\dagger \overline{Z}\ \overline{X} = -\overline{Z}$. This condition ensures that $\overline{X}$ has the effect of a NOT gate acting on the encoded state. It can be verified that the following choice of $\overline{X}$

$$\overline{X} = Z_1 Z_2 Z_3 Z_4 Z_5 Z_6 Z_7 Z_8 Z_9 \tag{1.30}$$

satisfies the condition. Thus, by specifying the generators of the stabilizer, the codewords and the logical Pauli operations $\overline{Z}$ and $\overline{X}$ can be determined. Note that another approach to determine the codewords from the generators of the stabilizer is by constructing the following state

$$\left(\sum_{M \in S} M\right) |\psi_9\rangle, \tag{1.31}$$

where $|\psi_9\rangle$ is an 9-qubit state. The state given by Eq. (1.31) is in the code space $C(S)$ for any $|\psi_9\rangle$. To determine the codeword $\left|\overline{0}\right\rangle$, one simply needs a state $|\psi_9\rangle$ such that the state given by Eq. (1.31) is nonzero. A common choice for $|\psi_9\rangle$ is just $|000000000\rangle$. Once $\left|\overline{0}\right\rangle$ is determined, simply acting $\overline{X}$ on $\left|\overline{0}\right\rangle$ gives the other codeword $\left|\overline{1}\right\rangle$.

In addition, to perform the error-correction operation for a stabilizer code, one simply needs to perform measurement of each generator of the stabilizer $g_1, ..., g_{n-k}$. Since elements of the Pauli group either commute or anticommute, a correctable error $E \in \mathcal{P}_n$ either commutes or anticommutes with a generator g, and I define

$$f_g(E) = \begin{cases} 0, \text{ if } [g, E] = 0 \\ 1, \text{ if } \{g, E\} = 1. \end{cases} \tag{1.32}$$

If E occurs to the encoded state, the measurement result of g_l will be $(-1)^{f_{g_l}(E)}$. Measuring each generator gives the error syndrome that corresponds a unique set of errors which act the same on the encoded states. Then, applying the inverse of any error in the set uniquely determined from the error syndrome reduces the error probability in the output encoded state to $\mathcal{O}(p^{t+1})$.

To sum up, an $[n, k, d]$ quantum error-correcting code uses n qubits to encode the k-qubit states, and can correct up to $t = \lfloor (d-1)/2 \rfloor$ errors. The stabilizer formalism provides a compact description for a wide variety of error-correcting codes, and by specifying the generators of the code, the error-correction property of a stabilizer code is fully determined.

1.3.2 Fault-tolerant Conditions

In the previous section I assumed that the process of encoding and error-correction are done perfectly. However, in practice the quantum operations used for encoding and error-correction are themselves subject to error. In addition, if decoding is required for applying quantum gates on the states, the decoded states are again vulnerable to noise during the time they are decoded. Fortunately, the

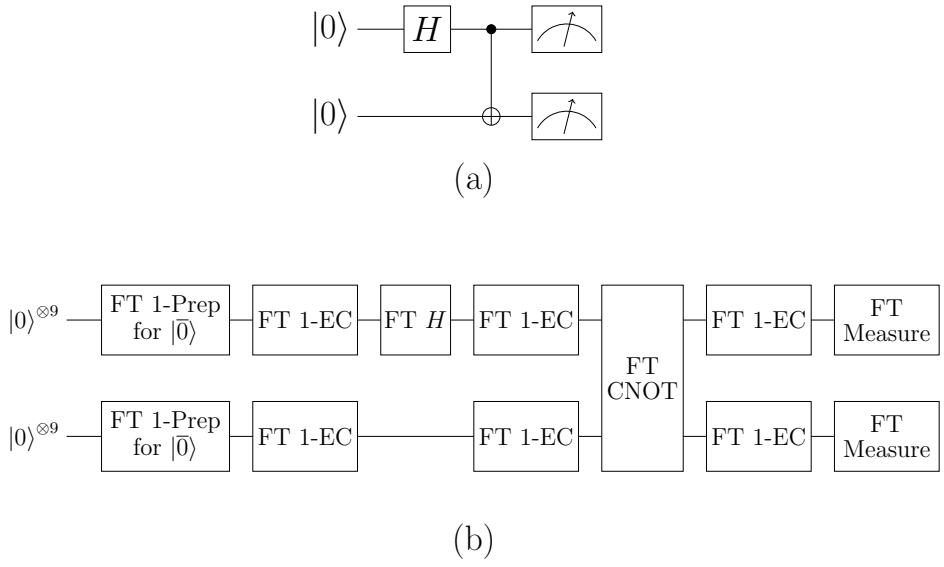

Figure 1.8: Two quantum circuits. (a) This circuit applies physical gates and measurements on the unencoded states; if each component in the circuit fails with probability p, the output is subject to an error probability of order $\mathcal{O}(p)$. (b) A simulation of the same circuit in (a) by applying encoded fault-tolerant 1-gadgets on encoded states using the 9-qubit Shor code. The fault-tolerant procedures ensure that the error probability at the output is of order $\mathcal{O}(p^2)$

theory of fault-tolerant quantum computation shows that under certain conditions, one can perform reliable logical operations directly on the encoded quantum states, even with faulty gates. I now present the conditions that are required for achieving fault-tolerant computation.

The basic idea of fault-tolerant quantum computation [11] is to perform computation by acting with encoded logical quantum gates on the logical quantum states that are encoded using a quantum error-correcting code. That is, on a circuit representation, the original (unencoded) qubit states are replaced by codeblocks encoded using an error-correcting code, and the original (unencoded) gates are replaced by

the encoded gates acting on the encoded states. The encoded gates are designed in such a way, that a single failure on one codeblock does not spread to more than one error in other codeblocks in the circuit. This protocol for applying encoded gates is known as a fault-tolerant procedure. Error-correction is also performed repeatedly on the encoded states, in a fault-tolerant fashion such that the procedure of error-correction does not introduce more errors to the codeblocks than it is able to correct. Similarly, there are fault-tolerant protocols for encoded state preparation and for performing measurements. In general, the encoded operations are implemented by "gadgets" that consist of elementary physical faulty operations (I refer physical operations on unencoded states as level-0 gadgets, and the corresponding encoded operation as level-1 gadgets). The fault-tolerant protocol for any 1-gadget is to design the gadget in such a way that a single error in the gadget produces no more than one error in each codeblocks output from the gadget.

Figure 1.8 illustrates the fault-tolerant protocol for quantum computation by presenting a particular quantum circuit. The first (original) circuit applies unencoded gates and unencoded measurements on the unencoded states, and is not fault-tolerant. The second circuit achieves fault-tolerance by replacing unencoded qubit states with codeblocks encoded using the Shor code, and by replacing the 0-gadgets by the fault-tolerant 1-gadgets.

1.3.3 Quantum Threshold Theorem

As I discussed above, quantum computation can have better robustness to errors than the physical circuits by applying fault-tolerant encoded operations on logical states encoded using a quantum error-correcting code. By recursively applying the fault-tolerant scheme, one can construct a hierarchy of codes within codes [20], in which the codeblock at the higher level is built from logical qubits encoded at the previous level. In addition, for each level of code in the hierarchy, one can construct the corresponding level of gadgets, such that the gadgets at the higher level are constructed by a fault-tolerant procedure that implements the encoded version of the gadgets in the previous level. The code from such a construction is known as the concatenated code. Suppose the failure probability of components at the zeroth (physical) level of a code that corrects t errors is p, then, it can be shown that the failure probability at the first code level is of order $\mathcal{O}(p^{t+1})$, and at the second code level $\mathcal{O}(p^{(t+1)^2})$, and so on. The order of the failure probability grows exponentially with the level of the code hierarchy. This conclusion brings us to the quantum threshold theorem [21]: provided the error probability of the physical hardwares p falls below a threshold P_a, by applying fault-tolerant encoded operations on encoded states using concatenating error-correcting code, quantum computation can be carried out with arbitrarily small error probability.

To summarize, with the development of the theory of quantum error-correcting code and fault-tolerant quantum computation, it is now well-established that reliable quantum computing is possible in principle, even in the presence of decoherence

and imperfect gates [20, 22–28]. In spite of this important result, significant technical obstacles currently stand in the way of building a scalable quantum computer. One major challenge is finding a way to implement a high-fidelity universal set of quantum gates from which an arbitrary quantum computation can be constructed. As specified by the quantum error threshold theorem [21], an accuracy threshold P_a provides a quantitative measure of the accuracy demanded of a quantum gate. Specifically, if a quantum gate is to be used in a reliable quantum computation, the probability P_e that it produces a single error must be less than the accuracy threshold: $P_e < P_a$. The accuracy threshold is a function of the quantum error-correcting code used to protect the computational data, and the fault-tolerant procedures used to control the spread of errors during the computation. Estimates of P_a vary widely, from as small as 10^{-6}, to as large as a few times 10^{-3} [19,29]. Over the years, the value $P_a \sim 10^{-4}$ has emerged as a challenging target for quantum hardware designers. Thus, one of the central problems in quantum control is finding a way to implement a universal set of quantum gates whose gate error probabilities are all less than the threshold value of 10^{-4}, so as to satisfy the condition of the error-threshold theorem to achieve reliable quantum computation.

One of the goals of this thesis is to establish a quantum control profile that is able to produce a universal set of quantum gates with error probabilities falling below the threshold of 10^{-4}. I apply the theory of neighboring optimal control introduced in Chapter 2 to achieve this goal.

Chapter 2: Theory of Neighboring Optimal Control

2.1 Introduction

To perform a quantum gate, a control field $\mathbf{F}(t)$ is applied to a quantum system over a time T ($-T/2 \leq t \leq T/2$), causing a time-varying unitary transformation $U(t)$ to act on the quantum state. When designing a quantum gate, the task is to find the control field $\mathbf{F}(t)$ that applies a target gate U_{tgt} to the quantum state (viz. $U(t = T/2) = U_{tgt}$). In optimal control theory [30], the task is to find a control field profile $\mathbf{F}_*(t)$ that produces a high-fidelity approximation $U(t)$ to the target gate U_{tgt}, while simultaneously minimizing a cost function that depends on the state $U(t)$ and control field $\mathbf{F}(t)$. The control profile $\mathbf{F}_*(t)$ is called the optimal control, and the corresponding unitary $U_*(t)$ is called the optimal (state) trajectory. Note that a perturbation of the dynamics can cause an optimal trajectory and control to become non-optimal. However, if the perturbation is small, the optimal control problem can be linearized about the original optimal solution, and a family of perturbed optimal trajectories determined from a single feedback control law. In the literature this classical perturbed control problem is referred to as neighboring optimal control [31].

In this chapter I will present a general theoretical framework for applying

the neighboring optimal control that takes a good quantum gate $U_0(t)$ as input, and returns a better one $U(t)$. It is assumed that a control field profile $\mathbf{F}_0(t)$ that produces a good approximation $U_0(t = T/2)$ to a target gate U_{tgt} is known. I extend the strategy of neighboring optimal control to the dynamics of a quantum system and use it to determine the control modification $\Delta\mathbf{F}(t)$ that produces an improved approximation $U(t = T/2)$ to the target U_{tgt}. In Section 2.2 I derive the equation of motion for the gate modification $\delta U(t) = U_0^\dagger(t)U(t)$; Section 2.3 constructs the cost function whose minimum determines the optimal gate modification; Section 2.4 varies the cost function to determine the equations that govern the optimization; and Section 2.5 presents two strategies for obtaining their solution. In Section 3 I illustrate the general method by using it to improve the performance of the gates in a universal set of quantum gates.

2.2 Gate modification dynamics

Consider a Hamiltonian $H(t) = H[\mathbf{F}(t)]$, which is a functional of a three-dimensional control field $\mathbf{F}(t) = \mathbf{F}_0(t) + \Delta\mathbf{F}(t)$ that contains a small variation $\Delta\mathbf{F}(t)$ about a nominal control field $\mathbf{F}_0(t)$. Expanding the Hamiltonian $H(t)$ about $\mathbf{F}_0(t)$ gives

$$\begin{aligned} H(t) &= H[\mathbf{F}_0(t)] + \sum_{j=1}^{3} \left.\frac{\delta H}{\delta F_j}\right|_{\mathbf{F}_0} \Delta F_j + \mathcal{O}(\Delta^2) \\ &\equiv H_0(t) + \sum_{j=1}^{3} \mathcal{G}_j \Delta F_j(t) \end{aligned} \tag{2.1}$$

(the second equality holds to the order of $\mathcal{O}(\Delta\mathbf{F}(t))$. Here $\mathcal{G}_j = \delta H/\delta F_j|_{\mathbf{F}_0}$ is an $N \times N$ matrix obtained by taking the functional derivative of $H[\mathbf{F}(t)]$ with respect to $F_j(t)$ evaluated at $\mathbf{F}_0(t)$, and N is the dimension of the Hilbert space. For example, suppose $H(t)$ is the Zeeman Hamiltonian $H(t) = -\boldsymbol{\sigma} \cdot \mathbf{F}(t)$, where the $1, 2, 3$ components of $\boldsymbol{\sigma}$ are the x, y, z Pauli matrices, respectively. Then, a simple calculation gives $\mathcal{G}_j = -\boldsymbol{\sigma}_j$.

The Schrodinger equation for the propagator $U(t)$ is ($\hbar = 1$)

$$i\frac{dU}{dt} = H[\mathbf{F}(t)]U. \tag{2.2}$$

For $H(t) = H[\mathbf{F}(t)]$, the propagator $U(t)$ becomes a functional of the control field $\mathbf{F}(t)$. Throughout this chapter I assume that the nominal control field $\mathbf{F}_0(t)$ acts for a time $-T/2 \leq t \leq T/2$ and gives rise to a propagator $U_0(t)$ via

$$i\frac{dU_0}{dt} = H_0(t)U_0, \tag{2.3}$$

which provides a good approximation $U_0(t = T/2)$ to a target gate U_{tgt} [32].

I now introduce the gate modification $\delta U(t)$ by writing $U(t) = U_0(t)\delta U(t)$. Inserting Eq. (2.1) into Eq. (2.2), and substituting for $U(t)$ gives

$$i\frac{d}{dt}(U_0\delta U) = \left[H_0(t) + \sum_{j=1}^{3} \mathcal{G}_j \Delta F_j(t)\right] U_0\delta U + \mathcal{O}(\Delta^2). \tag{2.4}$$

Inserting Eq. (2.3) into Eq. (2.4) gives the equation of motion for $\delta U(t)$:

$$\begin{aligned} i\frac{d}{dt}\delta U &= \left[\sum_{j=1}^{3} \left(U_0^\dagger \mathcal{G}_j U_0\right) \Delta F_j\right] \delta U + \mathcal{O}(\Delta^2) \\ &= \left[\sum_{j=1}^{3} \overline{G}_j \Delta F_j\right] \delta U. \end{aligned} \tag{2.5}$$

Here $\overline{G}_j = U_0^\dagger(t)\mathcal{G}_j U_0(t)$ is an $N \times N$ matrix. The initial condition for Eq. (2.5) is $\delta U(-T/2) = I$, which follows from the definition of $\delta U(t)$ and $U(-T/2) = U_0(-T/2) = I$. By assumption, $U_0(t)$ already gives a good approximation to the target gate U_{tgt}, and so I look for a gate modification $\delta U(t)$ that is close to the identity:

$$\delta U(t) = I - i\delta A(t) + \mathcal{O}(\Delta^2). \tag{2.6}$$

Note that $\delta A(t)$ is Hermitian, and $\delta A(-T/2) = 0$. Substituting this expression for $\delta U(t)$ into Eq. (2.5) gives

$$\frac{d}{dt}\delta A = \sum_{j=1}^{3} \overline{G}_j \Delta F_j + \mathcal{O}(\Delta^2). \tag{2.7}$$

It proves useful to write the $N \times N$ matrix $\delta A(t)$ as an N^2-component column vector $\Delta\mathbf{x}(t)$. This is done by concatenating the columns $\{\delta A_{\bullet,j}(t) : j = 1, \cdots, N\}$ of $\delta A(t)$ into a single column vector:

$$\Delta\mathbf{x}(t) = \begin{pmatrix} \delta A_{\bullet,1}(t) \\ \vdots \\ \delta A_{\bullet,N}(t) \end{pmatrix}. \tag{2.8}$$

I also construct an $N^2 \times 3$ matrix $G(t)$ as follows. First I take each $N \times N$ matrix $\overline{G}_j(t)$ and convert it into an N^2-component column vector $\mathbf{G}_j(t)$ in a similar fashion as $\delta A(t)$. I then insert $\mathbf{G}_j(t)$ into the j-th column of $G(t)$:

$$G(t) = \begin{pmatrix} \vdots & \vdots & \vdots \\ \mathbf{G}_1(t) & \mathbf{G}_2(t) & \mathbf{G}_3(t) \\ \vdots & \vdots & \vdots \end{pmatrix}. \tag{2.9}$$

Finally, I introduce the column vector $\Delta\mathbf{F}(t)$:

$$\Delta\mathbf{F}(t) = \begin{pmatrix} \Delta F_1(t) \\ \Delta F_2(t) \\ \Delta F_3(t) \end{pmatrix}. \tag{2.10}$$

With these definitions, Eq. (2.7) is transformed into the equation of motion for $\Delta\mathbf{x}(t)$:

$$\frac{d}{dt}\Delta\mathbf{x} \;=\; G(t)\Delta\mathbf{F}(t), \tag{2.11}$$

where the rhs is the matrix product of Eqs. (2.9) and (2.10), and the initial condition $\Delta\mathbf{x}(-T/2) = 0$ follows from $\delta A(-T/2) = 0$.

2.3 Dynamical optimization problem

In optimal control theory [30] the problem is to determine a control field profile $\mathbf{F}_*(t)$ that optimizes system performance relative to a set of design criteria. A cost function is introduced that quantifies the degree to which a particular assignment of the control and system variables satisfies these criteria, with an optimal assignment being one of minimum cost [33]. The cost function J used in my gate optimization contains three contributions: (i) a terminal cost J_1 that vanishes when the final propagator $U(t = T/2)$ equals the target gate U_{tgt}; (ii) an integral cost J_2 that insures the control field and state modifications, respectively, $\Delta\mathbf{F}(t)$ and $\Delta\mathbf{y}(t)$ (defined below) remain small at all times; and (iii) a Lagrange multiplier integral cost J_3 that insures the optimization does not violate the Schrodinger dynamics of $\Delta\mathbf{y}(t)$.

1. Terminal cost J_1: As shown in Ref. [34], and summarized in Appendix A,

$$Tr\, P = Tr\left[\left(U^\dagger(T/2) - U_{tgt}^\dagger\right)\left(U(T/2) - U_{tgt}\right)\right], \tag{2.12}$$

is a convenient upper bound on the gate error probability P_e which is clearly minimized when $U(T/2) = U_{tgt}$. I will use it as a terminal cost:

$$J_1 \;=\; Tr\left[\left(U^\dagger(T/2) - U_{tgt}^\dagger\right)\left(U(T/2) - U_{tgt}\right)\right]. \tag{2.13}$$

The cost J_1 enforces the criterion that $U(T/2) = U_{tgt}$ softly, allowing it to be violated, but penalizing violations with non-zero cost. By assumption, $U_0(T/2)$ is a good approximation for U_{tgt}, and therefore

$$U_0^\dagger(T/2)U_{tgt} = I - i\delta\beta + \mathcal{O}(\Delta^2), \tag{2.14}$$

where $\delta\beta$ is a Hermitian matrix. Recall that $U(t) = U_0(t)\delta U(t)$ and $\delta U(t) = I - i\delta A(t) + \mathcal{O}(\Delta^2)$. Expanding J_1 to second order gives:

$$J_1 = Tr\left[\left(\delta A^\dagger(T/2) - \delta\beta^\dagger\right)\left(\delta A(T/2) - \delta\beta\right)\right]. \tag{2.15}$$

By writing $\delta\beta$ as a (constant) N^2-component vector $\Delta\boldsymbol{\beta}$ as was done with $\delta A(t)$ in Eq. (2.8), I re-write J_1 as the product of a row and a column vector

$$J_1 = \left(\Delta\mathbf{x}^\dagger(T/2) - \Delta\boldsymbol{\beta}^\dagger\right)\left(\Delta\mathbf{x}(T/2) - \Delta\boldsymbol{\beta}\right). \tag{2.16}$$

Defining the column vector $\Delta\mathbf{y}(t)$ as

$$\Delta\mathbf{y}(t) = \Delta\mathbf{x}(t) - \Delta\boldsymbol{\beta}, \tag{2.17}$$

J_1 becomes the square-magnitude of $\Delta\mathbf{y}(T/2)$

$$J_1 = \Delta\mathbf{y}^\dagger(T/2)\Delta\mathbf{y}(T/2). \tag{2.18}$$

Note that since $\Delta\boldsymbol{\beta}$ is a constant vector, $\Delta\mathbf{y}(t)$ also satisfies Eq. (2.11):

$$\frac{d}{dt}\Delta\mathbf{y} = G\Delta\mathbf{F}. \tag{2.19}$$

The initial condition for Eq. (2.19) is $\Delta\mathbf{y}(-T/2) = -\Delta\boldsymbol{\beta}$ which follows from Eq. (2.17) and $\Delta\mathbf{x}(-T/2) = 0$. It proves convenient in the following to work with $\Delta\mathbf{y}(t)$ instead of $\Delta\mathbf{x}(t)$.

2. Integral cost J_2: The second cost term J_2 is an integral cost that penalizes large values of $\Delta\mathbf{F}(t)$ and $\Delta\mathbf{y}(t)$ for all times t:

$$J_2 = \int_{-T/2}^{T/2} dt \left[\Delta\mathbf{y}^\dagger(t)Q(t)\Delta\mathbf{y}(t) + \frac{1}{2}\Delta\mathbf{F}^T(t)R(t)\Delta\mathbf{F}(t)\right]. \tag{2.20}$$

Here $Q(t)$ and $R(t)$ are positive-definite Hermitian matrices, but otherwise, are unconstrained [35]. The cost J_2 is minimized by vanishing state and control modifications $\Delta\mathbf{y}(t) = 0$ and $\Delta\mathbf{F}(t) = 0$. Non-vanishing $\Delta\mathbf{y}(t)$ and $\Delta\mathbf{F}(t)$ are allowed to occur, but they are penalized with non-zero cost. Thus J_2 acts to softly enforce the criterion of small state and control modifications.

3. Integral cost J_3: Finally, I require that the optimization obey the Schrodinger dynamics of $\Delta\mathbf{y}(t)$. This criterion is enforced as a hard constraint which cannot be violated by introducing a Lagrange multiplier $\Delta\boldsymbol{\lambda}(t)$ such that:

$$\begin{aligned} J_3 &= \int_{-T/2}^{T/2} dt \left[\Delta\boldsymbol{\lambda}^\dagger(t)\left\{G(t)\Delta\mathbf{F}(t) - \Delta\dot{\mathbf{y}}(t)\right\} + h.\ c.\right] \\ &= -\Delta\boldsymbol{\lambda}^\dagger\Delta\mathbf{y}\Big|_{-T/2}^{T/2} + \int_{-T/2}^{T/2} dt \left[\left(\Delta\boldsymbol{\lambda}^\dagger(t)G(t)\Delta\mathbf{F}(t) + \Delta\dot{\boldsymbol{\lambda}}^\dagger(t)\Delta\mathbf{y}(t)\right)\right. \\ &\qquad\qquad \left. + h.\ c.\right]. \end{aligned} \tag{2.21}$$

Note that I have done an integration by parts in going from the first to the second line; a dot over a symbol indicates a time-derivative; and *h. c.* indicates the Hermitian conjugate of the proceeding term.

4. Total cost J: Combining all three costs gives

$$\begin{aligned} J &= \left[\Delta\mathbf{y}^\dagger(T/2)\Delta\mathbf{y}(T/2) - \Delta\boldsymbol{\lambda}^\dagger(T/2)\Delta\mathbf{y}(T/2)\right] \\ &\quad + \int_{-T/2}^{T/2} dt \left[\Delta\mathbf{y}^\dagger(t)Q(t)\Delta\mathbf{y}(t) + \frac{1}{2}\Delta\mathbf{F}^T R(t)\Delta\mathbf{F}(t)\right] \\ &\quad + \int_{-T/2}^{T/2} dt \left[\left(\Delta\dot{\boldsymbol{\lambda}}^\dagger(t)\Delta\mathbf{y}(t) + \Delta\boldsymbol{\lambda}^\dagger(t)G(t)\Delta\mathbf{F}(t)\right)\right. \\ &\qquad\qquad \left. + h.\ c.\,\right]. \end{aligned} \tag{2.22}$$

As I'll illustrate in Section 2.4, appropriate variation of J gives the equations that govern the optimization, including the feedback control law. Note that I have dropped the $\Delta\boldsymbol{\lambda}^\dagger(-T/2)\Delta\mathbf{y}(-T/2)$ contribution to J that arises from the surface term in Eq. (2.21) as it has zero variation since $\Delta\mathbf{y}(-T/2) = -\Delta\boldsymbol{\beta}$ is a constant with zero variation.

2.4 Euler-Lagrange equations for optimal control

A necessary condition for optimal control is that the first-order variation of the cost function J vanish. This is most easily worked out by taking functional derivatives of J with respect to $\Delta\mathbf{y}(T/2)$, $\Delta\mathbf{y}(t)$, $\Delta\mathbf{F}(t)$, and $\Delta\boldsymbol{\lambda}(t)$, and setting these derivatives equal to zero. This leads to the equations of motion that govern the optimization. It follows automatically from the positive-definite quadratic na-

ture of J that its second-order variation is positive, making the extremum solution found from the first-order variation the desired minimum cost solution.

1. Variation of $\Delta\mathbf{y}(t)$: Taking the functional derivative of J with respect to the surface term $\Delta\mathbf{y}(T/2)$ and setting the result equal to zero gives

$$\Delta\mathbf{y}^\dagger(T/2) - \Delta\boldsymbol{\lambda}^\dagger(T/2) = 0.$$

Solving for $\Delta\boldsymbol{\lambda}(T/2)$ gives:

$$\Delta\boldsymbol{\lambda}(T/2) = \Delta\mathbf{y}(T/2). \tag{2.23}$$

Next, taking the functional derivative of J with respect to $\Delta\mathbf{y}(t)$ and setting the result equal to zero gives

$$\Delta\mathbf{y}^\dagger(t)Q(t) + \Delta\dot{\boldsymbol{\lambda}}^\dagger(t) = 0.$$

Solving for $\Delta\dot{\boldsymbol{\lambda}}(t)$ gives (recall $Q(t)$ is Hermitian):

$$\frac{d}{dt}\Delta\boldsymbol{\lambda}(t) = -Q(t)\Delta\mathbf{y}(t). \tag{2.24}$$

Eqs. (2.23) and (2.24) define an initial value problem for the Lagrange multiplier $\Delta\boldsymbol{\lambda}(t)$, where the "initial" time is $t = T/2$. Note that taking the functional derivative of J with respect to $\Delta\mathbf{y}^\dagger(t)$ or $\Delta\mathbf{y}^\dagger(T/2)$ simply gives the adjoint of these equations and so provides no new information.

2. Variation of $\Delta\mathbf{F}(t)$: Taking the functional derivative of J with respect to $\Delta\mathbf{F}(t)$ and setting it equal to zero gives:

$$\Delta\mathbf{F}^T(t)R(t) + \Delta\boldsymbol{\lambda}^\dagger G(t) = 0.$$

Solving for $\Delta\mathbf{F}(t)$ gives (recall $R(t)$ is positive-definite and Hermitian):

$$\Delta\mathbf{F}(t) = -R^{-1}(t)G^{\dagger}(t)\Delta\boldsymbol{\lambda}(t). \tag{2.25}$$

Eq. (2.25) relates the control modification $\Delta\mathbf{F}(t)$ to the Lagrange multiplier $\Delta\boldsymbol{\lambda}(t)$. Note that for the second strategy presented in Section 2.5, this equation will be transformed into a feedback control law.

3. Variation of $\Delta\boldsymbol{\lambda}(t)$: By design, J_3 was added to the cost function to insure that the Schrodinger dynamics of $\Delta\mathbf{y}(t)$ is not violated by the optimization process. Taking the functional derivative of the first line of Eq. (2.21) and setting the result equal to zero gives

$$\frac{d}{dt}\Delta\mathbf{y}(t) - G(t)\Delta\mathbf{F}(t) = 0, \tag{2.26}$$

which is Eq. (2.19) as required. As discussed before, its initial condition is

$$\Delta\mathbf{y}(-T/2) = -\Delta\boldsymbol{\beta}. \tag{2.27}$$

2.5 Solution Strategies

This section describes two strategies for solving the Euler-Lagrange equations of motion for optimal control (Eqs. (2.23)-(2.27)). Each strategy provides a way to determine $\Delta\boldsymbol{\lambda}(t)$ without directly integrating Eqs. (2.23)–(2.24). The first is based on an *ansatz* for the Lagrange multiplier $\Delta\boldsymbol{\lambda}(t)$, while the second relates $\Delta\boldsymbol{\lambda}(t)$ to $\Delta\mathbf{y}(t)$ through the Ricatti matrix $S(t)$.

In Chapter 3 I use the neighboring optimal control formalism to improve the performance of all gates in the universal set of gates introduced in Section 3.1.2.

Strategy 1 will be used to improve all one-qubit gates, while Strategy 2 will be used to improve the sole two-qubit gate in the set.

2.5.1 Strategy 1 – Lagrange multiplier *ansatz*

This subsection presents an approach to solving the Euler-Lagrange (EL) equations for optimal control, in the case that the quantum system of interest is a single qubit. This approach is based on the following *ansatz* for the Lagrange multiplier:

$$\Delta\boldsymbol{\lambda}(t) = -\exp\left[-(t+T/2)/10\right]\mathbf{w}, \tag{2.28}$$

where $-T/2 \leq t \leq T/2$, and $\mathbf{w}$ is a 4-component constant column vector that is determined by demanding that: (i) the gate modification $\delta A(t) = i[\delta U(t) - I_{2\times 2}]$ satisfies the Schrodinger equation (viz. Eq. (2.7)), where $I_{n\times n}$ is the n-dimensional identity matrix; and (ii) $\delta A(T/2) = \delta\beta + \mathcal{O}(\Delta^2)$, where $\delta\beta = i[U_0^\dagger(T/2)U_{tgt} - I_{2\times 2}] + \mathcal{O}(\Delta^2)$ (see Eq. (2.14)). Note that, because of the second requirement, it follows from Eq. (2.6) that

$$\begin{aligned}
\delta U(T/2) &= I_{2\times 2} - i\delta A(T/2) + \mathcal{O}(\Delta^2) \\
&= I_{2\times 2} - i\delta\beta + \mathcal{O}(\Delta^2) \\
&= U_0^\dagger(T/2)U_{tgt} + \mathcal{O}(\Delta^2),
\end{aligned}$$

and consequently, the new gate $U(T/2) = U_0(T/2)\delta U(T/2)$ satisfies:

$$\begin{aligned}
U(T/2) &= U_0(T/2)\left[U_0^\dagger(T/2)U_{tgt}\right] \\
&= U_{tgt} + \mathcal{O}(\Delta^2).
\end{aligned} \tag{2.29}$$

Thus, by choosing the column vector $\mathbf{w}$ in this way, the EL Eqs. (2.26) and (2.27) are insured to be satisfied, and the new gate $U(T/2)$ is the target gate U_{tgt} to second-order in small quantities as desired.

I next choose $R(t) = I_{3\times 3}$, so that Eq. (2.25) gives the control modification:

$$\Delta\mathbf{F}(t) = \exp\left[-(t+T/2)/10\right] G^{\dagger}(t)\mathbf{w}. \tag{2.30}$$

Once $\mathbf{w}$ is determined, EL Eq. (2.25) is satisfied.

Finally, choosing $Q(t)$ to be a diagonal matrix, Eq. (2.24) determines $Q(t)$ from the *ansatz* for $\Delta\boldsymbol{\lambda}(t)$ and the solution $\Delta\mathbf{y}(t)$ of Eqs. (2.26) and (2.27). With this choice, the EL Eq. (2.24) is satisfied. Thus, once $\mathbf{w}$ is known, the strategy's construction insures that all EL equations are satisfied, and yields the control and gate modifications $\Delta\mathbf{F}(t)$ and $\Delta\mathbf{y}(t)$. Note that Strategy 1 has the following significant benefit. By introducing an *ansatz* for $\Delta\boldsymbol{\lambda}(t)$, computation of the control and gate modifications $\Delta\mathbf{F}(t)$ and $\Delta\mathbf{y}(t)$ becomes independent of $Q(t)$. Thus Strategy 1 does not actually require $Q(t)$ in Eq. (2.24)to be computed.

I now describe how $\mathbf{w}$ is determined. Begin by inserting Eq. (2.30) into Eq. (2.7):

$$\begin{aligned}\frac{d}{dt}\delta A &= \sum_{j=1}^{3} \overline{G}_j \Delta F_j \\ &= \exp\left[-(t+T/2)/10\right] \sum_{j=1}^{3} \overline{G}_j \left(G^{\dagger}\mathbf{w}\right)_j . \end{aligned} \tag{2.31}$$

For simplicity I rewrite the term $\sum_{j=1}^{3} \overline{G}_j \left(G^{\dagger}\mathbf{w}\right)_j$ on the RHS of Eq. (2.31) as $\mathcal{I}$. I

show below that

$$\begin{aligned}\mathcal{I} &\equiv \sum_{j=1}^{3} \overline{G}_j \left(G^\dagger \mathbf{w}\right)_j \\ &= \begin{pmatrix} w_1 - w_4 & 2w_3 \\ 2w_2 & w_4 - w_1 \end{pmatrix}.\end{aligned} \tag{2.32}$$

Note that in deriving the result in Eq. (2.32) I explicitly assumed that the dynamics of the single qubit quantum system here is driven by the Zeeman Hamiltonian $H(t) = -\boldsymbol{\sigma} \cdot \mathbf{F}(t)$. Following the development in Section 2.2, for this Hamiltonian, $\mathcal{G}_j = -\sigma_j$, where the $1, 2, 3$ components of $\boldsymbol{\sigma}$ are the x, y, z Pauli matrices, respectively, and

$$\overline{G}_j = U_0^\dagger \mathcal{G}_j U_0 = -U_0^\dagger \sigma_j U_0,$$

with

$$U_0 = \begin{pmatrix} U_{0,11} & U_{0,12} \\ U_{0,21} & U_{0,22} \end{pmatrix} \equiv \begin{pmatrix} | & | \\ \mathbf{u}_{0,1} & \mathbf{u}_{0,2} \\ | & | \end{pmatrix}. \tag{2.33}$$

It follows from the unitarity of U_0 that $\mathbf{u}_{0,1}$ and $\mathbf{u}_{0,2}$ form an orthonormal set: $\mathbf{u}_{0,i}^\dagger \mathbf{u}_{0,j} = \delta_{ij}$.

It proves useful to define the vector pairs $(\mathbf{e}_1, \mathbf{e}_2)$, $(\mathbf{f}_1, \mathbf{f}_2)$, and $(\mathbf{g}_1, \mathbf{g}_2)$ as fol-

lows:

$$\sigma_x U_0 = \begin{pmatrix} | & | \\ \mathbf{e}_1 & \mathbf{e}_2 \\ | & | \end{pmatrix};$$

$$\sigma_y U_0 = \begin{pmatrix} | & | \\ \mathbf{f}_1 & \mathbf{f}_2 \\ | & | \end{pmatrix}; \tag{2.34}$$

$$\sigma_z U_0 = \begin{pmatrix} | & | \\ \mathbf{g}_1 & \mathbf{g}_2 \\ | & | \end{pmatrix}.$$

With these preliminaries, I then write $\overline{G}_j$ as

$$\overline{G}_1 = -\begin{pmatrix} \mathbf{u}_{0,1}^\dagger \mathbf{e}_1 & \mathbf{u}_{0,1}^\dagger \mathbf{e}_2 \\ \mathbf{u}_{0,2}^\dagger \mathbf{e}_1 & \mathbf{u}_{0,2}^\dagger \mathbf{e}_2 \end{pmatrix} \equiv \begin{pmatrix} | & | \\ \boldsymbol{\gamma}_{1;1} & \boldsymbol{\gamma}_{1;2} \\ | & | \end{pmatrix};$$

$$\overline{G}_2 = -\begin{pmatrix} \mathbf{u}_{0,1}^\dagger \mathbf{f}_1 & \mathbf{u}_{0,1}^\dagger \mathbf{f}_2 \\ \mathbf{u}_{0,2}^\dagger \mathbf{f}_1 & \mathbf{u}_{0,2}^\dagger \mathbf{f}_2 \end{pmatrix} \equiv \begin{pmatrix} | & | \\ \boldsymbol{\gamma}_{2;1} & \boldsymbol{\gamma}_{2;2} \\ | & | \end{pmatrix}; \tag{2.35}$$

$$\overline{G}_3 = -\begin{pmatrix} \mathbf{u}_{0,1}^\dagger \mathbf{g}_1 & \mathbf{u}_{0,1}^\dagger \mathbf{g}_2 \\ \mathbf{u}_{0,2}^\dagger \mathbf{g}_1 & \mathbf{u}_{0,2}^\dagger \mathbf{g}_2 \end{pmatrix} \equiv \begin{pmatrix} | & | \\ \boldsymbol{\gamma}_{3;1} & \boldsymbol{\gamma}_{3;2} \\ | & | \end{pmatrix},$$

which gives

$$\mathbf{G}_1 = \begin{pmatrix} \boldsymbol{\gamma}_{1;1} \\ \boldsymbol{\gamma}_{1;2} \end{pmatrix}; \mathbf{G}_2 = \begin{pmatrix} \boldsymbol{\gamma}_{2;1} \\ \boldsymbol{\gamma}_{2;2} \end{pmatrix}; \mathbf{G}_3 = \begin{pmatrix} \boldsymbol{\gamma}_{3;1} \\ \boldsymbol{\gamma}_{3;2} \end{pmatrix}, \tag{2.36}$$

and

$$G = \begin{pmatrix} | & | & | \\ \mathbf{G}_1 & \mathbf{G}_2 & \mathbf{G}_3 \\ | & | & | \end{pmatrix} = \begin{pmatrix} \boldsymbol{\gamma}_{1;1} & \boldsymbol{\gamma}_{2;1} & \boldsymbol{\gamma}_{3;1} \\ \boldsymbol{\gamma}_{1;2} & \boldsymbol{\gamma}_{2;2} & \boldsymbol{\gamma}_{3;2} \end{pmatrix}. \tag{2.37}$$

Writing

$$\mathbf{w} = \begin{pmatrix} w_1 \\ w_2 \\ w_3 \\ w_4 \end{pmatrix} = \begin{pmatrix} \boldsymbol{\omega}_1 \\ \boldsymbol{\omega}_2 \end{pmatrix} \tag{2.38}$$

gives

$$G^\dagger \mathbf{w} = \begin{pmatrix} \boldsymbol{\gamma}_{1;1}^\dagger \boldsymbol{\omega}_1 + \boldsymbol{\gamma}_{1;2}^\dagger \boldsymbol{\omega}_2 \\ \boldsymbol{\gamma}_{2;1}^\dagger \boldsymbol{\omega}_1 + \boldsymbol{\gamma}_{2;2}^\dagger \boldsymbol{\omega}_2 \\ \boldsymbol{\gamma}_{3;1}^\dagger \boldsymbol{\omega}_1 + \boldsymbol{\gamma}_{3;2}^\dagger \boldsymbol{\omega}_2 \end{pmatrix} \equiv \begin{pmatrix} \pi_1 \\ \pi_2 \\ \pi_3 \end{pmatrix}. \tag{2.39}$$

With these definitions, the calculation of the matrix elements of $\mathcal{I}$ is simplified. Below I show explicitly the calculation of the matrix element $\mathcal{I}_{11}$. Calculation of the remaining three matrix elements is similar and so I simply quote the final result for these matrix elements at the end of this subsection.

Inserting Eqs. (2.35)–(2.39) into $\mathcal{I} = \sum_{j=1}^{3} \overline{G}_j \left(G^\dagger \mathbf{w}\right)_j$ gives

$$
\begin{aligned}
\mathcal{I}_{11} &= (\overline{G}_1)_{11}(G^\dagger \mathbf{w})_1 + (\overline{G}_2)_{11}(G^\dagger \mathbf{w})_2 + (\overline{G}_3)_{11}(G^\dagger \mathbf{w})_3 \\
&= -\mathbf{u}_{0,1}^\dagger \mathbf{e}_1 \pi_1 - \mathbf{u}_{0,1}^\dagger \mathbf{f}_1 \pi_2 - \mathbf{u}_{0,1}^\dagger \mathbf{g}_1 \pi_3 \\
&= w_1 \left[(\mathbf{u}_{0,1}^\dagger \mathbf{e}_1)(\mathbf{e}_1^\dagger \mathbf{u}_{0,1}) + (\mathbf{u}_{0,1}^\dagger \mathbf{f}_1)(\mathbf{f}_1^\dagger \mathbf{u}_{0,1}) + (\mathbf{u}_{0,1}^\dagger \mathbf{g}_1)(\mathbf{g}_1^\dagger \mathbf{u}_{0,1}) \right] \\
&\quad + w_2 \left[(\mathbf{u}_{0,1}^\dagger \mathbf{e}_1)(\mathbf{e}_1^\dagger \mathbf{u}_{0,2}) + (\mathbf{u}_{0,1}^\dagger \mathbf{f}_1)(\mathbf{f}_1^\dagger \mathbf{u}_{0,2}) + (\mathbf{u}_{0,1}^\dagger \mathbf{g}_1)(\mathbf{g}_1^\dagger \mathbf{u}_{0,2}) \right] \\
&\quad + w_3 \left[(\mathbf{u}_{0,1}^\dagger \mathbf{e}_1)(\mathbf{e}_2^\dagger \mathbf{u}_{0,1}) + (\mathbf{u}_{0,1}^\dagger \mathbf{f}_1)(\mathbf{f}_2^\dagger \mathbf{u}_{0,1}) + (\mathbf{u}_{0,1}^\dagger \mathbf{g}_1)(\mathbf{g}_2^\dagger \mathbf{u}_{0,1}) \right] \\
&\quad + w_4 \left[(\mathbf{u}_{0,1}^\dagger \mathbf{e}_1)(\mathbf{e}_2^\dagger \mathbf{u}_{0,2}) + (\mathbf{u}_{0,1}^\dagger \mathbf{f}_1)(\mathbf{f}_2^\dagger \mathbf{u}_{0,2}) + (\mathbf{u}_{0,1}^\dagger \mathbf{g}_1)(\mathbf{g}_2^\dagger \mathbf{u}_{0,2}) \right]
\end{aligned}
$$

Incorporating Eqs. (2.33)– (2.34) finally gives (after a moderate amount of algebra)

$$\mathcal{I}_{11} = w_1 - w_4. \tag{2.40}$$

Similar calculations give:

$$\mathcal{I}_{21} = 2w_2 \tag{2.41}$$

$$\mathcal{I}_{12} = 2w_3 \tag{2.42}$$

$$\mathcal{I}_{22} = w_4 - w_1. \tag{2.43}$$

This completes the derivation of Eq. (2.32).

Next, using Eq. (2.32) in Eq. (2.31) gives

$$\frac{d}{dt} \begin{pmatrix} \delta A_{11} & \delta A_{12} \\ \delta A_{21} & \delta A_{22} \end{pmatrix} = \exp\left[-(t+T/2)/10\right] \begin{pmatrix} w_1 - w_4 & 2w_3 \\ 2w_2 & w_4 - w_1 \end{pmatrix}. \tag{2.44}$$

For constant w_1, w_2, w_3 and w_4, Eq. (2.44) is easily integrated to get

$$\begin{aligned}
\delta A_{11}(t) &= 10\,(w_1 - w_4)\,\mathcal{A}(t) \\
\delta A_{21}(t) &= 20 w_2\,\mathcal{A}(t) \\
\delta A_{12}(t) &= 20 w_3\,\mathcal{A}(t) \\
\delta A_{22}(t) &= 10\,(w_4 - w_1)\,\mathcal{A}(t),
\end{aligned} \tag{2.45}$$

where

$$\mathcal{A}(t) = 1 - \exp\left[-(t + T/2)/10\right]. \tag{2.46}$$

For the one-qubit gate numerical simulations presented in Chapter 3 I use $T = 160$ [36]. Thus $\mathcal{A}(T/2) = 1 - \exp(-16) = 1 + \mathcal{O}(10^{-7})$. Combining this with the requirement that $\delta A(T/2) = \delta\beta$ gives

$$\begin{aligned}
w_1 - w_4 &= \frac{\delta\beta_{11}}{10} \\
w_2 &= \frac{\delta\beta_{21}}{20} \\
w_3 &= \frac{\delta\beta_{12}}{20} \\
w_4 - w_1 &= \frac{\delta\beta_{22}}{10}.
\end{aligned} \tag{2.47}$$

Recall that $U_0^\dagger(T/2)U_{tgt} = I - i\delta\beta + \mathcal{O}(\Delta^2)$ so that

$$\begin{aligned}
Tr\left[U_0^\dagger(T/2)U_{tgt}\right] &= 2 - i\,Tr\,\delta\beta + \mathcal{O}(\Delta^2) \\
&= 2 - i\,(\delta\beta_{11} + \delta\beta_{22}) + \mathcal{O}(\Delta^2).
\end{aligned} \tag{2.48}$$

In Section 3.3.1 I show that for all one-qubit gates of interest in this thesis, $Tr\left[U_0^\dagger(T/2)U_{tgt}\right] = 2 + \mathcal{O}(\Delta^2)$, so that

$$\delta\beta_{11} + \delta\beta_{22} = 0. \tag{2.49}$$

Combining Eq. (2.49) with the choice $w_1 = -w_4$, reduces Eqs. (2.47) to

$$\mathbf{w} = \frac{\Delta\boldsymbol{\beta}}{20}, \tag{2.50}$$

where, recall,

$$\Delta\boldsymbol{\beta} = \begin{pmatrix} \delta\beta_{11} \\ \delta\beta_{21} \\ \delta\beta_{12} \\ \delta\beta_{22} \end{pmatrix}. \tag{2.51}$$

Eqs. (2.50) and (2.51), together with $\delta\beta = i[U_0^\dagger(T/2)U_{tgt} - I]$, determine $\mathbf{w}$. As I noted above, this then determines the control modification $\Delta\mathbf{F}(t)$, and solution of the Schrodinger equation determines $\Delta\mathbf{y}(t)$ which gives the gate modification $\delta U(t)$. The new control field is $\mathbf{F}(t) = \mathbf{F}_0(t) + \Delta\mathbf{F}(t)$, and the new gate is $U(T/2) = U_0(T/2)\delta U(T/2)$. I implement Strategy 1 in Section 3.3.1.1 to improve all the one-qubit gates in the universal quantum gates set introduced in Section 3.1.2.

2.5.2 Strategy 2 – Ricatti equation and the control gain matrix

This section presents a general approach to solving the Euler-Lagrange (EL) equations for optimal control, with no preassumption about the quantum system dynamics. I implement this strategy in Section 3.3.1.2 to improve the two-qubit gate in the universal quantum gates set introduced in Section 3.1.2.

Eq. (2.24) shows that $\Delta\mathbf{y}(t)$ acts as the source for the Lagrange multiplier $\Delta\boldsymbol{\lambda}(t)$. I look for a solution of Eq. (2.24) of the form

$$\Delta\boldsymbol{\lambda}(t) = S(t)\Delta\mathbf{y}(t), \tag{2.52}$$

where $S(t)$ is known as the Ricatti matrix. Note that once $S(t)$ has been determined, Eq. (2.25) becomes the feedback control law

$$\begin{aligned} \Delta\mathbf{F}(t) &= -R^{-1}(t)G^{\dagger}(t)S(t)\Delta\mathbf{y}(t) \\ &= -C(t)\Delta\mathbf{y}(t) \end{aligned} \tag{2.53}$$

which relates the state modification $\Delta\mathbf{y}(t)$ to the control modification $\Delta\mathbf{F}(t)$. The matrix $C(t) = R^{-1}(t)G^{\dagger}(t)S(t)$ is known as the control gain matrix.

To obtain the equation of motion for $S(t)$ I differentiate Eq. (2.52), and then use Eqs. (2.24) and (2.26) to substitute for $\Delta\dot{\boldsymbol{\lambda}}$ and $\Delta\dot{\mathbf{y}}$. One finds

$$\begin{aligned} \dot{S}\Delta\mathbf{y} &= \Delta\dot{\boldsymbol{\lambda}} - S\Delta\dot{\mathbf{y}} \\ &= -Q\Delta\mathbf{y} - SG\Delta\mathbf{F} \\ &= -Q\Delta\mathbf{y} - SG(-R^{-1}G^{\dagger}S\Delta\mathbf{y}) \\ &= \left[-Q + SGR^{-1}G^{\dagger}S\right]\Delta\mathbf{y}. \end{aligned} \tag{2.54}$$

Identifying the coefficients of $\Delta\mathbf{y}$ on both sides of Eq. (2.54) gives the Ricatti equation [37]:

$$\frac{dS}{dt} = -Q + SGR^{-1}G^{\dagger}S. \tag{2.55}$$

The "initial" condition for $S(T/2)$ is found from Eqs. (2.23) and (2.52):

$$\Delta\mathbf{y}(T/2) = \Delta\boldsymbol{\lambda}(T/2) = S(T/2)\Delta\mathbf{y}(T/2),$$

from which it follows that

$$S(T/2) = I. \tag{2.56}$$

Note that by introducing the Ricatti matrix $S(t)$ I have transformed the problem of finding the Lagrange multiplier $\Delta\boldsymbol{\lambda}(t)$ to that of finding $S(t)$. This is a good

strategy as the Ricatti equation is independent of both $\Delta\mathbf{y}(t)$ and $\Delta\mathbf{F}(t)$ and so can be solved once and for all. This is not the case with Eq. (2.24). The equations that determine the path and control modifications $\Delta\mathbf{y}(t)$ and $\Delta\mathbf{F}(t)$ are thus Eqs. (2.17), (2.26), (2.27), (2.53), (2.55), and (2.56). Note that substituting the feedback control law (Eq. (2.53)) into Eq. (2.26) obtains

$$\frac{d}{dt}\Delta\mathbf{y} = -GC\Delta\mathbf{y}. \tag{2.57}$$

Once the Ricatti matrix $S(t)$ is known, the control gain matrix $C(t)$ is known, and Eq. (2.57) can then be integrated for $\Delta\mathbf{y}(t)$. With $\Delta\mathbf{y}(t)$ in hand, Eq. (2.53) determines the control modification $\Delta\mathbf{F}(t)$, and so the improved control $\mathbf{F}(t) = \mathbf{F}_0(t) + \Delta\mathbf{F}(t)$. Note that if all the eigenvalues of GC are positive, then $\Delta\mathbf{y}(t \to \infty) = 0$, and so from Eq. (2.17), that $\Delta\mathbf{x}(t \to \infty) = \Delta\boldsymbol{\beta}$. This, in turn implies that $\delta U(t \to \infty) = U_0^\dagger U_{tgt}$, and finally, $U(t \to \infty) = U_{tgt}$ as desired.

In Chapter 3 I show how the NOC theory introduced above can be used to implement a robust and high-fidelity approximation to each gate in a universal set of quantum gates.

Chapter 3: Application of NOC to Improve Quantum Gate Performance

In Chapter 2 I described a general theoretical framework for improving the performance of a good quantum gate based on neighboring optimal control (NOC). This NOC method takes as input a nominal control $\mathbf{F}_0(t)$ that enacts a unitary transformation $U_0(t)$ such that $U_{0,f} = U_0(T/2)$ is a good approximation to a target gate U_{tgt}, and derives the equations of motion (EOMs) Eqs.(2.23-2.27) which determine the optimal solution by minimizing the cost function Eq. (2.22). Two strategies for obtaining the solution to the EOMs were presented, and finally, the determined optimal control modification $\Delta\mathbf{F}(t)$ provided an improved approximation $U(t = T/2)$ to the target U_{tgt}.

This chapter illustrates the general method by applying it to improve the performance of all gates in a universal set of quantum gates $\mathcal{G}_U$. The gates I chose are produced using a form of non-adiabatic rapid passage that has been studied in the literature [34, 38–44]. I stress that the method introduced in Section 2 is not limited to this particular family of input gates - any other good gate, or set of gates, could serve as the input for the method.

In the following, I use: (i) Strategy 1 to determine the performance im-

provements for all the one-qubit gates in $\mathcal{G}_U$, and (ii) Strategy 2 for the two-qubit controlled-phase gate. Section 3.1 briefly reviews the background material on twisted rapid passage. Section 3.2 summarizes the numerical simulation procedure for improving the performance of the TRP gates using the NOC method. Section 3.3 presents the NOC performance gains under ideal control, and examines the bandwidth required to implement the ideal controls, while Section 3.4 considers the robustness of these improvements to some typical control imperfections. I show that under suitable conditions, all gate error probabilities fall well below the target threshold of $P_a = 10^{-4}$.

3.1 Twisted Rapid Passage

In an effort to make this chapter more self-contained, here I briefly review relevant background material on twisted rapid passage (TRP). For a more detailed presentation, the reader is directed to Refs. [34, 38, 42, 43]

3.1.1 TRP profiles

To introduce TRP [34,38], I consider a single-qubit interacting with an external control-field $\mathbf{F}(t)$ via the Zeeman interaction $H_z(t) = -\boldsymbol{\sigma} \cdot \mathbf{F}(t)$, where σ_i are the Pauli matrices ($i = x, y, z$). TRP is a generalization of adiabatic rapid passage (ARP) [45]. In ARP, the control-field $\mathbf{F}(t)$ is slowly inverted over a time T with $\mathbf{F}(t) = at\,\hat{\mathbf{z}} + b\,\hat{\mathbf{x}}$. In TRP, however, the control-field is allowed to twist in the x-y plane with time-varying azimuthal angle $\phi(t)$, while simultaneously undergoing

inversion along the z-axis: $\mathbf{F}_0(t) = at\,\hat{\mathbf{z}} + b\cos\phi(t)\,\hat{\mathbf{x}} + b\sin\phi(t)\,\hat{\mathbf{y}}$. Here $-T/2 \leq t \leq T/2$ and I consider TRP with *non-adiabatic* inversion.

As shown in Ref. [34], when a qubit is subject to the TRP Hamiltonian, the qubit undergoes resonance when

$$at - \frac{\hbar}{2}\frac{d\phi}{dt} = 0. \tag{3.1}$$

For polynomial twist, the twist profile $\phi(t)$ takes the form

$$\phi_n(t) = \frac{2}{n}Bt^n. \tag{3.2}$$

In this case, Eq. (3.1) has $n-1$ roots, though only real-valued roots correspond to resonance. Ref. [38] showed that for $n \geq 3$, the qubit undergoes resonance multiple times during a *single* TRP sweep: (i) for all $n \geq 3$, when $B > 0$; and (ii) for odd $n \geq 3$, when $B < 0$. For the remainder of this chapter I consider only $B > 0$, and to *quartic* twist for which $n = 4$ in Eq. (3.2). During quartic twist, the qubit passes through resonance at times $t = 0, \pm\sqrt{a/\hbar B}$ [38]. It is thus possible to alter the time separating the resonances by varying the TRP sweep parameters B and a.

Ref. [38] showed that these multiple resonances have a strong influence on the qubit transition probability, allowing transitions to be strongly enhanced or suppressed through a small variation of the sweep parameters. Ref. [46] calculated the qubit transition amplitude to all orders in the non-adiabatic coupling and found they can be expressed as the following diagrammatic series:

$T_-(t)$ =

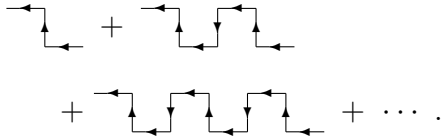

(3.3)

Lower (upper) lines correspond to propagation in the negative (positive) energy-level, and the vertical lines correspond to transitions between the two energy-levels. The calculation sums the probability amplitudes for all interfering alternatives [47] that allow the qubit to end up in the positive energy-level given that it was initially in the negative energy-level. As discussed before, varying the TRP sweep parameters varies the time separating the resonances. This in turn changes the value of each diagram in Eq. (3.3), and thus alters the interference between the alternative transition pathways. It is the sensitivity of the individual alternatives/diagrams to the time separation of the resonances that allows TRP to manipulate this quantum interference.

Zwanziger *et al.* [39] observed these interference effects in the transition probability using NMR and found excellent quantitative agreement between theory and experiment. It is this link between interfering quantum alternatives and the TRP sweep parameters that I believe underlies the ability of TRP to drive high-fidelity non-adiabatic one- and two-qubit gates.

3.1.2 TRP universal quantum gates set

The universal set of quantum gates $\mathcal{G}_U$ that is of interest here consists of the one-qubit Hadamard and NOT gates, together with variants of the one-qubit $\pi/8$ and phase gates, and the two-qubit controlled-phase gate. These gates are defined as:

1. Hadamard:

$$U_h = (1/\sqrt{2})\,(\,\sigma_z + \sigma_x) = \frac{1}{\sqrt{2}} \begin{pmatrix} 1 & 1 \\ 1 & -1 \end{pmatrix}; \tag{3.4}$$

2. NOT:

$$U_{not} = \sigma_x = \begin{pmatrix} 0 & 1 \\ 1 & 0 \end{pmatrix}; \tag{3.5}$$

3. Modified $\pi/8$:

$$V_{\pi/8} = \cos(\pi/8)\ \sigma_x - \sin(\pi/8)\ \sigma_y = \begin{pmatrix} 0 & e^{i\pi/8} \\ e^{-i\pi/8} & 0 \end{pmatrix}; \tag{3.6}$$

4. Modified phase:

$$V_p = (1/\sqrt{2})\,(\,\sigma_x - \sigma_y\,) = \begin{pmatrix} 0 & e^{i\pi/4} \\ e^{-i\pi/4} & 0 \end{pmatrix}; \tag{3.7}$$

5. Modified controlled-phase:

$$V_{cp} = (1/2)\left[\left(I^1 + \sigma_z^1\right) I^2 - \left(I^1 - \sigma_z^1\right)\sigma_z^2\right] = \begin{pmatrix} 1 & 0 & 0 & 0 \\ 0 & 1 & 0 & 0 \\ 0 & 0 & -1 & 0 \\ 0 & 0 & 0 & 1 \end{pmatrix}. \tag{3.8}$$

The universality of $\mathcal{G}_U$ was demonstrated in Ref. [42] by showing that its gates could construct the well-known universal set comprised of the Hadamard, phase, $\pi/8$, and CNOT gates.

3.2 Simulation Procedure

As is well-known, the Schrodinger dynamics is driven by a Hamiltonian $H(t)$ that causes a unitary transformation $U(t, t_0)$ to be applied to an initial quantum state $|\psi(t_0)\rangle$. In this chapter, I assume that the Hamiltonian $H(t)$ contains terms that independently Zeeman-couple each qubit to a TRP control-field $\mathbf{F}_0(t)$. Assigning values to the TRP sweep parameters (a, b, B, T) fixes the control-field $\mathbf{F}_0(t)$, and in turn, the actual unitary transformation $U_a = U(t_0 + T, t_0)$ applied to $|\psi(t_0)\rangle$. Ref. [42] used optimization algorithms to find TRP sweep parameter values that produced an applied one-qubit (two-qubit) gate U_a that approximates a desired target gate U_{tgt} sufficiently closely that its error probability (defined below) satisfies $P_e < 10^{-4}$ (10^{-3}) [48]. In the following, the target gate U_{tgt} will be one of the gates in the universal set $\mathcal{G}_U$. Since $\mathcal{G}_U$ contains only one- and two-qubit gates, the simulations will only involve one- and two-qubit systems.

For *one-qubit simulations*, the nominal Hamiltonian $H_0^1(t)$ is the Zeeman Hamiltonian $H_z(t)$ introduced in Section 3.1.1. Ref. [34] (see also Appendix A) showed that it can be written in the following dimensionless form:

$$\begin{aligned} H_0^1(\tau) &= (1/\lambda)\ \{-\tau\sigma_z - \cos\phi_4(\tau)\sigma_x - \sin\phi_4(\tau)\sigma_y\} \\ &= -\boldsymbol{\sigma}\cdot\mathbf{F}_0(\tau), \end{aligned} \tag{3.9}$$

where $\mathbf{F}_0(\tau)$ is the dimensionless TRP control field; $\tau = (a/b)t$; $\lambda = \hbar a/b^2$; and for quartic twist, $\phi_4(\tau) = (\eta_4/2\lambda)\tau^4$, with $\eta_4 = \hbar B b^2/a^3$. In this Section, I show how the neighboring optimal control framework introduced in Section 2 can be applied to

improve the performance of the TRP-generated one-qubit gates: Hadamard, NOT, modified phase, and modified $\pi/8$.

For the *two-qubit simulations*, the nominal Hamiltonian $H_0^2(t)$ contains terms that Zeeman-couple each qubit to the same TRP control-field $\mathbf{F}_0(t)$, and an Ising interaction term that couples the two qubits. Alternative two-qubit interactions can be considered, though all simulation results presented in this chapter assume an Ising interaction between the qubits. I note here that the energy difference between the two upper energy levels and the two lower energy levels are the same. To break a resonance-frequency degeneracy $\omega_{12} = \omega_{34}$ for transitions between, respectively, the ground and first-excited states ($E_1 \leftrightarrow E_2$) and the second- and third-excited states ($E_3 \leftrightarrow E_4$), the term $c_4|E_4(t)\rangle\langle E_4(t)|$ was added to $H_2(t)$.

Combining all of these factors, I arrive at the following (dimensionless) two-qubit Hamiltonian (see Ref. [42] or Appendix A for further details):

$$\begin{aligned} H_0^2(\tau) = & \left[-(d_1+d_2)/2 + \tau/\lambda\right]\sigma_z^1 \\ & + \left[-d_2/2 + \tau/\lambda\right]\sigma_z^2 \\ & -(d_3/\lambda)\left[\cos\phi_4\sigma_x^1 + \sin\phi_4\sigma_y^1\right] \\ & -(1/\lambda)\left[\cos\phi_4\sigma_x^2 + \sin\phi_4\sigma_y^2\right] \\ & -(\pi d_4/2)\sigma_z^1\sigma_z^2 \quad + c_4|E_4(\tau)\rangle\langle E_4(\tau)|. \end{aligned} \tag{3.10}$$

Here: (i) $b_i = \hbar\gamma_i B_{rf}/2$, $\omega_i = \gamma_i B_0$, γ_i is the coupling constant for qubit i, and $i = 1, 2$; (ii) $\tau = (a/b_2)t$, $\lambda = \hbar a/b_2^2$, and $\eta_4 = \hbar B b_2^2/a^3$; and (iii) $d_1 = (\omega_1 - \omega_2)b_2/a$, $d_2 = (\Delta/a)b_2$, $d_3 = b_1/b_2$, and $d_4 = (J/a)b_2$, where Δ is a detuning parameter. I present results for the two-qubit modified controlled phase gate below.

Given an applied gate U_a, a target gate U_{tgt}, and the initial state $|\psi\rangle$, it is possible to determine (see Ref. [34] or Appendix A) the error probability $P_e(\psi)$ for the TRP final state $|\psi_a\rangle = U_a|\psi\rangle$, relative to the target final state $|\psi_{tgt}\rangle = U_{tgt}|\psi\rangle$. The gate error probability P_e is defined to be the worst-case value [49] of $P_e(\psi)$: $P_e \equiv \max_{|\psi\rangle} P_e(\psi)$. Introducing the positive operator $P = \left(U_a^\dagger - U_{tgt}^\dagger\right)(U_a - U_{tgt})$, Ref. [34] showed that the error probability P_e satisfies the upper bound $P_e \leq Tr\, P$. Once U_a is known, $Tr\, P$ is easily evaluated, and so it is a convenient proxy for P_e which is harder to calculate. $Tr\, P$ also has the virtue of being directly related to the gate fidelity $\mathcal{F}_n = (1/2^n)\ Re\left[\, Tr\left(U_a^\dagger U_{tgt}\right)\right]$, where n is the number of qubits acted on by the gate. It is straightforward to show [42] that $\mathcal{F}_n = 1 - (1/2^{n+1})\ Tr\, P$. The simulations calculate $Tr\, P$, which is then used to upper bound the gate error probability P_e. Note that minimizing $Tr\, P$ is equivalent to maximizing the gate fidelity $\mathcal{F}_n$.

The procedure for solving the EL equations for optimal control was briefly described in Section 2.5. The one-qubit TRP gates presented in Ref. [44] and the two-qubit TRP gate presented in Ref. [42] will serve as the good gates that are to be improved. For convenience, the TRP sweep parameters for these gates are presented in Appendix A, along with their associated gate error probabilities and fidelities. For a particular target gate U_{tgt} belonging to $\mathcal{G}_U$ (see Section 3.1.2), the TRP sweep parameters corresponding to U_{tgt} determine the TRP control field $\mathbf{F}_0(\tau)$ which then drives the nominal Hamiltonian $H_0(\tau)$ (see Eqs. (3.9) and (3.10) for one- and two-qubit gates, respectively). The nominal Hamiltonian in turn produces the initial good approximate gate $U_0(\tau_0/2, -\tau_0/2)$ that is to be improved. Here τ is

the dimensionless time introduced above, and $\tau_0 \equiv aT/b$. For each gate in $\mathcal{G}_U$, its TRP approximation $U_0(\tau_0/2, -\tau_0/2)$ is also reproduced in Appendix A. For the two strategies introduced in Section 2.5, the numerical simulation implements the following procedure:

1. For both Strategies, integrate the Schrodinger equation with the nominal Hamiltonian $H_0(\tau)$ to obtain $U_0(\tau_0/2, -\tau_0/2)$; calculate $\Delta\boldsymbol{\beta}$ using Eq. (2.14). For Strategy 1, also calculate $\mathbf{w}$ using Eq. (2.50).

2. For both Strategies, calculate $\overline{G}_j(\tau) = U_0^\dagger(\tau)\mathcal{G}_j U_0(\tau)$, where I have abbreviated $U_0(\tau, -\tau_0/2)$ as $U_0(\tau)$, and $\mathcal{G}_j(\tau) = \delta H/\delta F_j|_{\mathbf{F}_0(\tau)}$; form $G(\tau)$. For Strategy 1, skip Step 3, go to Step 4.

3. For Strategy 2, set $R(\tau) = I_{3\times 3}$ and $S(\tau) = I_{16\times 16}$, where $I_{n\times n}$ is the $n \times n$ identity matrix. The Ricatti equation then requires $Q(\tau) = G(\tau)G^\dagger(\tau)$. The resulting control gain matrix is $C(\tau) = G^\dagger(\tau)$.

4. (a) For Strategy 1, use Eq. (2.30) to determine the control modification $\Delta\mathbf{F}(\tau)$.

   (b) For Strategy 2, solve Eq. (2.57) with initial condition Eq. (2.27) for $\Delta\mathbf{y}(\tau)$; substitute $\Delta\mathbf{y}(\tau)$ and $C(t)$ into the feedback control law (Eq. (2.53)) to determine $\Delta\mathbf{F}(\tau)$.

5. For both Strategies, with the improved control field $\mathbf{F}(\tau) = \mathbf{F}_0(\tau) + \Delta\mathbf{F}(\tau)$, numerically integrate the Schrodinger equation to determine the new propagator $U(\tau, -\tau_0/2)$, and the improved gate $U(\tau_0/2, -\tau_0/2)$.

6. For both Strategies, calculate $Tr\,P$ for the new gate. This gives: (i) an upper bound on the new gate error probability $P_e \leq Tr\,P$, and (ii) the new gate fidelity $\mathcal{F} = 1 - (1/2^{n+1})Tr\,P$.

3.3 Ideal Results

Here I illustrate the use of neighboring optimal control to improve the performance of a good quantum gate. In this section I examine performance improvements under ideal control, while Section 3.4 considers the robustness of these improvements to some important control imperfections.

3.3.1 Gate Performance Improvement: Ideal Control

As noted in Section 2.5, I use: (i) Strategy 1 to determine the performance improvements for the one-qubit gates in $\mathcal{G}_U$; and (ii) Strategy 2 for the two-qubit modified controlled-phase gate. I found that both strategies produce a gate satisfying $U(\tau_0/2) = U_{tgt} + \mathcal{O}(\Delta^2)$. Here I use the numerical simulation procedure described in Section 3.2 to determine the small residual error in a one/two-qubit gate $U(\tau_0)$.

3.3.1.1 One-qubit Gates

For a given one-qubit TRP gate, the nominal control field $\mathbf{F}_0(\tau)$ is fixed by the parameters λ, η_4 and $\tau_0 = aT/b$. This determines the nominal Hamiltonian

$H_0(\tau) = -\boldsymbol{\sigma} \cdot \mathbf{F}_0(\tau)$, and numerical integration of the Schrodinger equation

$$i\frac{d}{d\tau}U_0 = H_0(\tau)U_0 \tag{3.11}$$

determines the nominal state trajectory $U_0(\tau)$. In all one-qubit simulations $\tau_0 = 160$ [50]. Following the simulation protocol, $U_0(\tau)$ is used to determine $\delta\beta$ and $\mathbf{w}$, as well as the matrix $G(\tau)$. Eq. (2.30) is then used to determine the control modification $\Delta\mathbf{F}(\tau)$, and thus the improved control field $\mathbf{F}(\tau) = \mathbf{F}_0(\tau) + \Delta\mathbf{F}(\tau)$. The new Hamiltonian is $H(\tau) = -\boldsymbol{\sigma} \cdot \mathbf{F}(\tau)$, and numerical integration of the Schrodinger equation

$$i\frac{d}{d\tau}U = H(\tau)U \tag{3.12}$$

determines the improved state trajectory $U(\tau)$. The improved one-qubit gate is then $U(\tau = \tau_0/2)$. With the new gate in hand I determine $Tr\,P$ which then provides an upper bound on the gate error probability $P_e \leq Tr\,P$. If so desired, one can also calculate the gate fidelity $\mathcal{F} = 1 - (1/4)Tr\,P$. Below I present values for the TRP sweep parameters η_4 and λ I used to provide the good gate $U_0(\tau_0/2)$, together with the NOC performance gains for ideal control, for all the one-qubit gates in $\mathcal{G}_U$.

Hadamard gate

The TRP sweep parameters values I used to produce a good approximation to the Hadamard gate are $\lambda = 7.820$ and $\eta_4 = 1.792 \times 10^{-4}$. These values, together with the dimensionless inversion time $\tau_0 = 160$, fix the TRP control field $\mathbf{F}_0(\tau)$ which then implements the following unitary gate:

$$U_{0,H} = \begin{pmatrix} 0.7112 + 0.0000\,i & 0.7030 - 0.0016\,i \\ 0.7030 + 0.0016\,i & -0.7112 + 0.0000\,i \end{pmatrix}.$$

with $TrP = 1.12 \times 10^{-4}$, and thus a gate error probability $P_e \leq 1.12 \times 10^{-4}$.

To apply the NOC, I first need to verify that the Strategy 1 illustrated in Section 2.5.1 is applicable, *i.e.* to check if $Tr\left[U_0^\dagger(\tau_0/2)U_{tgt}\right] = 2 + \mathcal{O}(\Delta^2)$ holds. With $U_0(\tau = \tau_0/2) = U_{0,H}$ and $U_{tgt} = U_H = (1/\sqrt{2})\,(\sigma_x + \sigma_z)$, then

$$Tr\left[U_0^\dagger(\tau_0/2)U_{tgt}\right] = 2 + 6.7615 \times 10^{-5}.$$

Recall that $\delta\beta = i\left[U_0^\dagger(\tau_0/2)U_{tgt} - I\right]$. Using the max-norm $\|U\| = \max_{i,j}|U_{ij}|$, it can be shown that $\|\delta\beta\| = 0.0081$. This sets the scale for small quantities introduced in Section 2: $\Delta = \|\delta\beta\|$. Thus $\Delta^2 = 6.561 \times 10^{-5}$, and so

$$Tr\left[U_0^\dagger(\tau_0/2)U_{tgt}\right] = 2 + \mathcal{O}(\Delta^2),$$

and so Eq. (2.49) is verified.

Numerical integration of the Schrodinger equation (see Eq. (3.11)) with $H_0(\tau) = -\boldsymbol{\sigma}\cdot\mathbf{F}_0(\tau)$ and $\mathbf{F}_0(\tau)$ fixed by the TRP sweep parameter values λ and η_4 given above determines the TRP state trajectory $U_0(\tau)$. With $U_0(\tau)$ known, $\mathbf{w} = \Delta\boldsymbol{\beta}/20$ and the matrix $G(\tau)$ are determined, and Eq. (2.30) then determines the control modification $\Delta\mathbf{F}(\tau)$. Finally, an improved gate $U(\tau = \tau_0/2)$ is produced by the improved control field $\mathbf{F}(\tau) = \mathbf{F}_0(\tau) + \Delta\mathbf{F}(\tau)$, with $TrP = 1.04 \times 10^{-8}$, and thus a gate error probability satisfying $P_e \leq 1.04 \times 10^{-8}$. I see that use of NOC has produced a *four order-of-magnitude* reduction in the gate error probability compared to the starting TRP gate for which $P_e \leq 1.12 \times 10^{-4}$. The error probability for the improved gate is *four orders-of-magnitude* less than the target accuracy threshold of 10^{-4}. Because P_e is so small, I do not write out the unitary matrix produced by the numerical

simulation as it agrees with the target Hadamard unitary matrix to 6 significant figures.

NOT gate

The TRP sweep parameters $\lambda = 6.965$ and $\eta_4 = 2.189 \times 10^{-4}$ produce the following unitary gate, which is a good approximation to the NOT gate:

$$U_{0,NOT} = \begin{pmatrix} -0.0014 + 0.0000\,i & 1.0000 + 0.0054\,i \\ 1.0000 - 0.0054\,i & 0.0014 + 0.0000\,i \end{pmatrix}.$$

with $TrP = 6.27 \times 10^{-5}$.

With $U_0(\tau = \tau_0/2) = U_{0,NOT}$ and $U_{tgt} = U_{NOT} = \sigma_x$, I find that

$$Tr\ \left[U_0^\dagger(\tau_0/2)U_{tgt}\right] = 2 + 3.2000 \times 10^{-5}.$$

Here $\|\delta\beta\| = 0.0054$ and so $\Delta^2 = 2.92 \times 10^{-5}$. Thus

$$Tr\ \left[U_0^\dagger(\tau_0/2)U_{tgt}\right] = 2 + \mathcal{O}(\Delta^2).$$

Implementing the above numerical simulation protocol using the TRP approximation to the modified phase gate as the starting point returns an improved gate with $TrP = 8.58\times10^{-9}$, and thus a gate error probability satisfying $P_e \leq 8.58\times10^{-9}$. I do not write out the unitary matrix produced by the numerical simulation as it agrees with the target NOT gate to 6 significant figures.

Modified $\pi/8$ gate

The TRP sweep parameters $\lambda = 8.465$ and $\eta_4 = 1.675 \times 10^{-4}$ produce the

following unitary gate, which is a good approximation to the $V_{\pi/8}$ gate:

$$U_{0,\pi/8} = \begin{pmatrix} -0.0061 + 0.0000\,i & 0.9204 + 0.3910\,i \\ 0.9204 - 0.3910\,i & 0.0061 + 0.0000\,i \end{pmatrix}.$$

with $TrP = 2.13 \times 10^{-4}$.

With $U_0(\tau = \tau_0/2) = U_{0,\pi/8}$ and $U_{tgt} = V_{\pi/8} = \cos(\pi/8)\sigma_x - \sin(\pi/8)\sigma_y$, I find that

$$Tr\,\left[U_0^\dagger(\tau_0/2)U_{tgt}\right] = 2 + 1.2034 \times 10^{-4}.$$

Here $\|\delta\beta\| = 0.0091$ and so $\Delta^2 = 8.2810 \times 10^{-5}$. Thus

$$Tr\,\left[U_0^\dagger(\tau_0/2)U_{tgt}\right] = 2 + \mathcal{O}(\Delta^2).$$

Implementing the above numerical simulation protocol using the TRP approximation to the $\pi/8$ gate as the starting point returns an improved gate with $TrP = 1.06 \times 10^{-8}$, and thus a gate error probability satisfying $P_e \leq 1.06 \times 10^{-8}$. I do not write out the unitary matrix produced by the numerical simulation as it agrees with the target modified $\pi/8$ gate to 6 significant figures.

Modified phase gate

The TRP sweep parameters $\lambda = 8.073$ and $\eta_4 = 1.666 \times 10^{-4}$ produce the following unitary gate, which is a good approximation to the modified phase gate:

$$U_{0,P} = \begin{pmatrix} 0.0051 + 0.0000\,i & 0.7171 + 0.6969\,i \\ 0.7171 - 0.6969\,i & -0.0051 + 0.0000\,i \end{pmatrix}.$$

with $TrP = 4.62 \times 10^{-4}$.

With $U_0(\tau = \tau_0/2) = U_{0,P}$ and $U_{tgt} = V_P = (1/\sqrt{2})\,(\sigma_x - \sigma_y)$, I find that

$$Tr\,\left[U_0^\dagger(\tau_0/2)U_{tgt}\right] = 2 + 2.3131 \times 10^{-4}.$$

Here $\|\delta\beta\| = 0.0054$ and so $\Delta^2 = 2.0449 \times 10^{-4}$. Thus

$$Tr\left[U_0^\dagger(\tau_0/2)U_{tgt}\right] = 2 + \mathcal{O}(\Delta^2).$$

Implementing the above numerical simulation protocol using the TRP approximation to the modified phase gate as the starting point returns an improved gate with $TrP = 1.08\times10^{-8}$, and thus a gate error probability satisfying $P_e \leq 1.08\times10^{-8}$. I do not write out the unitary matrix produced by the numerical simulation as it agrees with the target modified phase gate to 6 significant figures.

3.3.1.2 Two-qubit Modified controlled-phase gate

As seen in Appendix A, the two-qubit nominal Hamiltonian $H_0^2(\tau)$ I used to produce a good approximation to the two-qubit modified controlled phase gate V_{cp} is specified by the TRP sweep parameters λ, η_4, and τ_0, as well as the parameters $d_1, \ldots, d_4$ and c_4. All two-qubit simulations used $\tau_0 = 120$. Table 3.1 lists the values for the control parameters that I used to determine the two-qubit nominal Hamiltonian $H_0^2(\tau)$ to produce a good approximation to the target modified controlled-phase gate V_{cp}. Ref. [42] describes the optimization procedure used to determine the control parameter values appearing in Table 3.1.

The unitary gate generated by the TRP control field fixed by the parameters

Table 3.1: The nominal two-qubit gate used in this paper is the modified controlled phase gate V_{cp} studied in Ref. [42]. For the reader's convenience, I tabulate the control parameter values and gate performance reported in that work. The control parameter values listed for λ, η_4, $d_1, \ldots, d_4$, and c_4 were found using simulated annealing; the TrP upper bound on the gate error probability was found using numerical simulation of the two-qubit Schrodinger dynamics; and the gate fidelity $\mathcal{F}$ follows from $Tr\,P$ (see Section 3.2). The dimensionless inversion time $\tau_0 = 120$.

λ	η_4	d_1	d_2	d_3	d_4	c_4	TrP	$\mathcal{F}$
5.1	2.4×10^{-4}	11.702	-2.6	-0.41	6.6650	5.0003	1.27×10^{-3}	0.99984

in Table 3.1 is:

$$Re(U_{0,cp}) = \begin{pmatrix} 0.9998 & 0.0155 & 0.0041 & 0.0028 \\ -0.0154 & 0.9997 & -0.0003 & 0.0021 \\ 0.0042 & -0.0002 & -0.9999 & -0.0038 \\ -0.0026 & -0.0021 & -0.0037 & 0.9999 \end{pmatrix};$$

$$Im(U_{0,cp}) = \begin{pmatrix} 0.0052 & -0.0108 & -0.0031 & -0.0017 \\ -0.0109 & 0.0064 & -0.0084 & 0.0068 \\ 0.0030 & 0.0084 & 0.0060 & -0.0079 \\ -0.0018 & 0.0068 & 0.0079 & 0.0026 \end{pmatrix}.$$

with $TrP = 1.27 \times 10^{-3}$, where $U_{0,cp} = U_0(\tau = \tau_0/2)$.

The state trajectory $U_0(\tau)$ determined by the two-qubit nominal Hamiltonian $H_0^2(\tau)$ fixed by the dimensionless control parameters appearing in Table 3.1 then serves as the input for the NOC method. I now implement Strategy 2 to determine a control modification $\Delta\mathbf{F}(\tau)$ to improve the two-qubit gate performance. For S-trategy 2 , Step 2 of the six step numerical procedure (see Section 3.2) requires the

three matrices $\mathcal{G}_1$, $\mathcal{G}_2$, and $\mathcal{G}_3$. These follow from the functional derivatives of $H_0^2(\tau)$ with respect to the components of the control field $\mathbf{F}(\tau)$:

$$\begin{cases} \mathcal{G}_1 = d_3 \left[\cos\left((\frac{d_1 b_2}{b_1 - b_2} + d_1)\tau \right) \sigma_x^1 + \sin\left((\frac{d_1 b_2}{b_1 - b_2} + d_1)\tau \right) \sigma_y^1 \right] \\ \qquad + \left[\cos\left((\frac{d_1 b_2}{b_1 - b_2})\tau \right) \sigma_x^2 + \sin\left((\frac{d_1 b_2}{b_1 - b_2})\tau \right) \sigma_y^2 \right] \\ \\ \mathcal{G}_2 = d_3 \left[\cos\left((\frac{d_1 b_2}{b_1 - b_2} + d_1)\tau \right) \sigma_y^1 - \sin\left((\frac{d_1 b_2}{b_1 - b_2} + d_1)\tau \right) \sigma_x^1 \right] \\ \qquad + \left[\cos\left((\frac{d_1 b_2}{b_1 - b_2})\tau \right) \sigma_y^2 - \sin\left((\frac{d_1 b_2}{b_1 - b_2})\tau \right) \sigma_x^2 \right] \\ \\ \mathcal{G}_3 = d_3 \sigma_z^1 + \sigma_z^2. \end{cases} \tag{3.13}$$

As noted in Step 3 of the procedure for Strategy 2, I chose $R(\tau) = I_{3\times 3}$ and $S(\tau) = I_{16\times 16}$, where $I_{n\times n}$ is the $n \times n$ identity matrix. Satisfying the Ricatti equation then required $Q(\tau) = G(\tau)G^{\dagger}(\tau)$. Carrying out the remaining steps in the numerical procedure for Strategy 2, the improved gate produced by the NOC improved control is:

$$Re(U_{cp}) = \begin{pmatrix} 1.0000 & 0.0001 & 0.0000 & 0.0024 \\ 0.0000 & 1.0000 & -0.0001 & 0.0000 \\ 0.0001 & 0.0001 & -1.0000 & -0.0001 \\ -0.0024 & 0.0000 & 0.0000 & 1.0000 \end{pmatrix};$$

$$Im(U_{cp}) = \begin{pmatrix} 0.0055 & 0.0001 & 0.0000 & -0.0016 \\ -0.0001 & 0.0014 & 0.0004 & 0.0000 \\ -0.0001 & -0.0004 & 0.0003 & 0.0000 \\ -0.0017 & 0.0000 & 0.0000 & 0.0015 \end{pmatrix}.$$

with $TrP = 5.21 \times 10^{-5}$, and an error probability P_e satisfying that $P_e \leq 5.21 \times 10^{-5}$, where $U_{cp} = U(\tau = \tau_0/2)$. The reader can directly examine the NOC improvement in U_{cp} by comparing the above unitary gate with the unimproved TRP two-qubit gate $U_{0,cp}$ found in Ref. [42].

I summarize the simulation results of the NOC improved gate performance for all target gates in $\mathcal{G}_U$ in Table 3.2. For comparison, I include the TrP upper bound on the gate error probability P_e for all gates with and without the neighboring optimal control improvements. I see that for all one-qubit gates in $\mathcal{G}_U$, NOC reduce the gate error probability by *four orders-of-magnitude* (viz. $10^{-4} \rightarrow 10^{-8}$), while for the two-qubit gate, P_e was reduced by *two orders-of-magnitude* (viz. $10^{-3} \rightarrow 10^{-5}$). NOC has thus substantially improved TRP gate performance, producing gates with error probability falling well below the target accuracy threshold of 10^{-4}.

3.3.2 Control Bandwidth

I now examine the bandwidth needed for the control modifications $\Delta\mathbf{F}(t)$ so that the NOC performance in Table 3.2 can be realized. To provide context, I note that arbitrary waveform generators (AWG) are commercially available with bandwidths as large as 5 GHz [51]. I assume that the TRP inversion time for one-

Table 3.2: Simulation results for all target gates in the universal set $\mathcal{G}_U$ for ideal control. The first column lists the target quantum gates, while the second column lists the $Tr\,P$ upper bound for the gate error probability P_e for gates whose performance is improved using neighboring optimal control (NOC). The third column lists the $Tr\,P$ upper bound for the starting TRP gates which do not use NOC. NOC has reduced the error probability for all one-qubit gates by *four orders-of-magnitude*, and by *two orders-of-magnitude* for the two-qubit controlled-phase gate. Although not included in the Table, the gate fidelity $\mathcal{F}_n$ for an n-qubit gate can be determined from $Tr\,P$ using $\mathcal{F}_n = 1 - (1/2^{n+1})Tr\,P$.

Target Gate	$P_e \leq TrP$ (with NOC)	$P_e \leq TrP$ (without NOC)
NOT	$\leq 8.58 \times 10^{-9}$	$\leq 6.27 \times 10^{-5}$
Hadamard	$\leq 1.04 \times 10^{-8}$	$\leq 1.12 \times 10^{-4}$
Modified $\pi/8$	$\leq 1.06 \times 10^{-8}$	$\leq 2.13 \times 10^{-4}$
Modified phase	$\leq 1.08 \times 10^{-8}$	$\leq 4.62 \times 10^{-4}$
Modified controlled-phase	$\leq 5.21 \times 10^{-5}$	$\leq 1.27 \times 10^{-3}$

qubit gate is $1\mu s$, and for two-qubit gate is $5\mu s$. I estimate the (dimensionless) bandwidth of the control field modification $\Delta\mathbf{F}(\tau)$ by determining the frequency $\omega_{0.1}$ at which the Fourier component module $|\Delta\mathcal{F}_x(\omega_{0.1})|$ is 10% of the peak value $|\Delta\mathcal{F}_x(0)|$, where $\Delta\mathcal{F}_x(\omega)$ is the Fourier transform of $\Delta F_x(\tau)$, the x-component of the control field modification $\Delta\mathbf{F}(\tau)$. To convert the dimensionless bandwidth $\omega_{0.1}$ into a physical bandwidth $\overline{\omega}_{0.1}$, note that the physical inversion time T corresponds to a dimensionless inversion time τ_0. Therefore, for the one-qubit gates with a physical inversion time $T = 1\mu s$ and dimensionless inversion time $\tau_0 = 160$, the physical bandwidth $\overline{\omega}_{0.1}$ is related to the dimensionless bandwidth $\omega_{0.1}$ by:

$$\frac{\overline{\omega}_{0.1}}{\omega_{0.1}} = \frac{1/T}{1/\tau_0} = \frac{160}{1\mu\text{s}} = 160\,\text{MHz}. \tag{3.14}$$

For the two-qubit gate with a physical inversion time $T = 5\mu s$ and dimensionless inversion time $\tau_0 = 120$, the connection between physical and dimensionless bandwidth is

$$\frac{\overline{\omega}_{0.1}}{\omega_{0.1}} = \frac{1/T}{1/\tau_0} = \frac{120}{5\mu\text{s}} = 24\,\text{MHz}. \tag{3.15}$$

With these preliminaries out of the way, I present the bandwidth results for all the NOC improved gates in $\mathcal{G}_U$.

1. Hadamard gate: Figure 3.1 shows the x-component of the dimensionless control field modification $\Delta F_x(\tau)$ as a function of the dimensionless time τ for the Hadamard gate as target. Figure 3.2 shows its Fourier transform module $|\Delta\mathcal{F}_x(\omega)|$. Examination of the numerical data used to produce Figure 3.2 gives $\omega_{0.1} = 4.0$. Thus, it follows from Eq. (3.14) that the physical bandwidth needed to implement

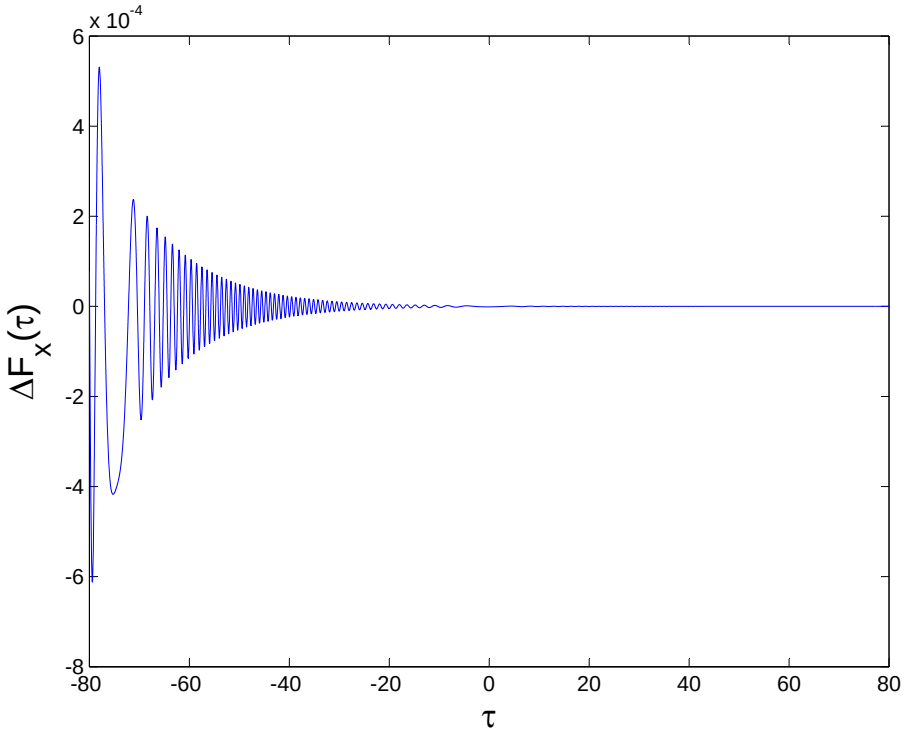

Figure 3.1: The x-component dimensionless control modification $\Delta F_x(\tau)$ used to implement a neighboring optimal control improved approximation to the Hadamard gate. Here τ is the dimensionless time.

the control modification $\Delta\mathbf{F}(t)$ for the Hadamard gate is $\overline{\omega}_{0.1} = (160MHz)(4.0) = 640MHz$. This is within the range of some commercially available AWGs.

2. NOT gate: Figure 3.3 shows the x-component of the dimensionless control field modification $\Delta F_x(\tau)$ as a function of the dimensionless time τ for the NOT gate. Figure 3.4 shows its Fourier transform module $|\Delta\mathcal{F}_x(\omega)|$. Examination of the data used to produce Figure 3.4 gives $\omega_{0.1} = 0.8$. Eq. (3.14) then gives a physical bandwidth of $\overline{\omega}_{0.1} = 130$ MHz.

3. Modified phase gate: Figure 3.5 shows the x-component of the dimen-

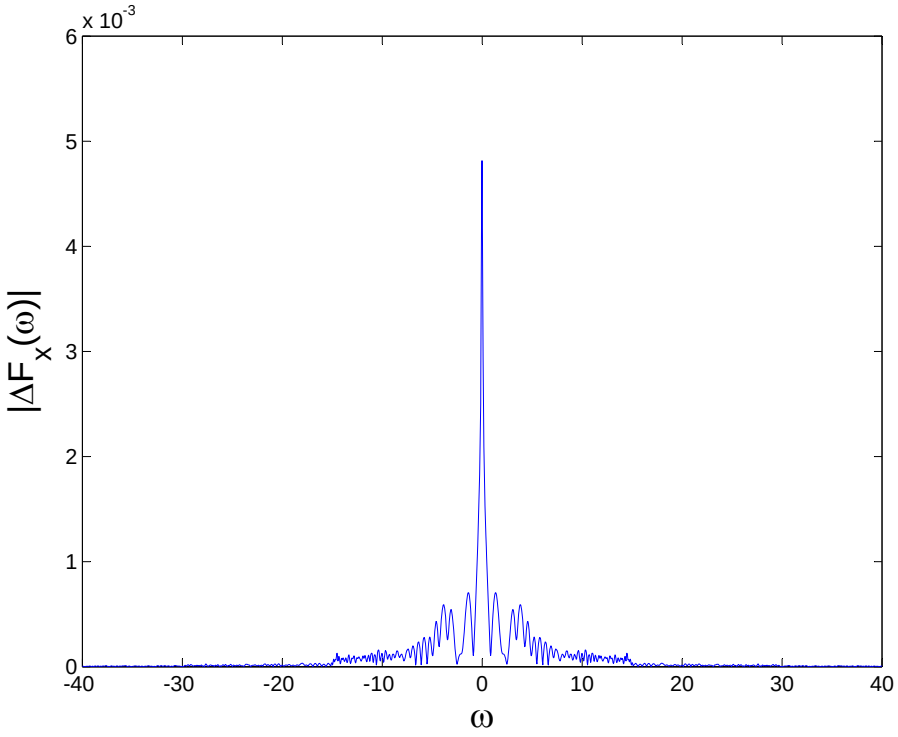

Figure 3.2: The Fourier transform module $|\Delta\mathcal{F}_x(\omega)|$ of the x-component dimensionless control modification $\Delta F_x(\tau)$ for the Hadamard Gate as target. Here ω is the dimensionless frequency.

sionless control field modification $\Delta F_x(\tau)$ as a function of the dimensionless time τ for the modified phase gate. Figure 3.6 shows its Fourier transform module $|\Delta\mathcal{F}_x(\omega)|$. Examination of the data used to produce Figure 3.6 gives $\omega_{0.1} = 1.9$, which, using Eq. (3.14), gives a physical bandwidth of $\overline{\omega}_{0.1} = 300$ MHz.

4. Modified $\pi/8$ gate: Figure 3.7 shows the x-component of the dimensionless control field modification $\Delta F_x(\tau)$ as a function of the dimensionless time τ for the modified $\pi/8$ gate. Figure 3.8 shows its Fourier transform module $|\Delta\mathcal{F}_x(\omega)|$. Examination of the data used to produce Figure 3.8 gives $\omega_{0.1} = 1.3$, which, using

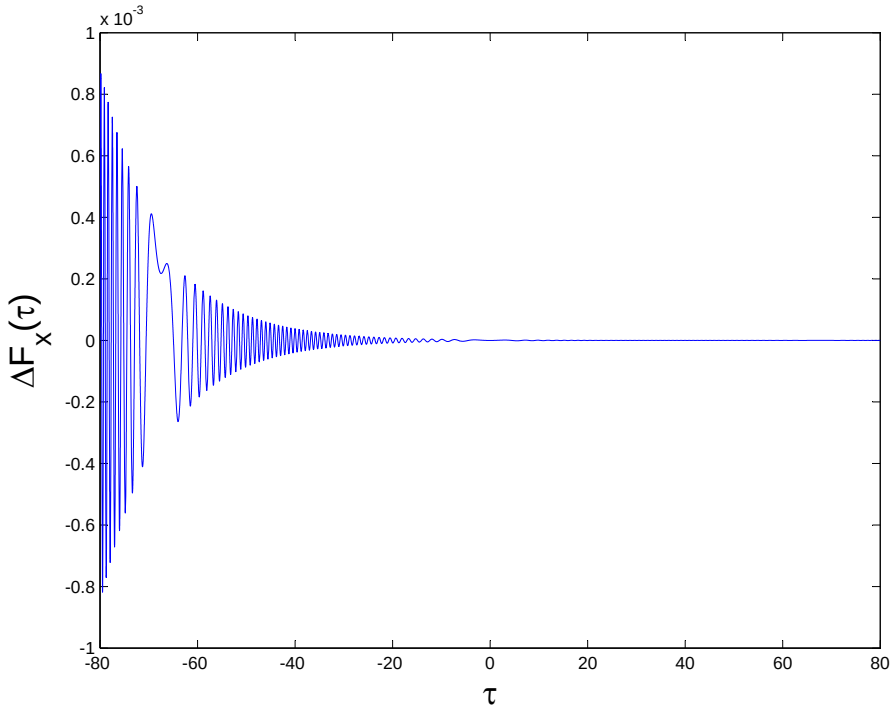

Figure 3.3: The x-component of the dimensionless control field modification $\Delta F_x(\tau)$ for the NOT gate versus the dimensionless time τ.

Eq. (3.14), gives a physical bandwidth of $\overline{\omega}_{0.1} = 210$ MHz.

5. Modified controlled-phase gate: Figure 3.9 shows the x-component of the dimensionless control field modification $\Delta F_x(\tau)$ as a function of the dimensionless time τ for the modified controlled-phase gate. Figure 3.11 shows its Fourier transform module $|\Delta \mathcal{F}_x(\omega)|$. Examination of the data used to produce Figure 3.11 gives $\omega_{0.1} = 34$, which, using Eq. (3.15), gives a physical bandwidth of $\overline{\omega}_{0.1} = 820$ MHz.

To summarize, Table 3.3 lists the dimensionless and physical bandwidth required to implement the control modification for each of the target gates in $\mathcal{G}_U$. I note here that the bandwidth required to implement the neighboring optimal control

Table 3.3: Bandwidth requirements for neighboring optimal control improved quantum gates. The dimensionful values assume a one-qubit (two-qubit) gate time of 1μs (5μs). Note that the bandwidth for the nominal TRP control field $\mathbf{F}_0(t)$ is less than 1% of the bandwidth of the control modification $\Delta\mathbf{F}(t)$. I thus use the bandwidth for $\Delta\mathbf{F}(t)$ as the total bandwidth. Column 1 lists the target gates in $\mathcal{G}_U$; column 2 the dimensionless bandwidth $\omega_{0.1}$; while column 3 gives the dimensionful bandwidth $\overline{\omega}_{0.1}$.

Target Gate	$\omega_{0.1}$ (dimensionless)	$\overline{\omega}_{0.1}$ (MHz)
NOT	0.80	130
Modified $\pi/8$	1.3	210
Modified phase	1.9	300
Hadamard	4.0	640
Modified controlled-phase	34	820

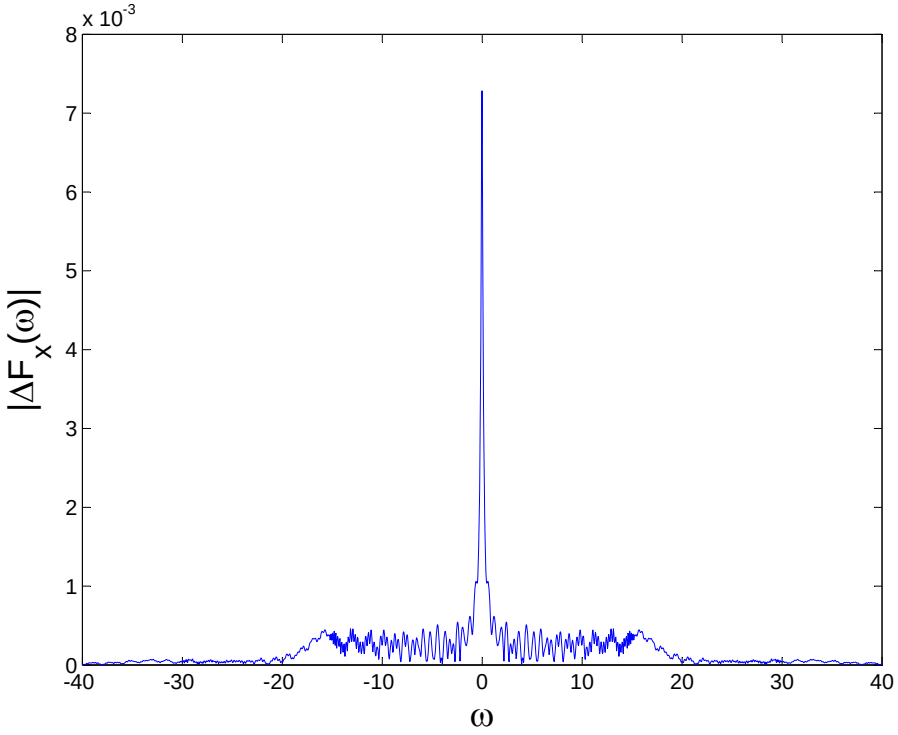

Figure 3.4: The Fourier transform module $|\Delta\mathcal{F}_x(\omega)|$ of the x-component dimensionless control field modification for the NOT gate versus the dimensionless frequency ω.

performance improvements for all gates in $\mathcal{G}_U$ is within the range of commercially available AWGs. Note that Eqs. (3.14-3.15) indicate that the dimensionful bandwidth $\overline{\omega}_{0.1}$ scales as $1/T$ in the TRP inversion time T. Thus, if relaxation an dephaseing do not prevent it, one can reduce the bandwidth of the control modification $\Delta\mathbf{F}(t)$ by increasing the TRP inversion time (*viz.* gate time) T.

3.4 Robustness to Control Imperfections

In this section I examine the robustness of the neighboring optimal control (NOC) performance gains found in Section 3.3 to two important control imper-

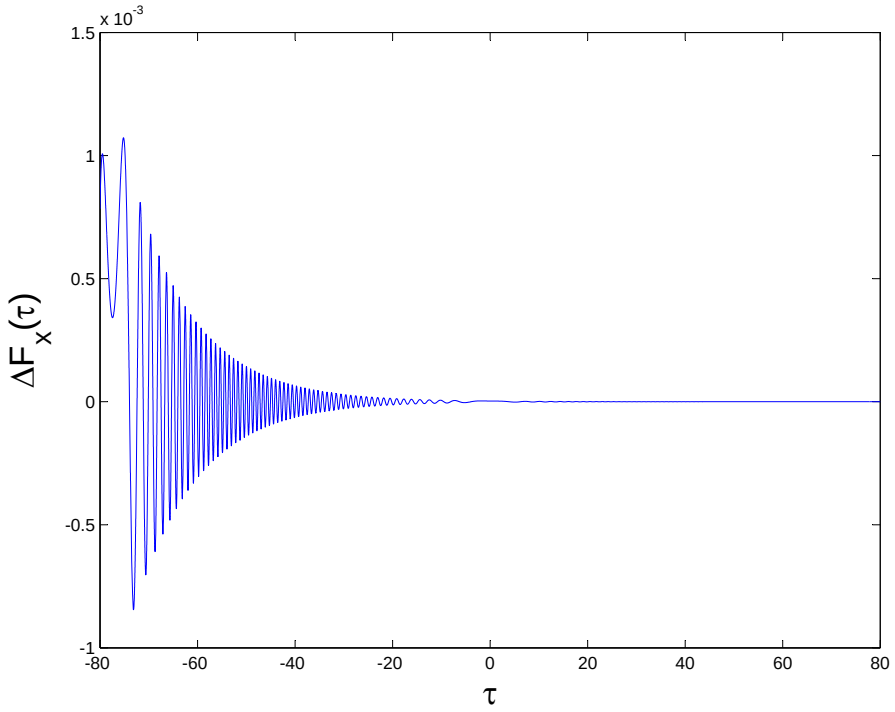

Figure 3.5: The x-component of the dimensionless control field modification $\Delta F_x(\tau)$ for the modified phase gate versus the dimensionless time τ.

fections. In Section 3.4.1 I examine the impact of control parameters with finite precision; while in Section 3.4.2 I consider phase noise in the nominal control field.

3.4.1 Finite Parameter Precision

The NOC formalism introduced above requires an input state trajectory $U_0(\tau)$ that yields a good approximation to a target gate U_{tgt}. The control modification $\Delta\mathbf{F}(\tau)$ determined by the formalism is optimum for $U_0(\tau)$, or equivalently, for the nominal control $\mathbf{F}_0(\tau)$. Alteration of the nominal control field $\mathbf{F}_0(\tau) \rightarrow \mathbf{F}_0'(\tau)$ alters the state trajectory $U_0(\tau) \rightarrow U_0'(\tau)$, with the result that the control modification $\Delta\mathbf{F}(\tau)$ may no longer be optimal for the altered trajectory $U_0'(\tau)$. Because the

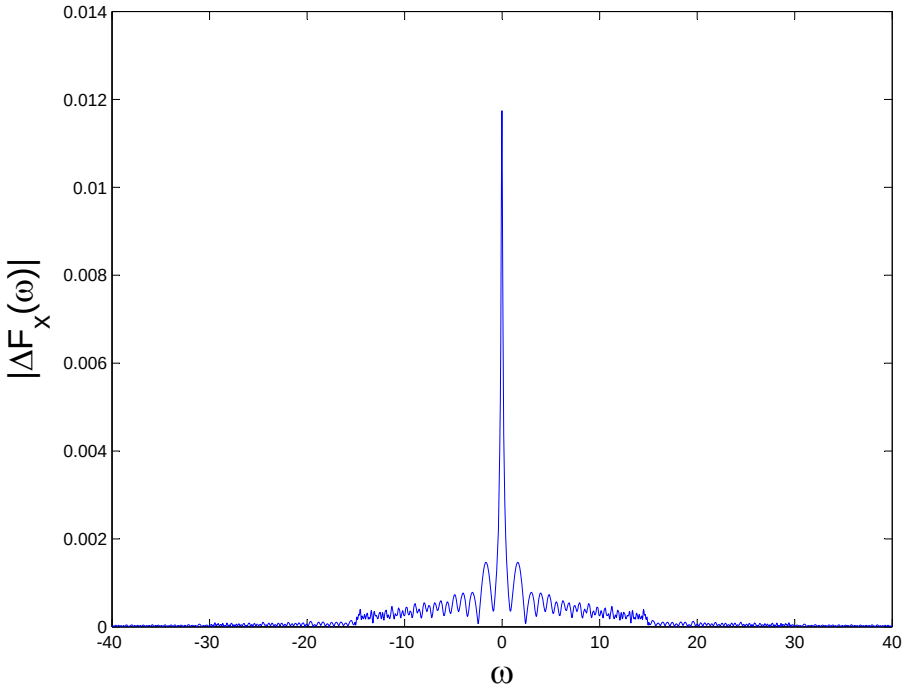

Figure 3.6: The Fourier transform module $|\Delta\mathcal{F}_x(\omega)|$ of the x-component dimensionless control field modification for the modified phase gate versus the dimensionless frequency ω.

hardware used to produce $\mathbf{F}_0(\tau)$ has limited precision, it becomes important to determine the degree of precision to which the control parameters must be specified if the NOC performance gains are to survive the limitation of finite-precision control.

For the one-qubit gates in $\mathcal{G}_U$, the optimum values for the TRP sweep parameter λ and η_4 presented in Section 3.3.1.1 are used to produce the nominal control filed $\mathbf{F}_0(\tau)$ and state trajectory $U_0(\tau)$, for which the nominal gate $U_0(\tau_0/2)$ is a good approximation to the target gate in $\mathcal{G}_U$, with the gate error probability satisfying $P_e \leq TrP \sim 10^{-4}$. For these control parameter values, NOC determines the control modification $\Delta\mathbf{F}(\tau)$ (see Section 3.3.1) which produces a new gate with

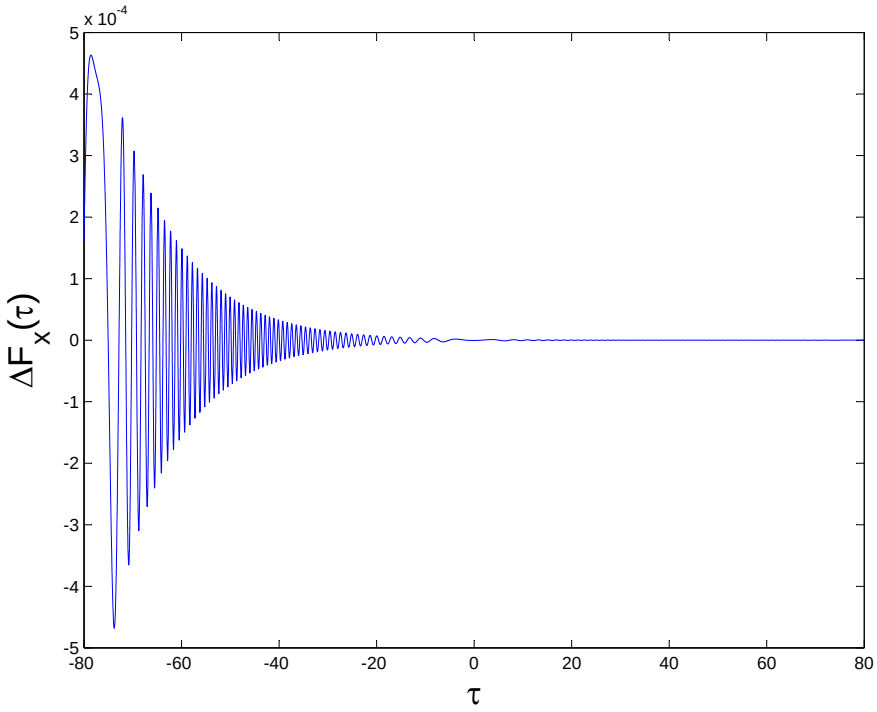

Figure 3.7: The x-component of the dimensionless control field modification $\Delta F_x(\tau)$ for the modified $\pi/8$ gate versus the dimensionless time τ.

$P_e \leq TrP \sim 10^{-8}$. To examine the robustness of this performance improvement, I shift λ (η_4) away from its optimum value by 1 in its fourth significant digit, while keeping η_4 (λ) at optimum. This shift causes $\mathbf{F}_0(\tau) \rightarrow \mathbf{F}'_0(\tau)$. I then numerically simulate the Schrodinger dynamics driven by the Hamiltonian $H(\tau) = -\boldsymbol{\sigma} \cdot \mathbf{F}'(\tau)$, where the new control field $\mathbf{F}'(\tau) = \mathbf{F}'_0(\tau) + \Delta\mathbf{F}(\tau)$, and $\Delta\mathbf{F}(\tau)$ is the NOC modification that corresponds to the nominal control field $\mathbf{F}_0(\tau)$. The TrP upper bound for the gate error probability P_e of the new gate $U(\tau_0/2)$ yielded by this new control field $\mathbf{F}'(\tau)$ is then calculated. Below I present how the TrP upper bound for the gate error probability P_e varies as I change λ (η_4) by one in its least significant digit, while keeping η_4 (λ) at optimum, for all one-qubit gates in $\mathcal{G}_U$.

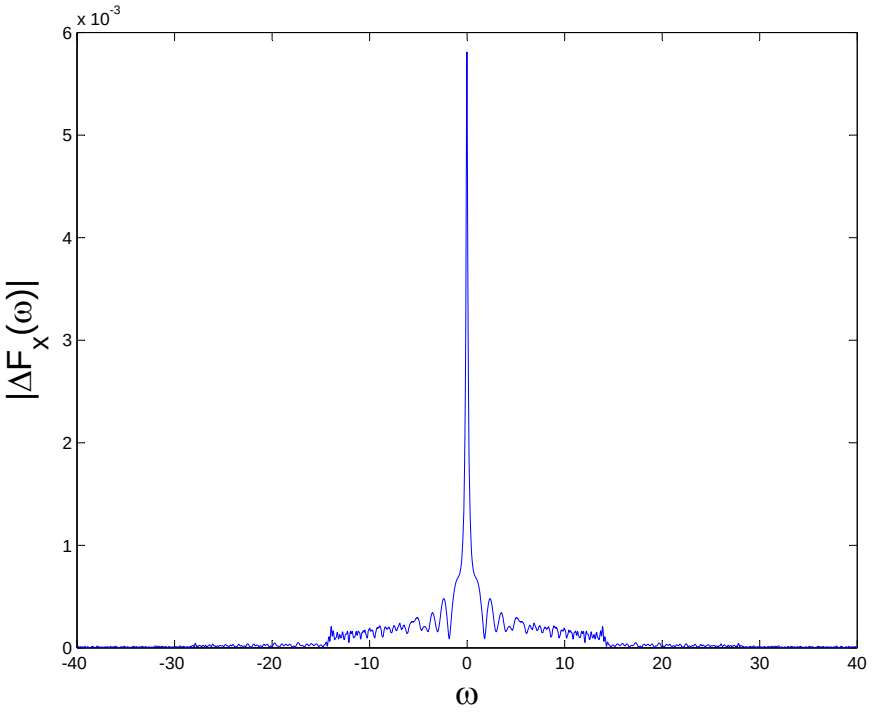

Figure 3.8: The Fourier transform module $|\Delta\mathcal{F}_x(\omega)|$ of the x-component dimensionless control field modification for the modified $\pi/8$ gate versus the dimensionless frequency ω.

Hadamard gate: For the Hadamard gate, the optimum TRP control parameters are $\lambda = 7.820$ and $\eta_4 = 1.792 \times 10^{-4}$. For these control parameter values, the control modification optimum $\Delta\mathbf{F}(\tau)$ determined by NOC yields an improved gate with $P_e \leq 1.04 \times 10^{-8}$. Shifting λ (η_4) away from its optimum value by 1 in its fourth significant digit while keeping η_4 (λ) at optimum causes the control $\mathbf{F}(\tau) \rightarrow \mathbf{F}'(\tau) = \mathbf{F}'_0(\tau) + \Delta\mathbf{F}(\tau)$, and the resulting TrP upper bound for the gate error probability P_e of the gate yielded by this new control can be calculated from numerical simulation. Tables 3.4 and 3.5 show how the $Tr\,P$ upper bound for the gate error probability P_e changes due to a small shift in λ (η_4) away from its opti-

Table 3.4: Sensitivity of TrP to a small variation of λ away from its optimum value for the one-qubit Hadamard gate. For all λ values, η_4 is maintained at its optimum value $\eta_4 = 1.792 \times 10^{-4}$. Column 2 (3) shows the variation of $Tr\,P$ when the control field includes (omits) the NOC control modification $\Delta\mathbf{F}(\tau)$.

λ	TrP (with NOC)	TrP (without NOC)
7.819	2.62×10^{-4}	8.15×10^{-4}
7.820	1.04×10^{-8}	1.12×10^{-4}
7.821	4.44×10^{-4}	2.07×10^{-3}

Table 3.5: Sensitivity of TrP to a small variation of η_4 away from its optimum value for the one-qubit Hadamard gate. For all η_4 values, λ is maintained at its optimum value $\lambda = 7.820$. Column 2 (3) shows the variation of $Tr\,P$ when the control field includes (omits) the NOC control modification $\Delta\mathbf{F}(\tau)$.

η_4	TrP (with NOC)	TrP (without NOC)
1.791×10^{-4}	5.75×10^{-3}	2.86×10^{-2}
1.792×10^{-4}	1.04×10^{-8}	1.12×10^{-4}
1.793×10^{-4}	7.76×10^{-3}	3.11×10^{-2}

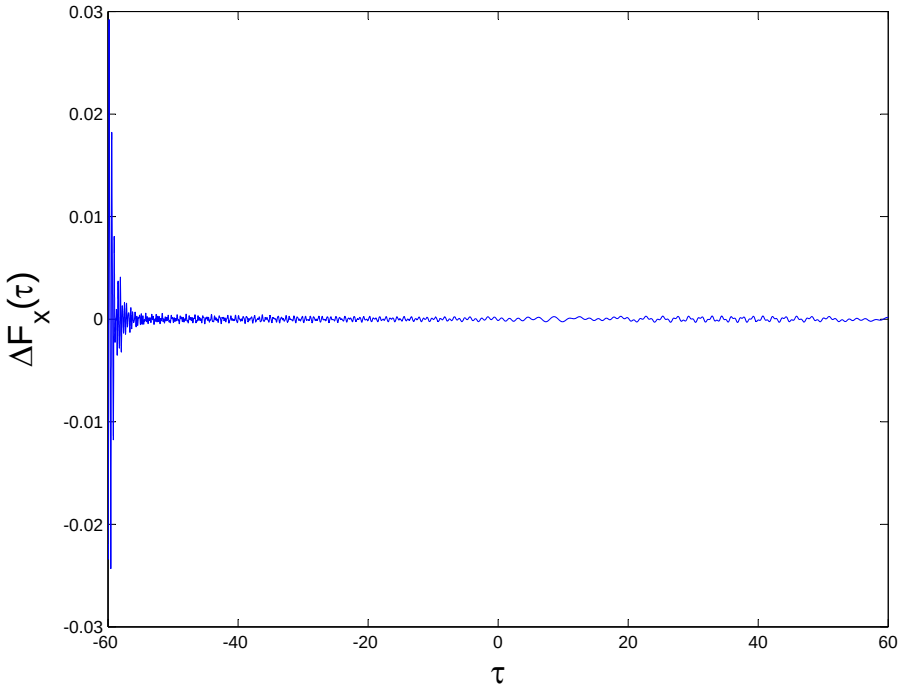

Figure 3.9: The x-component of the dimensionless control field modification $\Delta F_x(\tau)$ for the modified controlled-phase gate versus the dimensionless time τ.

mum value. For comparison, I also show how $Tr\,P$ changes when the new control field does not contain the NOC modification: $\mathbf{F}'(\tau) = \mathbf{F}'_0(\tau)$. It is clear from these Tables that both λ and η_4 must be controllable to better than one part in $10,000$ if the NOC performance gains are to be realized. Such control parameter precision is attainable using an AWG with 14-bit vertical resolution (viz. one part in $2^{14} = 16,384$). Such AWGs are available commercially [52]. Note that 13-bit precision corresponds to a precision of one part in $2^{13} = 8192$, and so to an uncertainty in the fourth significant digit. Thus with less than 14-bits of precision, Tables 3.4 and 3.5 indicate that the NOC performance gains will be washed out by the uncertainty in the least significant digit of λ and η_4. Lastly, notice that the NOC

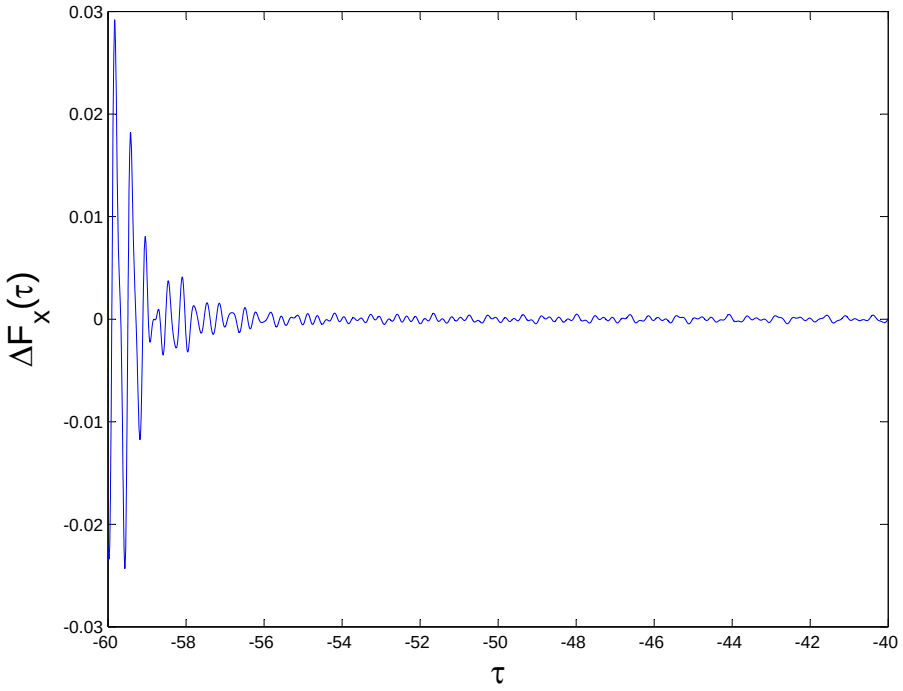

Figure 3.10: The x-component of the dimensionless control field modification $\Delta F_x(\tau)$ for the modified controlled-phase gate versus the dimensionless time τ, zoomed for $\tau \in [-60, -40]$.

improved Hadamard gate outperforms the unimproved nominal TRP gate, even in the presence of finite precision control parameters.

NOT gate: For the NOT gate, NOC delivered a gate with $P_e \leq 8.58\times10^{-9}$. In Tables 3.6 and 3.7 I show how the $Tr\,P$ upper bound on the gate error probability ($P_e \leq Tr\,P$) changes due to a small shift in λ and η_4 away from its optimum value, respectively. I show the variation in $Tr\,P$ when the NOC modification is both included and omitted. As with the Hadamard gate, both λ and η_4 must be controlled to better than one part in $10,000$ to realize the NOC performance gains. As shown in the Hadamard gate discussion, this is possible using an AWG with at

Table 3.6: Sensitivity of TrP to a small variation of λ away from its optimum value for the one-qubit NOT gate. For all λ values, η_4 is maintained at its optimum value $\eta_4 = 2.189 \times 10^{-4}$. Column 2 (3) shows the variation of $Tr\,P$ when the control field includes (omits) the NOC modification $\Delta\mathbf{F}(\tau)$. Recall that $Tr\,P$ upper bounds the gate error probability $P_e \leq Tr\,P$.

λ	TrP (with NOC)	TrP (without NOC)
6.964	8.75×10^{-4}	2.12×10^{-3}
6.965	8.58×10^{-9}	6.27×10^{-5}
6.966	3.99×10^{-4}	3.82×10^{-4}

Table 3.7: Sensitivity of TrP to a small variation of η_4 away from its optimum value for the one-qubit NOT gate. For all η_4 values, λ is maintained at its optimum value $\lambda = 6.965$. Column 2 (3) shows the variation of $Tr\,P$ when the control field includes (omits) the NOC modification $\Delta\mathbf{F}(\tau)$. Recall that $Tr\,P$ upper bounds the gate error probability $P_e \leq Tr\,P$.

η_4	TrP (with NOC)	TrP (without NOC)
2.188×10^{-4}	6.50×10^{-3}	1.55×10^{-2}
2.189×10^{-4}	8.58×10^{-9}	6.27×10^{-5}
2.190×10^{-4}	9.80×10^{-3}	3.28×10^{-2}

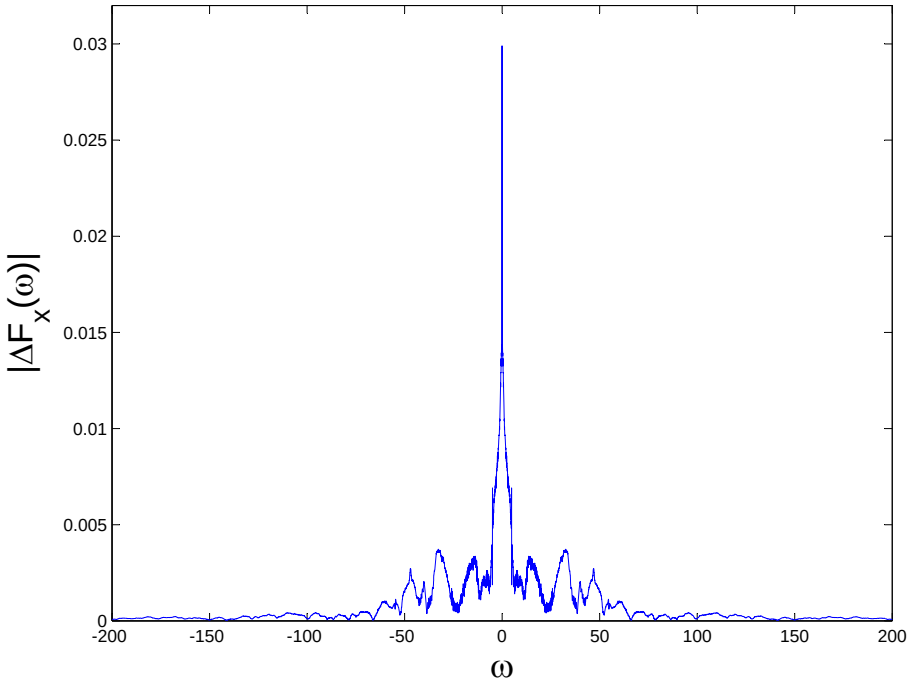

Figure 3.11: The Fourier transform module $|\Delta\mathcal{F}_x(\omega)|$ of the x-component dimensionless control field modification for the modified controlled-phase gate versus the dimensionless frequency ω .

least 14-bit vertical resolution. Using less precision will give rise to uncertainty in the fourth significant digit, and to a washing out of the NOC performance gains.

Modified $\pi/8$ gate: For the modified $\pi/8$ gate, NOC delivered a gate with $P_e \leq 1.06 \times 10^{-8}$. In Tables 3.8 and 3.9 I show how the $Tr\,P$ upper bound on the gate error probability ($P_e \leq Tr\,P$) changes due to a small shift in λ and η_4 away from its optimum value, respectively. I show the variation in $Tr\,P$ when the NOC modification is both included and omitted. As with the Hadamard gate, both λ and η_4 must be controlled to better than one part in $10,000$ to realize the NOC performance gains. This is possible using an AWG with at least 14-bit vertical

Table 3.8: Sensitivity of TrP to a small variation of $\lambda 4$ away from its optimum value for the one-qubit modified $\pi/8$ gate. For all λ values, η_4 is maintained at its optimum value $\eta_4 = 1.675 \times 10^{-4}$. Column 2 (3) shows the variation of $Tr\,P$ when the control field includes (omits) the NOC modification $\Delta\mathbf{F}(\tau)$. Recall that $Tr\,P$ upper bounds the gate error probability $P_e \leq Tr\,P$.

λ	TrP (with NOC)	TrP (without NOC)
8.464	6.77×10^{-4}	2.12×10^{-3}
8.465	1.06×10^{-8}	2.13×10^{-4}
8.466	7.32×10^{-4}	4.58×10^{-4}

Table 3.9: Sensitivity of TrP to a small variation of η_4 away from its optimum value for the one-qubit modified $\pi/8$ gate. For all η_4 values, λ is maintained at its optimum value $\lambda = 8.465$. Column 2 (3) shows the variation of $Tr\,P$ when the control field includes (omits) the NOC modification $\Delta\mathbf{F}(\tau)$. Recall that $Tr\,P$ upper bounds the gate error probability $P_e \leq Tr\,P$.

η_4	TrP (with NOC)	TrP (without NOC)
1.674×10^{-4}	7.10×10^{-3}	4.99×10^{-2}
1.675×10^{-4}	1.06×10^{-8}	2.13×10^{-4}
1.676×10^{-4}	7.30×10^{-3}	3.90×10^{-2}

Table 3.10: Sensitivity of TrP to a small variation of λ away from its optimum value for the one-qubit modified phase gate. For all λ values, η_4 is maintained at its optimum value $\eta_4 = 1.666 \times 10^{-4}$. Column 2 (3) shows the variation of $Tr\,P$ when the control field includes (omits) the NOC modification $\Delta\mathbf{F}(\tau)$. Recall that $Tr\,P$ upper bounds the gate error probability $P_e \leq Tr\,P$.

λ	TrP (with NOC)	TrP (without NOC)
8.072	1.97×10^{-4}	1.17×10^{-3}
8.073	1.08×10^{-8}	4.62×10^{-4}
8.074	5.82×10^{-4}	3.20×10^{-3}

Table 3.11: Sensitivity of TrP to a small variation of η_4 away from its optimum value for the one-qubit modified phase gate. For all η_4 values, λ is maintained at its optimum value $\lambda = 8.073$. Column 2 (3) shows the variation of $Tr\,P$ when the control field includes (omits) the NOC modification $\Delta\mathbf{F}(\tau)$. Recall that $Tr\,P$ upper bounds the gate error probability $P_e \leq Tr\,P$.

η_4	TrP (with NOC)	TrP (without NOC)
1.665×10^{-4}	1.20×10^{-3}	4.42×10^{-2}
1.666×10^{-4}	1.08×10^{-8}	4.62×10^{-4}
1.667×10^{-4}	6.10×10^{-3}	5.74×10^{-2}

resolution. Using less precision will give rise to uncertainty in the fourth significant digit, and to a washing out of the NOC performance gains.

Modified phase gate: For the modified phase gate, NOC delivered a gate with $P_e \leq 1.08 \times 10^{-8}$. In Tables 3.10 and 3.11 I show how the $Tr\,P$ upper bound

on the gate error probability ($P_e \leq Tr\, P$) changes due to a small shift in λ and η_4 away from its optimum value, respectively. I show the variation in $Tr\, P$ when the NOC modification is both included and omitted. As with the Hadamard gate, both λ and η_4 must be controlled to better than one part in $10,000$ to realize the NOC performance gains. This is possible using an AWG with at least 14-bit vertical resolution. Using less precision will give rise to uncertainty in the fourth significant digit, and to a washing out of the NOC performance gains.

Two-qubit modified controlled-phase gate: For the two-qubit modified controlled-phase gate, the nominal Hamiltonian $H_0^2(\tau)$ is fixed by the dimensionless parameters listed in Table 3.1. For these control parameters, NOC delivered a gate with the gate error probability satisfying $P_e \leq 5.21 \times 10^{-5}$. To examine the robustness of this performance improvement to small variations in the control parameters and thereby determining the minimum control parameter precision needed to realize this performance improvement, I change each parameter away from its optimum value by 1 in its last significant digit, while keeping the others at optimum. Such shift causes $H_0^2(\tau) \rightarrow H_0^{2\prime}(\tau)$. I then numerically simulate the Schrodinger dynamics driven by the Hamiltonian $H^2(\tau) = H_0^{2\prime}(\tau) + \boldsymbol{\mathcal{G}} \cdot \Delta\mathbf{F}(\tau)$, where $\Delta\mathbf{F}(\tau)$ is the NOC modification that corresponds to the nominal Hamiltonian $H_0^2(\tau)$, and $\boldsymbol{\mathcal{G}} = (\mathcal{G}_1, \mathcal{G}_2, \mathcal{G}_3)$ with $\mathcal{G}_j$ given by Eq. (3.13). It was found (and also confirmed by Ref. [42]) that the performance was most sensitive to small changes in d_1, d_4 and c_4. Tables 3.12, 3.12 and 3.14 show how the TrP upper bound on the gate error probability ($P_e \leq TrP$) changes due to a small shift in the last significant digit of

Table 3.12: Sensitivity of TrP to a small variation of d_1 away from its optimum value for the two-qubit modified controlled-phase gate. For all d_1 values, the remaining control parameters appearing in Table 3.1 are maintained at the optimum values given there. Column 2 (3) shows the variation of $Tr\,P$ when the control field includes (omits) the NOC modification $\Delta\mathbf{F}(\tau)$. Recall that $Tr\,P$ upper bounds the gate error probability $P_e \leq Tr\,P$.

d_1	TrP (with NOC)	TrP (without NOC)
11.701	1.16×10^{-3}	3.36×10^{-3}
11.702	5.21×10^{-5}	1.27×10^{-3}
11.703	1.16×10^{-3}	1.43×10^{-3}

Table 3.13: Sensitivity of TrP to a small variation of d_4 away from its optimum value for the two-qubit modified controlled-phase gate. For all d_4 values, the remaining control parameters appearing in Table 3.1 are maintained at the optimum values given there. Column 2 (3) shows the variation of $Tr\,P$ when the control field includes (omits) the NOC modification $\Delta\mathbf{F}(\tau)$. Recall that $Tr\,P$ upper bounds the gate error probability $P_e \leq Tr\,P$.

d_4	TrP (with NOC)	TrP (without NOC)
6.6649	1.25×10^{-3}	3.36×10^{-3}
6.6650	5.21×10^{-5}	1.27×10^{-3}
6.6651	1.69×10^{-3}	2.97×10^{-3}

d_1, d_4 and c_4 away from their optimum value, respectively. I show the variation in TrP when the NOC modification is both included and omitted.

I note here that all d_1, d_4 and c_4 must be controlled to better than one part

Table 3.14: Sensitivity of TrP to a small variation of c_4 away from its optimum value for the two-qubit modified controlled-phase gate. For all d_1 values, the remaining control parameters appearing in Table 3.1 are maintained at the optimum values given there. Column 2 (3) shows the variation of $Tr\,P$ when the control field includes (omits) the NOC modification $\Delta\mathbf{F}(\tau)$. Recall that $Tr\,P$ upper bounds the gate error probability $P_e \leq Tr\,P$.

c_4	TrP (with NOC)	TrP (without NOC)
5.0002	1.40×10^{-4}	1.36×10^{-3}
5.0003	5.21×10^{-5}	1.27×10^{-3}
5.0004	1.30×10^{-4}	1.38×10^{-3}

in $100,000$ to realize the NOC performance gains. Such control parameter precision is attainable using an AWG with 17-bit vertical resolution (viz. one part in $2^{17} = 131,072$). I am not aware of such AWGs being commercially available. Thus further study of the possibility of constructing suitable custom electronics is needed to realize the NOC performance gains for this two-qubit gate. Note that 16-bit precision corresponds to a precision of one part in $2^{16} = 65,536$, and so to an uncertainty in the fifth significant digit. Thus with less than 17-bits of precision, Table 3.12 indicates that the NOC performance gains will be washed out by the uncertainty in the least significant digit of d_1. Similar for d_4 and c_4.

3.4.2 Phase/Timing Jitter

Phase jitter arises from timing errors in the clock used by an AWG to produce a desired control signal. Ideally, the clock outputs a sequence of "ticks" with constant

time separation T_{clock}, derived from an oscillation with phase $\phi(t) = 2\pi f_{clock} t$ and frequency $f_{clock} = 1/T_{clock}$. A real clock only approximates this ideal behavior. In actuality, the time T between ticks is a stochastic process $T = T_{clock} + \delta t$, where the stochastic timing error δt has: (i) vanishing time-average $\overline{\delta t} = 0$; and (ii) a standard deviation $\sigma_t = \sqrt{\overline{\delta t^2}}$ which quantifies the spread of the tick intervals about T_{clock}. The spread σ_t is known as timing jitter. The timing error δt gives rise to a phase error $\delta\phi = (2\pi f_{clock})\delta t$ which has: (i) zero time-average $\overline{\delta\phi} = 0$; and (ii) standard deviation $\sigma_\phi = \sqrt{\overline{\delta\phi^2}}$ which characterizes the spread about 2π of the phase accumulated between ticks: $\phi = 2\pi f_{clock} T$. The spread σ_ϕ is known as phase jitter. As σ_ϕ and σ_t are two ways of characterizing the clock timing errors, the ratio of spread to period for the phase $(\sigma_\phi/2\pi)$ and the time (σ_t/T_{clock}) are the same. Equating them, and solving for σ_t gives

$$\sigma_t = \frac{\sigma_\phi}{2\pi f_{clock}}. \tag{3.16}$$

This expression can be thought of as a change in units from jitter in radians (viz. σ_ϕ) to jitter in seconds (viz. σ_t).

Phase jitter is anticipated to affect the performance of the TRP gates that I used to illustrate the NOC formalism. As I discussed in Section 3.1.1 that the performance of these gates relies on quantum interference effects during a TRP sweep. In the presence of phase jitter, the TRP twist profile $\phi_4(\tau) = (\eta_4/2\lambda)\tau^4$ has phase noise $\delta\phi(\tau)$ due to the timing error $\delta\tau$ in τ. For sufficiently strong phase jitter, this phase noise will wash out the interference effects that underlie the good performance of the TRP gates. Specifically, since this noise adds to the TRP twist

phase $\phi_4(\tau) \rightarrow \phi_4'(\tau) = \phi_4(\tau) + \delta\phi(\tau)$, it causes the (dimensionless) TRP control field $\mathbf{F}_0'(\tau) = (1/\lambda)\left[\cos\phi_4'(\tau)\hat{\mathbf{x}} + \sin\phi_4'(\tau)\hat{\mathbf{y}} + \tau\hat{\mathbf{z}}\right]$ to twist incorrectly. The control field with the NOC modification is now $\mathbf{F}'(\tau) = \mathbf{F}_0'(\tau) + \Delta\mathbf{F}(\tau)$, where $\Delta\mathbf{F}(\tau)$ is the neighboring optimal control modification determined for the TRP control $\mathbf{F}_0(\tau)$ with *jitter-free* twist phase $\phi_4(\tau)$. Since the phase noise $\delta\phi(\tau)$ is unpredictable, the control modification $\Delta\mathbf{F}(\tau)$ cannot be recalculated so that it is optimal for $\mathbf{F}_0'(\tau)$. Thus, for a given target gate, one can only calculate the control modification $\Delta\mathbf{F}(\tau)$ which is optimal for the jitter-free TRP control $\mathbf{F}_0(\tau)$, and add it to the noisy TRP control $\mathbf{F}_0'(\tau)$. Since $\Delta\mathbf{F}(\tau)$ is not optimal for $\mathbf{F}'(\tau)$, the NOC performance improvements are expected to be reduced by phase jitter.

To quantitatively study the effects of phase/timing jitter on the NOC performance gains, I modelled the phase noise $\delta\phi(\tau)$ as shot noise and used the model to generate numerical realizations of the phase noise $\delta\phi(\tau)$. The details of the noise model and the protocol used to generate noise realizations is described in Appendix B. For each noise realization, I determined the state trajectory $U(\tau)$ by numerically simulating the Schrodinger dynamics generated by the noisy control field $\mathbf{F}'(\tau)$, and used it to determine the $Tr\,P$ upper bound for the gate error probability P_e. For each target gate U_{tgt} and given value of phase jitter σ_ϕ (equivalently, mean phase noise power $\overline{P}$, see below), I generated ten realizations of phase noise $\delta\phi(\tau)$, and determined the ten corresponding values of $Tr\,P$. The average $\langle Tr\,P\rangle$ and standard deviation $\sigma(Tr\,P)$ for these values was calculated and used to approximate the noise-averaged NOC gate performance: $P_e \leq \langle Tr\,P\rangle \pm \sigma(Tr\,P)$. I carried out simulations for various values of σ_ϕ, and present the results for the Hadamard

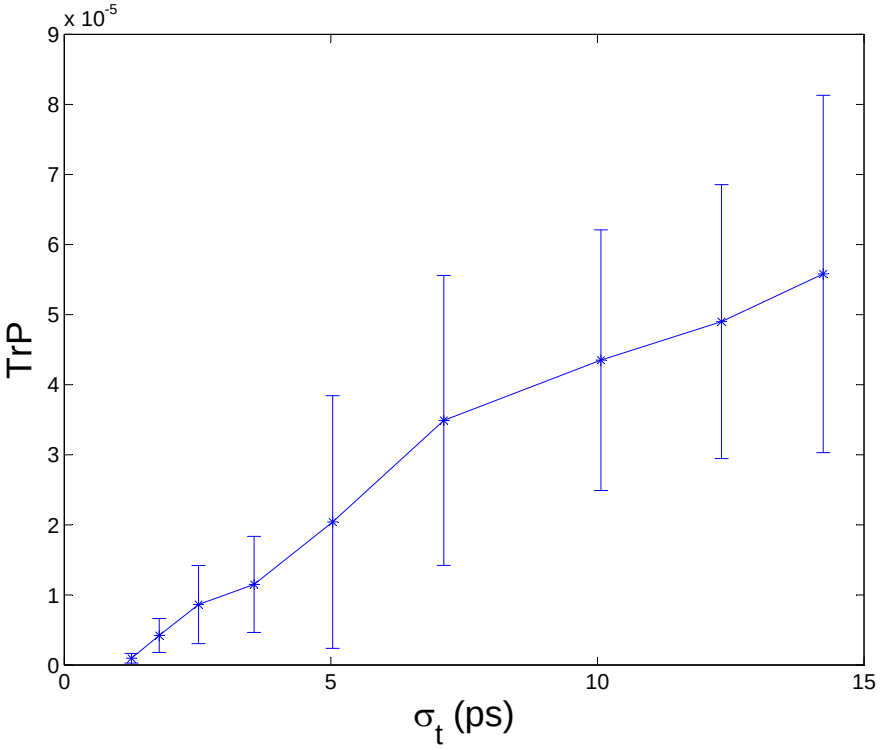

Figure 3.12: The noise-averaged value of TrP with NOC versus timing jitter $\sigma_t = \sigma_\phi/(2\pi f_{clock})$ for the Hadamard gate. For each σ_t, ten realizations of phase noise were generated, and for each realization, gate performance was determined by numerical simulation of the Schrodinger dynamics generated by the control field $\mathbf{F}'(\tau)$ that includes the noisy TRP nominal control $\mathbf{F}'_0(\tau)$ and the NOC modification $\Delta\mathbf{F}(\tau)$ (see text). The average and standard deviation were determined for the resulting ten $Tr\,P$ values. For each value of σ_t, the average of $Tr\,P$ is plotted, and the standard deviation is used to specify the error bar. To obtain σ_t, I have assumed that $f_{clock} = 1$GHz (see text).

gate in Figure 3.12.

To put Figure 3.12 into context, I note that AWGs with timing jitter $\sigma_t = 5$ps and clock frequency $f_{clock} = 1$GHz are commercially available [53]. In Appendix B I show that the phase noise variance $\overline{\delta\phi^2}$ is equal to the mean phase noise power $\overline{P}$. Since $\sigma_\phi = \sqrt{\overline{\delta\phi^2}}$, it turns out that $\sigma_\phi = \sqrt{\overline{P}}$, and so phase jitter is simply an alternative way to represent phase noise power. Eq. (3.16) is then used to convert

phase jitter σ_ϕ into timing jitter σ_t. The horizontal axis in Figure 3.12 is thus simply an encoding of phase noise power. The largest phase noise power value used in the simulations was $\overline{P} = 0.008$, which gives

$$\sigma_t = \frac{\sqrt{0.008}}{2\pi(10^9\,\mathrm{s}^{-1})} = 14.2\mathrm{ps}. \tag{3.17}$$

This corresponds to the right-most data-point in Figure 3.12. A similar conversion of phase noise power was done for the other simulation data-points. At $\sigma_t = 5.03$ps, appropriate for commercially available AWGs, Figure 3.12 indicates that $P_e \leq (2.04 \pm 1.80) \times 10^{-5}$. It is shown in Table 3.2 that, for ideal control, NOC produced a Hadamard gate with $P_e \leq 1.04 \times 10^{-8}$. As anticipated, the NOC performance gains are impacted by phase jitter. Figure 3.12 also shows that if an AWG was available with $\sigma_t = 1.26$ps, then $P_e \leq (9.59 \pm 6.94) \times 10^{-7}$, which is: (i) an order of magnitude reduction in the impact of phase jitter compared to $\sigma_t = 5.03$ps; and (ii) *two orders-of-magnitude* less than the target accuracy threshold of 10^{-4}, underscoring the importance of reducing timing jitter in the control electronics. I discuss this further below.

In Table 3.15 I display the impact of phase/timing jitter on the NOC performance gains of all gates in $\mathcal{G}_U$ for timing jitter $\sigma_t = 5.03$ps. It is shown that, even with timing jitter at the level found in commercially available AWGs, all gates in $\mathcal{G}_U$ have gate error probabilities that are an *order of magnitude smaller* than the target accuracy threshold value of 10^{-4}. Notice also the insensitivity of the two-qubit TRP gate to 5.03ps timing jitter. The standard deviation for this gate, $\sigma(TrP) = 5.26 \times 10^{-11}$, is displayed as zero to three significant figures in Table

Table 3.15: Sensitivity of TrP to timing jitter $\sigma_t = \sqrt{\bar{P}}/(2\pi f_{clock})$ for all target gates in the universal set $\mathcal{G}_U$. For all gates, the numerical simulations used mean noise power $\bar{P} = 0.001$, which corresponds to timing jitter $\sigma_t = 5.03$ps for $f_{clock} = 1$GHz. For each gate, ten phase noise realizations were generated (see Appendix B), leading to ten values of the $Tr\,P$ upper bound on the gate error probability $P_e \leq Tr\,P$. The third column lists, for each gate, the corresponding average $< TrP >$, and uses the standard deviation $\sigma(TrP)$ to indicate the spread of $Tr\,P$ about the average.

Gate	Timing-jitter σ_t	$P_e \leq\ < TrP > \pm\sigma$(TrP) with NOC
Hadamard	$5.03ps$	$(2.04 \pm 1.80) \times 10^{-5}$
NOT	$5.03ps$	$(2.11 \pm 1.64) \times 10^{-5}$
Modified $\pi/8$	$5.03ps$	$(2.92 \pm 1.96) \times 10^{-5}$
Modified phase	$5.03ps$	$(3.04 \pm 2.16) \times 10^{-5}$
Modified controlled phase	$5.03ps$	$(5.21 \pm 0.00) \times 10^{-5}$

3.15. This weak sensitivity to timing jitter is not completely surprising given the weak sensitivity of this gate to imprecision in λ and η_4 that was found in Ref. [42], and thus to imprecision in the twisting of the control field. The critical parameters for this gate are d_1, d_4, and c_4 (see Section 3.4.1).

In Table 3.16 I display the impact of phase/timing jitter on the NOC performance gains of all gates in $\mathcal{G}_U$ for timing jitter $\sigma_t = 1.26$ps. It is shown that the gate error probability for the one-qubit gates is reduced by an order-of-magnitude ($P_e \sim 10^{-5} \rightarrow 10^{-6}$) compared to the error probability at $\sigma_t = 5.03$ps. The two-qubit gate error probability is unchanged at $P_e = 5.21 \times 10^{-5}$, although its standard deviation is now $\sigma(TrP) = 4.24 \times 10^{-14}$. Thus reducing timing jitter by a factor of 5

Table 3.16: Sensitivity of TrP to timing jitter $\sigma_t = \sqrt{\overline{P}}/(2\pi f_{clock})$ for all target gates in the universal set $\mathcal{G}_U$. For all gates, the numerical simulations used mean noise power $\bar{P} = 6.25 \times 10^{-5}$, which corresponds to timing jitter $\sigma_t = 1.26$ps for $f_{clock} = 1$GHz. For each gate, ten phase noise realizations were generated (see Appendix B), leading to ten values of the $Tr\,P$ upper bound on the gate error probability $P_e \leq Tr\,P$. The third column lists, for each gate, the corresponding average $< TrP >$, and uses the standard deviation $\sigma(TrP)$ to indicate the spread of $Tr\,P$ about the average.

Gate	Timing-jitter σ_t	$P_e \leq \; < TrP > \pm\sigma$(TrP) with NOC
Hadamard	$1.26ps$	$(9.59 \pm 6.94) \times 10^{-7}$
Modified $\pi/8$	$1.26ps$	$(1.24 \pm 1.04) \times 10^{-6}$
NOT	$1.26ps$	$(1.82 \pm 1.14) \times 10^{-6}$
Modified phase	$1.26ps$	$(1.92 \pm 1.57) \times 10^{-6}$
Modified controlled phase	$1.26ps$	$(5.21 \pm 0.00) \times 10^{-5}$

produces one-qubit gates whose error probability is *two orders-of-magnitude* smaller than the target accuracy threshold of 10^{-4}. For a threshold $P_a \sim 10^{-3}$ appropriate for surface and color quantum error correcting codes, *all gates* in $\mathcal{G}_U$ operate 2–3 *orders-of-magnitude* below threshold at $\sigma_t = 1.26$ps. Thus, for AWGs operating at this reduced level of timing jitter, the impact of phase/timing jitter on the NOC performance gains is greatly mitigated.

In Table 3.17 I present further noisy simulation results for all gates in $\mathcal{G}_U$ at noise power $\overline{P} = 0.005$ (0.008) for the two-qubit (one-qubit) gate(s). This corresponds, respectively, to: (i) timing jitter $\sigma_t = 11.3$ (14.2)ps; (ii) $\overline{n} = 2.50$ (1.33); and

Table 3.17: Sensitivity of TrP to timing jitter $\sigma_t = \sqrt{\overline{P}}/(2\pi f_{clock})$ for all target gates in the universal set $\mathcal{G}_U$. For all one-qubit (two-qubit) gates, the numerical simulations used mean noise power $\bar{P} = 0.008$ (0.005), which corresponds to timing jitter $\sigma_t = 14.2$ (11.3)ps for $f_{clock} = 1$GHz. For each gate, ten phase noise realizations were generated (see Appendix B), leading to ten values of the $Tr\,P$ upper bound on the gate error probability $P_e \leq Tr\,P$. The third column lists, for each gate, the corresponding average $< TrP >$, and uses the standard deviation $\sigma(TrP)$ to indicate the spread of $Tr\,P$ about the average.

Gate	Timing-jitter σ_t	$P_e \leq \; < TrP > \pm\sigma$(TrP) with NOC
Hadamard	$14.2ps$	$(5.58 \pm 2.55) \times 10^{-5}$
NOT	$14.2ps$	$(5.71 \pm 2.67) \times 10^{-5}$
Modified phase	$14.2ps$	$(7.09 \pm 3.23) \times 10^{-5}$
Modified $\pi/8$	$14.2ps$	$(8.04 \pm 2.43) \times 10^{-5}$
Modified controlled phase	$11.3ps$	$(6.74 \pm 1.09) \times 10^{-5}$

(iii) phase noise realizations with, on average, $\mathcal{N}_f = 300$ (213) noise fluctuations. It is shown that the increased noise power $\overline{P} = 0.001 \rightarrow 0.005, 0.008$ only degraded the NOC performance gains slightly more than was seen in Table 3.15. Notice that, even with phase jitter that is worse than occurs in commercially available AWGs, all gates in $\mathcal{G}_U$ still have error probabilities that fall below the target accuracy threshold of 10^{-4}.

Lastly, note that for starting gates whose good performance is not due to quantum interference, phase jitter may have less impact on the NOC performance gains than for the TRP gates examined here.

Chapter 4: Application of NOC to Quantum State Preparation: Two-qubit Logical Bell State

Having introduced the general theory of neighboring optimal control in Chapter 2, and illustrated its use by applying the general method to improve the performance of all gates in a universal set of quantum gates $\mathcal{G}_U$ produced using twisted-rapid passage in Chapter 3, in this Chapter I adapt the general NOC method to fault-tolerant logical quantum state preparation.

A fundamental task which a quantum computer must execute with success probability close to 1 is the fault-tolerant preparation of a known logical quantum state. Such states are required throughout a quantum computation includes, for example, in Steane error correction [54], syndrome extraction requires ancilla qubits prepared in the $|\overline{0}\rangle$ and $|\overline{+}\rangle$ eigenstates of the logical Pauli $\overline{Z}$ and $\overline{X}$ operators, respectively. In quantum teleportation (QT) [15] based schemes of fault-tolerant quantum computing (FTQC) [55–58], fault-tolerant preparation of logical Bell states are an important prerequisite.

This Chapter presents a two-step procedure for fault-tolerant preparation of a logical qubit state $|\overline{\psi}_{tgt}\rangle$. Step 1 begins with a single-shot preparation for a high-fidelity approximation $|\psi_a\rangle$ to a target state $|\psi_{tgt}\rangle$ by adapting the general NOC

method presented in Chapter 2, with preparation error probability ϵ; the high-fidelity approximate state $|\psi_a\rangle$ then goes through a projection circuit, leaving it in $|\psi'_a\rangle$ state which has preparation error probability $\mathcal{O}(\epsilon^2)$. Step 2 then takes a block of p pairs of physical qubits, each prepared in $|\psi'_a\rangle$ using Step 1, and runs the block through a simple fault-tolerant circuit which leaves it in the logical state $|\overline{\psi}_{tgt}\rangle$. I illustrate this procedure by preparing the following two-qubit logical Bell state

$$|\overline{\beta_{01}}\rangle = \frac{1}{\sqrt{2}}\left[|\overline{01}\rangle + |\overline{10}\rangle\right]. \tag{4.1}$$

This Chapter is structured as follows. Section 4.1 briefly reviews some background knowledge about Bell state and quantum teleportation. Sections 2 and 3 describe Steps 1 and 2 of the logical state preparation procedure, respectively. Section 2 describes a single-shot NOC approach to prepare a high-fidelity approximation to the physical two-qubit Bell state $|\beta_{01}\rangle$. Both ideal control and non-ideal control are examined. It is shown that the single-shot NOC approach is able to achieve a preparation error probability of $\epsilon \sim 10^{-6}$ for ideal control, and that a preparation error probability of $\epsilon \sim 10^{-5}$ should be possible with commercially available arbitrary waveform generators (AWG). Passing the NOC produced state through a projection circuit yields an approximate Bell state with error probability $\mathcal{O}(\epsilon^2)$. Section 3 introduces a simple fault-tolerant circuit which produces the logical Bell state $|\overline{\beta_{01}}\rangle$, and I illustrate its use for the $[4, 2, 2]$ quantum error detecting code C_4.

4.1 Bell State, Quantum Teleportation and Fault-tolerant Quantum Computation

The *Bell states* $|\beta_{xy}\rangle$, $x, y = 0, 1$ are four maximally entangled two-qubit states [59], which form an orthonormal basis for the two-qubit Hilbert space, known as the Bell basis:

$$\begin{aligned} |\beta_{00}\rangle &= \frac{|00\rangle + |11\rangle}{\sqrt{2}}; \qquad |\beta_{10}\rangle = \frac{|00\rangle - |11\rangle}{\sqrt{2}} \\ |\beta_{01}\rangle &= \frac{|01\rangle + |10\rangle}{\sqrt{2}}; \qquad |\beta_{11}\rangle = \frac{|01\rangle - |10\rangle}{\sqrt{2}} \ . \end{aligned} \tag{4.2}$$

where the state $|ij\rangle$, $i, j = 0, 1$ are the computational basis states of the two-qubit Hilbert space, which are usually chosen to be the eigenstates of the two-qubit Pauli operators $Z^1 = \sigma_z \otimes I$ and $Z^2 = I \otimes \sigma_z$, where I is the 2×2 identity operator.

Here "maximally entangled" [60] means that tracing over the second qubit to find the density operator ρ_1 for the first qubit results in a multiple of the identity operator I

$$\rho_1 = tr_2 \left(|\beta_{xy}\rangle \langle \beta_{xy}| \right) = \frac{1}{2} I. \tag{4.3}$$

Similarly, $\rho_2 = \frac{1}{2} I$. This indicates that if a two-qubit system is in a Bell state $|\beta_{xy}\rangle$, the von Neumann entropy [61] for the whole system is apparently zero; however, for the two single-qubit subsystems, their von Neumann entropies take the maximal value of 1

$$S(\rho_1) = S(\rho_2) = -tr \left(\frac{I}{2} \log_2 \frac{I}{2} \right) = 1. \tag{4.4}$$

In other words, even though the whole system is in a pure state, the two single-qubit subsystems are in completely mixed state. One can use a two-qubit system

in a Bell state to encode two bits of information, say, the parity of the state, and the relative phase between the two computational basis states. This information cannot be acquired by a local measurement on a single-qubit subsystem, which would merely generate a random bit of 0 or 1. On the other hand, a local operation on any single-qubit subsystem does manipulate the state of the whole system, even if the two qubits are spatially separated.

Take the Bell state $|\beta_{01}\rangle$ as an example: upon measuring the first qubit in the computational basis, one ends up with two possible outcomes, each with probability 1/2: (i) obtaining measuring result 0 and leaving the post-measurement state in $|01\rangle$, and (2) obtaining measuring result 1 and leaving the post-measuring state in $|10\rangle$. A subsequent measuring on the second qubit would always give the opposite measuring result as the measurement of the first qubit. Similar measurement correlation exists for all other Bell states. It is this entanglement property that makes the Bell states the essential resource in quantum teleportation (QT) [15], by which quantum state can be transmitted between two parties, Alice and Bob, even in the absence of a quantum communications channel linking the two.

Here I present the protocol for Alice to deliver a qubit in the state $|\psi\rangle = \alpha\,|0\rangle + \beta\,|1\rangle$ to Bob, where α and β are unknown amplitudes, given they each possess one qubit of the Bell state $|\beta_{01}\rangle$. The quantum circuit for teleporting $|\psi\rangle$ is shown in Figure 4.1.

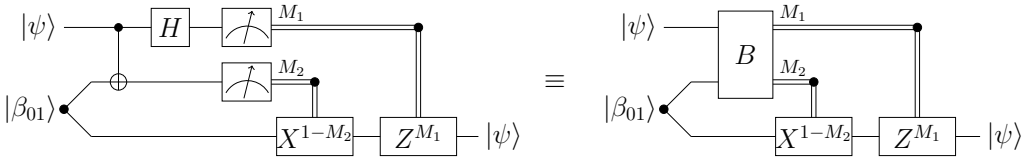

Figure 4.1: Quantum circuit for teleporting a qubit state $|\psi\rangle$ using the Bell state $|\beta_{01}\rangle$. The meter represents measurement in the computational basis.

The input state to the circuit in Figure 4.1 is

$$\begin{aligned} |\psi_0\rangle &= |\psi\rangle \otimes |\beta_{01}\rangle \\ &= \frac{1}{\sqrt{2}} \left[\alpha |0\rangle \otimes (|01\rangle + |10\rangle) + \beta |1\rangle \otimes (|01\rangle + |10\rangle)\right]. \end{aligned} \tag{4.5}$$

Alices then applies a CNOT gate to her qubits, obtaining

$$|\psi_1\rangle = \frac{1}{\sqrt{2}} \left[\alpha |0\rangle \otimes (|01\rangle + |10\rangle) + \beta |1\rangle \otimes (|11\rangle + |00\rangle)\right]. \tag{4.6}$$

Next Alices applies a Hadamard gate to the first qubit, obtaining

$$\begin{aligned} |\psi_2\rangle &= \frac{1}{2} \left[\alpha(|0\rangle + |1\rangle) \otimes (|01\rangle + |10\rangle) + \beta(|0\rangle - |1\rangle) \otimes (|11\rangle + |00\rangle)\right] \\ &= \frac{1}{2} \left[|00\rangle \otimes (\alpha |1\rangle + \beta |0\rangle) + |01\rangle \otimes (\alpha |0\rangle + \beta |1\rangle)\right. \\ &\quad \left. + |10\rangle \otimes (\alpha |1\rangle - \beta |0\rangle) + |11\rangle \otimes (\alpha |0\rangle - \beta |1\rangle)\right]. \end{aligned} \tag{4.7}$$

Alice then performs a $Z-$ measurement on her qubits and sends Bob her results through a classical channel. Depending on Alice's measurement outcome M_1 and M_2, Bob then applies the corresponding operation $X^{1-M_2} Z^{M_1}$ to his postmeasurement qubit and recovers $|\psi\rangle$.

Quantum teleportation has been used as a key ingredient for some schemes of fault-tolerant quantum computation (FTQC) [55–58]. By utilizing quantum error detection codes, post-selected quantum computation [58] achieves an accuracy

threshold $\gamma \sim 10^{-3}$ [62,63]. Fault-tolerant preparation of a logical Bell state is thus an important prerequisite for QT based schemes for FTQC. In the following sections, I present a two-step procedure for fault-tolerant preparation of a two logical qubit state $|\overline{\psi}_{tgt}\rangle$, and use this procedure to prepare the logical Bell state $|\overline{\beta_{01}}\rangle$.

4.2 Step 1: High-fidelity physical Bell state $|\beta_{01}\rangle$ preparation

In this section I introduce the first step of our two-step procedure for logical quantum state preparation, which combines single-shot NOC state preparation with a projection circuit, to prepare a high-fidelity approximation to the Bell state $|\beta_{01}\rangle$. In Section 4.2.1 I re-state the control problem to produce a high-fidelity approximation to a target physical quantum state as to find a control field which enacts a high-fidelity approximated target gate, thus making the NOC approach introduced in Chapter 2 adaptable. In Section 4.2.2 I present the input to the NOC approach: a good approximation to the Bell state $|\beta_{01}\rangle$ produced using twisted-rapid passage. In Section 4.2.3 I use the NOC approach to determine a control modification which yields a better approximated Bell state $|\beta_{01}\rangle$. Numerical results are presented in Section 4.2.4 for ideal control and in Section 4.2.5 for non-ideal control. And finally, in Section 4.2.6 I use a projection circuit which takes as input the state prepared by NOC with error probability $\mathcal{O}(\epsilon)$, and returns an approximate Bell state $|\beta_{01}{}'\rangle$ with error probability $\mathcal{O}(\epsilon^2)$.

4.2.1 Reformulating the Control Problem

The first task of the two-step logical quantum state preparation is to find a control field $\mathbf{F}(t)$ which produces a state $|\psi_a\rangle$ which is a high-fidelity approximation to a target state $|\psi_{tgt}\rangle$. These states can be multi-(physical) qubit states, though for purposes of this Chapter I focus on preparation of two-qubit states. As indicated above, these high-fidelity states are then used to prepare the logical target state $|\overline{\psi}_{tgt}\rangle$. In this Section, I re-state this control problem to a familiar form, such that the NOC approach introduced in Chapter 2 to improve quantum gate performance becomes applicable.

Consider a two-qubit system in the state $|\psi(t)\rangle$. The qubits are coupled to a control field $\mathbf{F}(t)$ with Hamiltonian

$$\mathcal{H}_2(t) = \mathcal{H}_2\left[\mathbf{F}(t)\right], \tag{4.8}$$

which is a functional of $\mathbf{F}(t)$ which acts for a time $-T/2 \leq t \leq T/2$. Throughout this thesis I assume the control duration time T is much shorter than the qubit longitudinal (T_1) and transverse (T_2) relaxation times so that the qubit is weakly decohering and a state vector description is appropriate.

At $t = -T/2$ the two-qubit state is initialized such that $|\psi(-T/2)\rangle = |00\rangle$. The control field $\mathbf{F}(t)$ then drives a unitary transformation $U(t)$ on the state, taking it to the final state $|\psi_a\rangle$:

$$|\psi_a\rangle = U_f\,|00\rangle\,, \tag{4.9}$$

where $U_f \equiv U(T/2)$.

Let $\left|\psi^{\perp}_{tgt,2}\right\rangle$, $\left|\psi^{\perp}_{tgt,3}\right\rangle$, $\left|\psi^{\perp}_{tgt,4}\right\rangle$ be three mutually orthogonal states that are orthogonal to $|\psi_{tgt}\rangle$, and U_{tgt} be a 4×4 unitary matrix, whose columns are $|\psi_{tgt}\rangle$, $\left|\psi^{\perp}_{tgt,2}\right\rangle$, $\left|\psi^{\perp}_{tgt,3}\right\rangle$ and $\left|\psi^{\perp}_{tgt,4}\right\rangle$, respectively:

$$U_{tgt} = \begin{pmatrix} | & | & | & | \\ |\psi_{tgt}\rangle & \left|\psi^{\perp}_{tgt,2}\right\rangle & \left|\psi^{\perp}_{tgt,3}\right\rangle & \left|\psi^{\perp}_{tgt,4}\right\rangle \\ | & | & | & | \end{pmatrix}.$$

By construction, U_{tgt} maps $|00\rangle$ to $|\psi_{tgt}\rangle$ exactly, *i.e.*

$$|\psi_{tgt}\rangle \equiv U_{tgt}\,|00\rangle\,.$$

I now re-state the control problem to produce a high-fidelity approximation to a target quantum state: find a control field $\mathbf{F}(t)$ which enacts a unitary transformation U_f that is a high-fidelity approximation to the target unitary 4×4 matrix U_{tgt}, which can be seen as a two-qubit gate. Once such an $\mathbf{F}(t)$ is determined, the state $|\psi_a\rangle$ produced by $\mathbf{F}(t)$ would naturally be a high-fidelity approximation to the target state $|\psi_{tgt}\rangle$, as the fidelity of $|\psi_a\rangle$

$$\begin{aligned} \mathcal{F}_a &\equiv |\langle\psi_a|\,\psi_{tgt}\rangle| \\ &= \left|\langle 00|\,U_f^{\dagger} U_{tgt}\,|00\rangle\right| \rightarrow 1. \end{aligned} \tag{4.10}$$

A solution to this control problem has been presented in Chapter 2 using NOC. Specifically, the Strategy 2 introduced in Section 2.5.2 is particularly suitable for solving this control problem. In the following sections I will apply this approach to determine a control field that produces a high-fidelity approximated physical Bell state $|{\beta_{01}}^{a}\rangle$.

4.2.2 Input: Good State Prepared via TRP

After re-stating the control problem in Section 4.2.1 I now apply the general NOC method introduced in Chapter 2 to determine a control field that produces a high-fidelity approximation to the target, the Bell state $|\beta_{01}\rangle$. The general NOC method did not assume a specific form of the control Hamiltonian. For the following derivation and simulation, I assume that the Hamiltonian $\mathcal{H}_2$ contains a Zeeman interaction term that couples each qubit to the control field $\mathbf{F}(t)$, and an anisotropic Heisenberg interaction coupling the two qubits. Note that alternative two-qubit interactions can easily be considered by straightforward modification of the following arguments.

With these assumptions, the Hamiltonian in the lab frame can be written as

$$\begin{aligned}\frac{\mathcal{H}_2[\mathbf{F}(t)]}{\hbar} &= -\sum_{i=1}^{2}\frac{\gamma_i}{2}\boldsymbol{\sigma}^i\cdot\mathbf{F}(t) - \frac{\pi}{2}\left(J_z\sigma_z^1\sigma_z^2 + J_{xy}(\sigma_x^1\sigma_x^2+\sigma_y^1\sigma_y^2)\right)\\ &= \frac{{\mathcal{H}_2}^0(t)}{\hbar} + \sum_{j=1}^{3}\mathcal{G}_j(t)\Delta F_j(t),\end{aligned} \tag{4.11}$$

where

$$\frac{{\mathcal{H}_2}^0(t)}{\hbar} = -\sum_{i=1}^{2}\frac{\gamma_i}{2}\boldsymbol{\sigma}^i\cdot\mathbf{F}_0(t) - \frac{\pi}{2}\left(J_z\sigma_z^1\sigma_z^2 + J_{xy}(\sigma_x^1\sigma_x^2+\sigma_y^1\sigma_y^2)\right) \tag{4.12}$$

is the nominal Hamiltonian which excludes the contribution from the control modification $\Delta\mathbf{F}(t)$, in which γ_i, $i=1,2$ is the gyromagnetic ratio of the Zeeman coupling for qubit i, and $J_{z,xy}$ are the Heisenberg interaction coupling constant; and

$$\mathcal{G}_j(t) = -\frac{1}{2}\sum_{i=1}^{2}\gamma_i\sigma_j^i. \tag{4.13}$$

The input for the NOC procedure is a known control $\mathbf{F}_0(t)$ which enacts a unitary transformation $U_0(t)$, which maps the initial state $|\psi_0(-T/2)\rangle = |00\rangle$ to $\left|\beta_{01}{}^0\right\rangle$

$$|00\rangle \rightarrow \left|\beta_{01}{}^0\right\rangle \equiv |\psi_0(T/2)\rangle = U_{0,f}\,|00\rangle\,. \tag{4.14}$$

Here $U_{0,f} = U_0(T/2)$, and $\left|\beta_{01}{}^0\right\rangle$ is a good approximation to the target state $|\beta_{01}\rangle$. I use a form of non-adiabatic rapid passage known as twisted rapid passage (TRP) [38, 39] as the nominal control $\mathbf{F}_0(t)$ to produce the good state $\left|\beta_{01}{}^0\right\rangle$. In the lab frame, $\mathbf{F}_0(t)$ has a static component B_0 along the z-axis with a simultaneous twisting in the $x-y$ plane. I can write

$$\mathbf{F}_0(t) = B_0\hat{\mathbf{z}} + B_{rf}\cos\phi_{rf}(t)\hat{\mathbf{x}} - B_{rf}\sin\phi_{rf}(t)\hat{\mathbf{y}}. \tag{4.15}$$

Introducing $\omega_i = \gamma_i B_0$ and $\omega_i^{rf} = \gamma_i B_{rf}$, $i = 1, 2$, and inserting Eq. (4.15) into Eq. (4.12) yields

$$\begin{aligned}\frac{\mathcal{H}_2{}^0(t)}{\hbar} = &-\frac{\omega_1}{2}\sigma_z^1 - \frac{\omega_1^{rf}}{2}\left[\cos\phi_{rf}\sigma_x^1 - \sin\phi_{rf}\sigma_y^1\right] \\ &-\frac{\omega_2}{2}\sigma_z^2 - \frac{\omega_2^{rf}}{2}\left[\cos\phi_{rf}\sigma_x^2 - \sin\phi_{rf}\sigma_y^2\right] \\ &-\frac{\pi}{2}\left(J_z\sigma_z^1\sigma_z^2 + J_{xy}(\sigma_x^1\sigma_x^2 + \sigma_y^1\sigma_y^2)\right).\end{aligned} \tag{4.16}$$

I next introduce a unitary transformation that puts the system in the detector frame [39],

$$U_{ld}(t) = \exp\left[\frac{i}{2}\phi_{det}(t)(\sigma_z^1 + \sigma_z^2)\right]. \tag{4.17}$$

The Hamiltonian in the detector frame is then

$$\begin{aligned}\frac{\mathcal{H}_{2,d}{}^{0}(t)}{\hbar} &= U_{ld}^{\dagger}\frac{\mathcal{H}_{2}{}^{0}(t)}{\hbar}U_{ld} - iU_{ld}^{\dagger}\frac{dU_{ld}}{dt} \\ &= \left(\frac{-\omega_1 + \dot{\phi}_{det}}{2}\right)\sigma_z^1 + \left(\frac{-\omega_2 + \dot{\phi}_{det}}{2}\right)\sigma_z^2 \\ &\quad - \frac{\omega_1^{rf}}{2}\left[\cos\left(\phi_{det} - \phi_{rf}\right)\sigma_x^1 + \sin\left(\phi_{det} - \phi_{rf}\right)\sigma_y^1\right] \\ &\quad - \frac{\omega_2^{rf}}{2}\left[\cos\left(\phi_{det} - \phi_{rf}\right)\sigma_x^2 + \sin\left(\phi_{det} - \phi_{rf}\right)\sigma_y^2\right] \\ &\quad - \frac{\pi}{2}J_z\sigma_z^1\sigma_z^2 - \frac{\pi}{2}J_{xy}\left[\sigma_x^1\sigma_x^2 + \sigma_y^1\sigma_y^2\right].\end{aligned} \tag{4.18}$$

To produce a TRP sweep in the detector frame it is necessary to sweep $\dot{\phi}_{det}$ and $\dot{\phi}_{rf}$ through a Larmor resonance frequency. I chose to sweep through the Larmor frequency ω_2 and put the 1st qubit out of resonance by introducing the detuning Δ:

$$\begin{aligned}\dot{\phi}_{det} &= \omega_2 + \frac{2at}{\hbar} + \Delta \\ \phi_{rf} &= \phi_{det} - \phi_{trp}.\end{aligned} \tag{4.19}$$

Here a is the TRP inversion rate, and $\phi_{trp}(t) = (1/2)Bt^4$ is the TRP quartic twist. Introducing $\delta\omega = \omega_1 - \omega_2$ yields

$$\begin{aligned}\frac{\mathcal{H}_{2,d}{}^{0}(t)}{\hbar} &= \left(-\frac{\delta\omega + \Delta}{2} + \frac{at}{\hbar}\right)\sigma_z^1 + \left(-\frac{\Delta}{2} + \frac{at}{\hbar}\right)\sigma_z^2 \\ &\quad - \frac{\omega_1^{rf}}{2}\left[\cos\phi_{trp}\sigma_x^1 + \sin\phi_{trp}\sigma_y^1\right] \\ &\quad - \frac{\omega_2^{rf}}{2}\left[\cos\phi_{trp}\sigma_x^2 + \sin\phi_{trp}\sigma_y^2\right] \\ &\quad - \frac{\pi J_z}{2}\sigma_z^1\sigma_z^2 - \frac{\pi J_{xy}}{2}\left[\sigma_x^1\sigma_x^2 + \sigma_y^1\sigma_y^2\right].\end{aligned} \tag{4.20}$$

It proves useful for the numerical simulations to recast the Schrodinger equation into dimensionless form. Let $b_{1,2} = \hbar\omega_{1,2}^{rf}/2$ and $\lambda = \hbar a/b_2^2$. Introduce the dimensionless time $\tau = (a/b_2)t$. The TRP quartic twist expressed in dimensionless time is then $\phi_4(\tau) = (\eta_4/2\lambda)\tau^4$, where $\eta_4 = \hbar B b_2^2/a^3$. Multiplying both sides of

Eq. (4.20) by (b_2/a) finally yields the Hamiltonian in dimensionless form, which reads

$$\begin{aligned}\overline{\mathcal{H}}^0_{2,d}(\tau) = &\left(-\frac{d_1+d_2}{2}+\frac{\tau}{\lambda}\right)\sigma_z^1+\left(-\frac{d_2}{2}+\frac{\tau}{\lambda}\right)\sigma_z^2\\ &-\frac{d_3}{\lambda}\left[\cos\phi_{trp}\sigma_x^1+\sin\phi_{trp}\sigma_y^1\right]\\ &-\frac{1}{\lambda}\left[\cos\phi_{trp}\sigma_x^2+\sin\phi_{trp}\sigma_y^2\right]\\ &-\frac{\pi}{2}\left[d_z\sigma_z^1\sigma_z^2+d_{xy}(\sigma_x^1\sigma_x^2+\sigma_y^1\sigma_y^2)\right],\end{aligned} \tag{4.21}$$

where $d_1 = (b_2/a)\delta\omega$, $d_2 = (b_2/a)\Delta$, $d_3 = b_1/b_2$ and $d_{z,xy} = (b_2/a)J_{z,xy}$. The Hamiltonian $\overline{\mathcal{H}}^0_{2,d}(\tau)$ depends on the TRP sweep parameters (λ, η_4) as well as the dimensionless coupling parameters (d_1, d_2, d_3) and $d_{z,xy}$. Here $(d_1, d_2, d_3, d_{z,xy})$ are the dimensionless versions of, respectively, the Larmor frequency difference $\delta\omega = \omega_1 - \omega_2$, the detuning parameter Δ, the Zeeman coupling ratio $b_1/b_2 = \gamma_1/\gamma_2$, and the Heisenberg coupling strength $J_{z,xy}$.

Equation (4.21) presents the dimensionless nominal Hamiltonian $\overline{\mathcal{H}}^0_{2,d}(\tau)$, which can be then integrated via the Schrodinger Equation to obtain $U_{0,f} = U_0(\tau_0/2)$ which maps the initial state $|00\rangle$ to the state $\left|\beta_{01}{}^0\right\rangle$. Note that $\overline{\mathcal{H}}^0_{2,d}(\tau)$ and $U_0(\tau)$ are functions of the dimensionless control parameters $\mathbf{p} = (\eta_4, \lambda, d_1, d_2, d_3, d_z, d_{xy})$, and hence $\left|\beta_{01}{}^0\right\rangle$ is a function of the control parameters $\mathbf{p}$, as well as the dimensionless inversion time $\tau_0 = (a/b_2)T$. To produce a good approximate state $\left|\beta_{01}{}^0\right\rangle$ requires finding suitable values for these parameters. As with the two-qubit simulation in Chapter 3 I set $\tau_0 = 120$ in all the numerical simulations presented below, and use simulated annealing [64] to find a parameter assignment $\overline{\mathbf{p}} = \left(\overline{\eta}_4, \overline{\lambda}, \overline{d}_1, \overline{d}_2, \overline{d}_3, \overline{d}_z, \overline{d}_{xy}\right)$ that

minimizes the state error probability [65]

$$\epsilon_0(\overline{\mathbf{p}}) = 1 - \left|\left\langle {\beta_{01}}^0 \right| \beta_{01}\right\rangle\right|^2 . \tag{4.22}$$

which is equivalent to maximizing the state fidelity as

$$\mathcal{F}_0(\overline{\mathbf{p}}) = \left|\left\langle {\beta_{01}}^0 \right| \beta_{01}\right\rangle\right| = \sqrt{1-\epsilon_0(\overline{\mathbf{p}})}. \tag{4.23}$$

I list the control parameter values I found in Table. 4.1. Numerical integration of the two-qubit Schrodinger equation using the TRP control Hamiltonian $\overline{\mathcal{H}}^0_{2,d}(\tau)$ with these parameter values produces the state

$$\left|{\beta_{01}}^0\right\rangle = \begin{pmatrix} -0.0070 - 0.0066\,i \\ -0.2053 - 0.6870\,i \\ -0.2006 - 0.6672\,i \\ 0.0080 + 0.0164\,i \end{pmatrix}. \tag{4.24}$$

The error probability for the state $\left|{\beta_{01}}^0\right\rangle$ is

$$\epsilon_0(\overline{\mathbf{p}}) = 1 - \left|\left\langle {\beta_{01}}^0 \right| \beta_{01}\right\rangle\right|^2 = 6.68 \times 10^{-4}, \tag{4.25}$$

and its fidelity

$$\mathcal{F}_0(\overline{\mathbf{p}}) = \sqrt{1-\epsilon_0(\overline{\mathbf{p}})} = 0.9997. \tag{4.26}$$

The state $\left|{\beta_{01}}^0\right\rangle$ produced by the TRP control carries two components: a leading component along the target Bell state $|\beta_{01}\rangle$, and a small error component of order $\mathcal{O}(\sqrt{\epsilon_0(\overline{\mathbf{p}})})$ along the other Bell states. Therefore, the state $\left|{\beta_{01}}^0\right\rangle$ is a good

Table 4.1: The target state studied in this paper is the Bell state $|\beta_{01}\rangle$. The TRP control parameter values listed for $\overline{\mathbf{p}} = \left(\overline{\eta}_4, \overline{\lambda}, \overline{d}_1, \overline{d}_2, \overline{d}_3, \overline{d}_z, \overline{d}_{xy}\right)$ were found using simulated annealing, with the dimensionless control operation time $\tau_0 = 120$. The state error probability was found by numerically integrating the two-qubit Schrodinger equation and using Eq. (4.22).

$\overline{\eta}_4$	$\overline{\lambda}$	$\overline{d}_1$	$\overline{d}_2$	$\overline{d}_3$	$\overline{d}_z$	$\overline{d}_{xy}$
4.526×10^{-4}	9.579	1.386	9.622	8.905	0.918	4.331

starting point for the NOC formalism. Hence I write

$$\begin{aligned} \left|\beta_{01}{}^{0}\right\rangle &= U_{0,f}\,|00\rangle \\ &= -e^{1.28i}\sqrt{1-\epsilon_0(\overline{\mathbf{p}})}\,|\beta_{01}\rangle + \mathcal{O}(\sqrt{\epsilon_0(\overline{\mathbf{p}})}), \end{aligned} \tag{4.27}$$

where the phase factor $-e^{1.28i}$ is calculated by taking the inner product $\langle\beta_{01}|\,\beta_{01}^{0}\rangle$.

Note that the TRP control Hamiltonian with parameter values $\overline{\mathbf{p}}$ also produces the following states starting from the other three two-qubit computational basis states. As with $\left|\beta_{01}{}^{0}\right\rangle$, these states each carry a leading component along one of the other three Bell states $|\beta_{00}\rangle$, $|\beta_{10}\rangle$ and $|\beta_{11}\rangle$, and a small error component of order

$\mathcal{O}(\sqrt{\epsilon_0^{00}})$, $\mathcal{O}(\sqrt{\epsilon_0^{10}})$, and $\mathcal{O}(\sqrt{\epsilon_0^{11}})$, respectively:

$$
\begin{aligned}
U_{0,f}\,|01\rangle = & \begin{pmatrix} -0.7054 - 0.1678\,i \\ 0.0036 + 0.0139\,i \\ -0.0130 - 0.0143\,i \\ -0.6694 - 0.1595\,i \end{pmatrix} \\
= & -e^{0.24i}\sqrt{1-\epsilon_0^{00}}\,|\beta_{00}\rangle + \mathcal{O}(\sqrt{\epsilon_0^{00}}) \\
U_{0,f}\,|10\rangle = & \begin{pmatrix} -0.6686 - 0.1591\,i \\ 0.0188 + 0.0311\,i \\ 0.0051 - 0.0182\,i \\ 0.7053 + 0.1683\,i \end{pmatrix} \\
= & -e^{0.24i}\sqrt{1-\epsilon_0^{10}}\,|\beta_{10}\rangle + \mathcal{O}(\sqrt{\epsilon_0^{10}}) \\
U_{0,f}\,|11\rangle = & \begin{pmatrix} 0.0374 + 0.0172\,i \\ 0.1214 + 0.6853\,i \\ -0.1267 - 0.7055\,i \\ -0.0115 + 0.0006\,i \end{pmatrix} \\
= & e^{1.39i}\sqrt{1-\epsilon_0^{11}}\,|\beta_{11}\rangle + \mathcal{O}(\sqrt{\epsilon_0^{11}}).
\end{aligned}
\tag{4.28}
$$

4.2.3 NOC Strategy: Simulation Procedure

The goal is to apply the NOC strategy introduced in the previous section to reduce the error components in each of these states. I now define the following

unitary matrix to be the target gate used in the NOC formalism:

$$U_{tgt} = \begin{pmatrix} | & | & | & | \\ -e^{1.28i}\,|\beta_{01}\rangle & -e^{0.24i}\,|\beta_{00}\rangle & -e^{0.24i}\,|\beta_{10}\rangle & e^{1.39i}\,|\beta_{11}\rangle \\ | & | & | & | \end{pmatrix}. \tag{4.29}$$

As indicated in Section 4.2.2, the nominal Hamiltonian $\overline{\mathcal{H}}^0_{2,d}(\tau)$ given in Eq. (4.21) fixed by the parameter values in Table 4.1 gives rise to a unitary $U_0(\tau)$, such that $U_{0,f} = U_0(\tau_0/2)$ is a good approximation to the target gate U_{tgt} given by Eq. (4.29). Taking this as input, I then apply the NOC strategy to determine a control modification $\Delta\mathbf{F}(\tau)$, such that the new Hamiltonian

$$\overline{\mathcal{H}}_{2,d}(\tau) = \overline{\mathcal{H}}^0_{2,d}(\tau) + \sum_{j=1}^{3} \mathcal{G}_j(\tau)\Delta F_j(\tau) \tag{4.30}$$

gives rise to a new unitary $U(\tau)$ that $U(\tau_0/2)$ is a better approximation to the target gate U_{tgt}. By construction, $U(\tau_0/2)$ will map the initial state $|\psi(-\tau_0/2)\rangle = |00\rangle$ to $|\psi(\tau_0/2)\rangle = |\beta_{01}{}'\rangle$, which is a better approximated physical Bell state.

I apply Strategy 2 presented in Chapter 2.5.2 to solve for the control modification $\Delta\mathbf{F}(\tau)$. As noted earlier, $\Delta\mathbf{F}(\tau)$ is determined by solving the Ricatti equation Eq. (2.55) and the Schrodinger equation Eq. (2.57), and applying the feedback control law Eq. (2.53), with $t = b_2\tau/a$:

$$\frac{dS}{d\tau} = -Q + SGR^{-1}G^{\dagger}S, \quad S(\tau_0/2) = I_{16\times 16}, \tag{4.31}$$

$$\frac{d}{d\tau}\Delta\mathbf{y} = -GC\Delta\mathbf{y}, \quad \mathbf{y}(-\tau_0/2) = \Delta\boldsymbol{\beta}, \tag{4.32}$$

$$\Delta\mathbf{F}(\tau) = -C(\tau)\Delta\mathbf{y}(\tau). \tag{4.33}$$

Here the matrix $G(\tau)$ is obtained by concatenating the columns of $\overline{G}_j = U_0^\dagger(\tau)\mathcal{G}_j U_0(\tau)$, with $\mathcal{G}_j$ given by Eq. (4.13) and $U_0(\tau)$ determined by numerical integration of the Schrodinger equation with the nominal Hamiltonian $\overline{\mathcal{H}}_{2,d}^0(\tau)$. The initial value of $\Delta\boldsymbol{\beta}$ for Eq. (4.32) is also found by concatenating the columns of the matrix $\delta\beta = i[U_{0,f}^\dagger U_{tgt} - I]$, with $U_{0,f} = U_0(\tau_0/2)$ and U_{tgt} given by Eq. (4.29). $C(\tau) = R^{-1}(\tau)G^\dagger(\tau)S(\tau)$ is the control gain matrix.

The choice of the matrices $R(\tau)$ and $Q(\tau)$ are at our disposal. In the following simulation I chose $R(\tau) = rG^\dagger(\tau)G(\tau)$ and $S(\tau) \equiv I_{16\times 16}$, and I chose $r = 70$. Satisfying the Ricatti equation Eq. (4.31) then requires that $Q(\tau) \equiv G(G^\dagger G)^{-1}G^\dagger/r$. Combining all these ingredients I get the solution to the Ricatti equation Eq. (4.31). With the Ricatti matrix $S(\tau)$ known, the control gain matrix $C(\tau)$ is known, and Eq. (4.32) can then be integrated for $\Delta\mathbf{y}(\tau)$. With $\Delta\mathbf{y}(\tau)$ in hand, Eq. (4.33) determines the control modification $\Delta\mathbf{F}(\tau)$, which, added to the TRP control profile $\mathbf{F}_0(\tau)$, gives rise to the improved new control $\mathbf{F}(\tau) = \mathbf{F}_0(\tau) + \Delta\mathbf{F}(\tau)$. The improved new control $\mathbf{F}(\tau)$ finally determines $U(\tau)$ and $U_f = U(\tau_0/2)$ via numerical integration of the Schrodinger equation:

$$i\frac{d}{d\tau}U(\tau) = \mathcal{H}_2[\mathbf{F}(\tau)]U(\tau). \tag{4.34}$$

The state prepared by $\mathbf{F}(\tau)$ is then

$$|{\beta_{01}}^a\rangle = U_f\,|00\rangle\,, \tag{4.35}$$

whose fidelity is

$$\mathcal{F}_a = |\langle{\beta_{01}}^a|\,\beta_{01}\rangle|\,, \tag{4.36}$$

and the error probability is

$$\epsilon_a = 1 - \mathcal{F}_a^2. \tag{4.37}$$

In the following sections I present the numerical simulation results for the NOC-prepared approximated Bell state $|\beta_{01}{}^a\rangle$, for both ideal control and non-ideal control.

4.2.4 Physical Bell state $|\beta_{01}\rangle$ prepared via NOC: ideal control

With the control modification $\Delta\mathbf{F}(\tau)$ determined via the NOC numerical procedure presented in Section 4.2.3, numerically integrating the Schrodinger equation using the improved control $\mathbf{F}(\tau) = \mathbf{F}_0(\tau) + \Delta\mathbf{F}(\tau)$ in the Zeeman coupling term then drives the initial state $|00\rangle$ to the following improved state

$$|\beta_{01}{}^a\rangle = \begin{pmatrix} -0.0043 - 0.0043i \\ -0.2044 - 0.6849i \\ -0.2006 - 0.6701i \\ 0.0059 + 0.0118i \end{pmatrix} \tag{4.38}$$

which has error probability

$$\epsilon_a = 1 - |\langle\beta_{01}{}^a|\ \beta_{01}\rangle|^2 = 2.58 \times 10^{-6} \tag{4.39}$$

and fidelity $\mathcal{F}_a = 0.999999$. Therefore, NOC produces an extremely high-fidelity approximation to the Bell state $|\beta_{01}\rangle$ in a single shot.

I estimate the bandwidth needed for the NOC control modification $\Delta\mathbf{F}(t)$ from Figure 4.2 which shows the Fourier transform module $|\Delta\mathcal{F}_x(\omega)|$ of the x-component

dimensionless control field modification $\Delta\mathbf{F}_x(\tau)$; the y-and z-components behave similarly. It is shown that $|\Delta\mathcal{F}_x(\omega)|$ is reduced to 1-2% of its peak value for $|\omega| \gtrsim 60$, giving a *dimensionless* bandwidth $\Delta\omega \sim 60$. Choosing a control operation time $T = 5\mu s$, which then corresponds to the dimensionless time $\tau_0 = 120$, gives a *physical* bandwidth $\Delta\overline{\omega} \sim (120/5\mu s)\Delta\omega = 1.44\,\mathrm{GHz}$, which is within the range of some commercially available arbitrary waveform generators (AWG). From the known values of control operation time T, and the dimensionless control parameters $\overline{\mathbf{p}}$ and τ_0, it is straightforward to determine the values of the dimensionful parameters, *i.e.* the coupling constants γ_i and $J_{z,xy}$ and the TRP control parameters B, B_0 and B_{rf}. With these values, the improved (dimensionful) control $\mathbf{F}(t)$ is fully specified. Experimental application of $\mathbf{F}(t)$ to a pair of qubits in the state $|00\rangle$ leaves them in an extremely high-fidelity approximation to the Bell state $|\beta_{01}\rangle$.

4.2.5 Physical Bell state $|\beta_{01}\rangle$ prepared via NOC: non-ideal control

In this section I examine the robustness of performance of NOC to two important control imperfections: the impact of control parameters with finite precision, and phase noise in the nominal control field.

(i) Finite-precision control parameters. As seen in Section 4.2.2, the NOC formalism requires the nominal Hamiltonian ${\mathcal{H}_2}^0(\tau)$ to produce a good approximation $\left|{\beta_{01}}^0\right\rangle$ to the target state $|\beta_{01}\rangle$. The NOC control modification $\Delta\mathbf{F}(\tau)$ is optimal for ${\mathcal{H}_2}^0(\tau)$. If I shift the parameter values in ${\mathcal{H}_2}^0(\tau)$, causing it to be altered ${\mathcal{H}_2}^0(\tau) \to {\mathcal{H}_2}^{0'}(\tau)$, then $\Delta\mathbf{F}(\tau)$ may no longer be optimal for the altered Hamil-

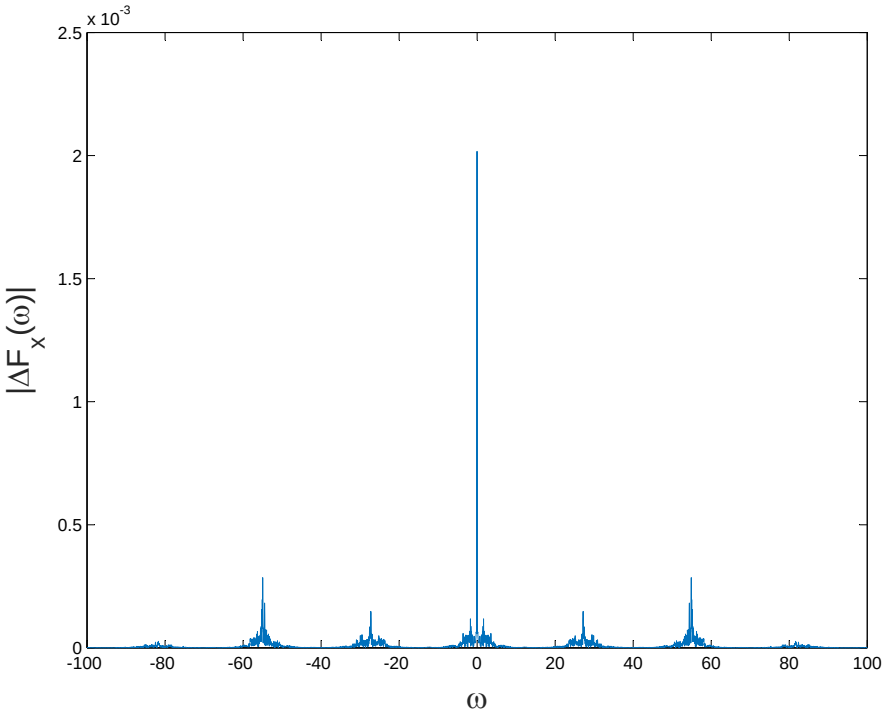

Figure 4.2: The Fourier transform module $|\Delta\mathcal{F}_x(\omega)|$ of the x-component dimensionless control modification $\Delta F_x(\tau)$ used to prepare a NOC improved approximation to the state $|\beta_{01}\rangle$. Here ω is dimensionless frequency.

tonian. Because the experimental hardware used to implement ${\mathcal{H}_2}^0(\tau)$ has limited precision, it becomes important to determine how much precision is required of the control parameters $\overline{\mathbf{p}}$ if the high-fidelity state $|{\beta_{01}}^a\rangle$ found under ideal control is to be produced.

I showed that for the control parameters with values $\overline{\mathbf{p}}$ in Table 4.1, $\mathbf{F}(\tau)$ produces the state $|{\beta_{01}}^a\rangle$, whose error probability is $\epsilon_a = 2.58 \times 10^{-6}$. To examine the robustness of this result, I shift one control parameter away from its optimum value in its the fourth significant digit, while keeping the rest at optimum. This causes ${\mathcal{H}_2}^0(\tau) \rightarrow {\mathcal{H}_2}^{0'}(\tau)$. I then numerically integrated the Schrodinger equation

with the sub-optimal Hamiltonian $\mathcal{H}'(\tau) = \mathcal{H}_2{}^{0'}(\tau) + \sum_{j=1}^{3} \mathcal{G}_j(t)\Delta F_j(\tau)$. The results are summarized in Tables 4.2-4.8. I found for example that for $\lambda = (9.579 +/- 0.001)$, the error probability changes to $\epsilon'_a = 3.35/0.789 \times 10^{-5}$, while for $\eta_4 = (4.526 +/- 0.001) \times 10^{-4}$, the error probability shifts to $\epsilon'_a = (1.35/1.90) \times 10^{-5}$. This indicates that all control parameters must be controlled to *better than* one part in 10,000 if the high-fidelity NOC performance is to be realized. This degree of control parameter precision is attainable with an AWG with 14-bit vertical resolution (viz. one part in $2^{14} = 16{,}384$). Such AWGs are commercially available. Note that 13-bit precision corresponds to a precision of one part in $2^{13} = 8192$, and so leads to uncertainty in the fourth significant digit. Thus, with less than 14 bits of precision, the NOC performance will be diminished by the uncertainty in the least significant digit of the control parameter values.

(ii) Phase/timing jitter Ideally, the clock in an AWG outputs a sequence of ticks with constant time separation T_{clock}, derived from an oscillatory process with phase $\phi(t) = (2\pi f_{clock})t$ and frequency $f_{clock} = 1/T_{clock}$. In reality, the time between ticks is a stochastic process $T = T_{clock} + \delta t$, where the timing error δt has a vanishing mean $\overline{\delta t} = 0$, and a standard deviation $\sigma_t = \sqrt{\overline{\delta t^2}}$. The timing error δt causes a phase error $\delta\phi = (2\pi f_{clock})\delta t$ which also has vanishing mean, $\overline{\delta\phi} = 0$, and its standard deviation $\sigma_\phi = \sqrt{\overline{\delta\phi^2}}$ is known as phase jitter. It is straightforward to show [66] (and in Appendix B) that $\sigma_t = \sigma_\phi/(2\pi f_{clock})$.

The timing errors introduce phase noise into the TRP control $\mathbf{F}_0(t)$. Specifically, the TRP twist angle $\phi_4(\tau) = (\eta_4/2\lambda)\tau^4$ picks up a phase noise $\delta\phi(\tau)$ due

Table 4.2: Sensitivity of error probability ϵ_a to a small variation of η_4 away from its optimum value. For all η_4 values, the other control parameters are maintained at the optimum values (the optimum value for η_4 is denoted by superscript $*$). Column 2 shows the variation of ϵ_a when the control field includes the NOC modification $\Delta\mathbf{F}(\tau)$.

η_4	ϵ_a (with NOC)
4.524×10^{-4}	5.12×10^{-5}
4.525×10^{-4}	1.90×10^{-5}
$4.526 \times 10^{-4*}$	2.58×10^{-6}
4.527×10^{-4}	1.35×10^{-5}
4.528×10^{-4}	1.35×10^{-5}

Table 4.3: Sensitivity of error probability ϵ_a to a small variation of λ away from its optimum value. For all λ values, the other control parameters are maintained at the optimum values (the optimum value for λ is denoted by superscript $*$). Column 2 shows the variation of ϵ_a when the control field includes the NOC modification $\Delta\mathbf{F}(\tau)$.

λ	ϵ_a (with NOC)
9.577	1.75×10^{-5}
9.578	7.89×10^{-6}
9.579^*	2.58×10^{-6}
9.580	3.35×10^{-5}
9.581	1.00×10^{-4}

Table 4.4: Sensitivity of error probability ϵ_a to a small variation of d_1 away from its optimum value. For all d_1 values, the other control parameters are maintained at the optimum values (the optimum value for d_1 is denoted by superscript $*$). Column 2 shows the variation of ϵ_a when the control field includes the NOC modification $\Delta\mathbf{F}(\tau)$.

d_1	ϵ_a (with NOC)
1.384	5.90×10^{-5}
1.385	2.37×10^{-5}
1.386^*	2.58×10^{-6}
1.387	1.99×10^{-5}
1.388	2.82×10^{-5}

Table 4.5: Sensitivity of error probability ϵ_a to a small variation of d_2 away from its optimum value. For all d_2 values, the other control parameters are maintained at the optimum values (the optimum value for d_2 is denoted by superscript $*$). Column 2 shows the variation of ϵ_a when the control field includes the NOC modification $\Delta\mathbf{F}(\tau)$.

d_2	ϵ_a (with NOC)
9.620	1.40×10^{-4}
9.621	5.31×10^{-5}
9.622^*	2.58×10^{-6}
9.623	2.70×10^{-5}
9.624	2.02×10^{-5}

Table 4.6: Sensitivity of error probability ϵ_a to a small variation of d_3 away from its optimum value. For all d_3 values, the other control parameters are maintained at the optimum values (the optimum value for d_3 is denoted by superscript $*$). Column 2 shows the variation of ϵ_a when the control field includes the NOC modification $\Delta\mathbf{F}(\tau)$.

d_3	ϵ_a (with NOC)
8.903	1.37×10^{-5}
8.904	4.68×10^{-6}
8.905^*	2.58×10^{-6}
8.906	8.05×10^{-6}
8.907	1.18×10^{-5}

Table 4.7: Sensitivity of error probability ϵ_a to a small variation of d_z away from its optimum value. For all d_z values, the other control parameters are maintained at the optimum values (the optimum value for d_z is denoted by superscript $*$). Column 2 shows the variation of ϵ_a when the control field includes the NOC modification $\Delta\mathbf{F}(\tau)$.

d_z	ϵ_a (with NOC)
0.916	4.18×10^{-4}
0.917	1.67×10^{-4}
0.918^*	2.58×10^{-6}
0.919	8.70×10^{-5}
0.920	8.15×10^{-5}

Table 4.8: Sensitivity of error probability ϵ_a to a small variation of d_{xy} away from its optimum value. For all d_{xy} values, the other control parameters are maintained at the optimum values (the optimum value for d_{xy} is denoted by superscript $*$). Column 2 shows the variation of ϵ_a when the control field includes the NOC modification $\Delta\mathbf{F}(\tau)$.

d_{xy}	ϵ_a (with NOC)
4.329	1.38×10^{-3}
4.330	5.59×10^{-4}
4.331^*	2.58×10^{-6}
4.332	1.33×10^{-4}
4.333	2.33×10^{-4}

to the timing error $\delta\tau$ in τ (I have switched over to dimensionless time): $\phi_4(\tau) \rightarrow \phi_4'(\tau) = \phi_4(\tau) + \delta\phi(\tau)$. This causes the TRP control to twist incorrectly and yields a noisy profile: $\mathbf{F}_0(\tau) \rightarrow \mathbf{F}_0'(\tau)$. Because the phase noise cannot be known in advance, it is not possible to determine the control modification that is optimal for the noisy control $\mathbf{F}_0'(\tau)$. All one can do is calculate the NOC modification $\Delta\mathbf{F}(\tau)$ that is optimal for the *jitter-free* TRP control $\mathbf{F}_0(\tau)$ and add it to $\mathbf{F}_0'(\tau)$ to form the new (noisy) control $\mathbf{F}'(\tau) = \mathbf{F}_0'(\tau) + \Delta\mathbf{F}(\tau)$. Since $\Delta\mathbf{F}(\tau)$ is not optimal for $\mathbf{F}_0'(\tau)$, the new control $\mathbf{F}'(\tau)$ is sub-optimal, and it can be expected that the fidelity of the NOC prepared state is reduced.

To quantitatively study the impact of phase jitter on NOC state preparation, I modelled the phase noise $\delta\phi(\tau)$ as shot noise and used the model to generate numer-

ical realizations of $\delta\phi(\tau)$. The details of the model and the protocol used to generate noise realizations are described in Ref. [66] (see also Ref. [67] and Appendix B)). Ref. [66] also showed that the average phase noise power $\overline{P}$ and the phase noise variance σ_ϕ^2 are equal. Using this result, and the formula above relating σ_t and σ_ϕ, gives $\overline{P} = (2\pi f_{clock})^2\sigma_t^2$, which relates the timing error variance to the average phase noise power introduced into the control. For each phase noise realization I determined the state $|\psi(\tau)\rangle$ by numerically integrating the Schrodinger equation driven by the noisy control $\mathbf{F}'(\tau)$ and used it to determine the error probability ϵ of the state produced. I generated 10 realizations of phase noise $\delta\phi(\tau)$ and determined 10 corresponding error probabilities. From these values, the average error probability $\overline{\epsilon}$ and standard deviation σ_ϵ were calculated and used to estimate the noise-averaged performance of NOC preparation of the state $|\beta_{01}\rangle$.

For timing jitter $\sigma_t = 5.03\,\text{ps}$ and clock frequency $f_{clock} = 1\,\text{GHz}$, typical of commercially available AWGs, the simulations found $\overline{\epsilon} \pm \sigma_\epsilon = (1.64 \pm 0.16) \times 10^{-5}$. It is shown that, although timing errors do impact NOC performance, the resulting error probabilities remain extremely small: $\epsilon \lesssim 2 \times 10^{-5}$ for commercially available AWGs.

4.2.6 Improving the approximate Bell state

The high-fidelity approximate Bell state $|{\beta_{01}}^a\rangle$ prepared via the single-shot NOC approach in Section 4.2.4, which has an error probability $\epsilon_a \sim 10^{-6}$ with ideal

control, can be written in the Bell basis as

$$|{\beta_{01}}^a\rangle = a\,|\beta_{01}\rangle + b\,|\beta_{10}\rangle + c\,|\beta_{00}\rangle + d\,|\beta_{11}\rangle \tag{4.40}$$

where

$$\begin{aligned} |a^2| &\sim 1 - \epsilon_a \\ |b|^2 + |c|^2 + |d|^2 &\sim \epsilon_a \end{aligned} \tag{4.41}$$

Other than the desired component along the $|\beta_{01}\rangle$ direction with amplitude $\sim \sqrt{1-\epsilon_a}$, the $|{\beta_{01}}^a\rangle$ state has components along the other Bell states, with amplitude $\sim \sqrt{\epsilon_a}$. In this subsection I implement a projection circuit, which takes as input the approximate Bell state $|{\beta_{01}}^a\rangle$ whose error probability is $\mathcal{O}(\epsilon)$, and returns a better approximate Bell state $|{\beta_{01}}'\rangle$ with error probability $\mathcal{O}(\epsilon^2)$.

Note that

$$\begin{aligned} \frac{(I + X_1X_2)}{2}\,|\beta_{01}\rangle &= |\beta_{01}\rangle \\ \frac{(I + X_1X_2)}{2}\,|\beta_{10}\rangle &= 0 \\ \frac{(I + X_1X_2)}{2}\,|\beta_{00}\rangle &= |\beta_{00}\rangle \\ \frac{(I + X_1X_2)}{2}\,|\beta_{11}\rangle &= 0, \end{aligned} \tag{4.42}$$

and

$$\begin{aligned} \frac{(I - Z_1Z_2)}{2}\,|\beta_{01}\rangle &= |\beta_{01}\rangle \\ \frac{(I - Z_1Z_2)}{2}\,|\beta_{10}\rangle &= 0 \\ \frac{(I - Z_1Z_2)}{2}\,|\beta_{00}\rangle &= 0 \\ \frac{(I - Z_1Z_2)}{2}\,|\beta_{11}\rangle &= |\beta_{11}\rangle\,. \end{aligned} \tag{4.43}$$

Hence $|\beta_{01}\rangle$ is stabilized by the product of the two projection operators $[\frac{(I-Z_1Z_2)}{2}][\frac{(I+X_1X_2)}{2}]$, while the other Bell states are annihilated by this product. Therefore, ideal imple-

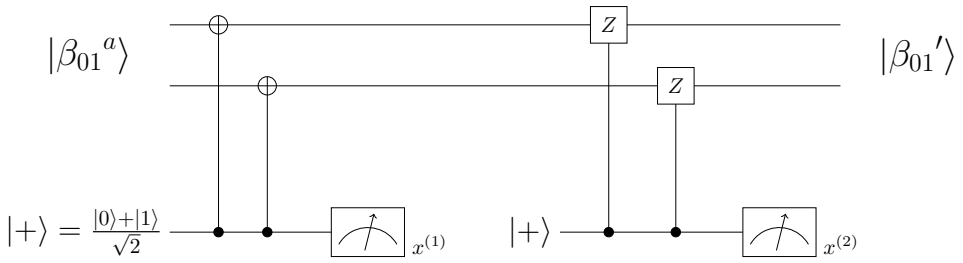

Figure 4.3: The quantum projection circuit for high-fidelity Bell state $|\beta_{01}{}'\rangle$ preparation. The output is accepted only if the first measurement result $x^{(1)}$ has even parity and the second measurement result $x^{(2)}$ has odd parity. By applying the circuit twice and accepting the final state only if both sets of parity measurements agree, the final state will have error probability $\mathcal{O}(\epsilon^2)$.

mentation of the circuit in Figure 4.3 on $|\beta_{01}{}^a\rangle$ projects out the component along $|\beta_{01}\rangle$ and annihilates components along the other Bell states.

Because real-world implementation of the projection circuit will utilize faulty gates and measurements, it is necessary to verify the measurement results. By repeating the circuit in Figure 4.3 twice and only accepting the final state if the measurement parities satisfy $x_1^{(1)} = x_2^{(1)} =$ even and $x_1^{(2)} = x_2^{(2)} =$ odd, the error probability of the output state will be $\mathcal{O}(\epsilon^2)$, where $\epsilon = \max(\epsilon_a, \epsilon_{CNOT}, \epsilon_{CZ}, \epsilon_+, \epsilon_{measurement})$. This is the level of accuracy required for the logical Bell state preparation in Section 4.3. Note that using a single ancilla for each x-parity measurement does not damage the fault-tolerance of the circuit in Figure 4.3. Examination of the consequence of a fault at any single location in the circuit shows that to $\mathcal{O}(\epsilon)$ the circuit operates correctly. Circuit failure requires at least two errors, yielding a failure probability of $\mathcal{O}(\epsilon^2)$.

4.3 Step 2: Fault-tolerant preparation of logical $\left|\overline{\beta_{01}}\right\rangle$

In this Section I describe a fault-tolerant procedure for preparing the logical Bell state $\left|\overline{\beta_{01}}\right\rangle$ which takes as input the high-fidelity Bell state prepared in Section 4.2. I give two illustrations of the procedure (Sections 4.3.1 and 4.3.2) for the $[4, 2, 2]$ quantum error detecting code C_4.

4.3.1 C_4 logical Bell state preparation with two codeblocks

In this subsection I show how to fault-tolerantly prepare the logical Bell state $\left|\overline{\beta_{01}}\right\rangle$ for the $[4, 2, 2]$ error detection code C_4 [58]. The generators for this code are [56, 57]:

$$g_1 = X_1X_2X_3X_4; \tag{4.44a}$$

$$g_2 = Z_1Z_2Z_3Z_4; \tag{4.44b}$$

and the logical Pauli operators for the logical (L) and spectator (S) qubits are:

$$\overline{X}_L = X_1X_2I_3I_4; \quad \overline{Z}_L = Z_1I_2Z_3I_4 \tag{4.1a}$$

$$\overline{X}_S = I_1X_2I_3X_4; \quad \overline{Z}_S = I_1I_2Z_3Z_4. \tag{4.1b}$$

The logical computational basis states are

$$\begin{aligned}
\left|\overline{00}\right\rangle &= N[I + g_1 + g_2 + g_1 g_2]\,|0000\rangle \\
&= \frac{1}{\sqrt{2}}[|0000\rangle + |1111\rangle] && \text{(4.1a)} \\
\left|\overline{01}\right\rangle &= \overline{X}_S \left|\overline{00}\right\rangle = \frac{1}{\sqrt{2}}[|0101\rangle + |1010\rangle] && \text{(4.1b)} \\
\left|\overline{10}\right\rangle &= \overline{X}_L \left|\overline{00}\right\rangle = \frac{1}{\sqrt{2}}[|1100\rangle + |0011\rangle] && \text{(4.1c)} \\
\left|\overline{11}\right\rangle &= \overline{X}_L \overline{X}_S \left|\overline{00}\right\rangle = \frac{1}{\sqrt{2}}[|1001\rangle + |0110\rangle], && \text{(4.1d)}
\end{aligned}$$

and the logical Bell state $\left|\overline{\beta_{01}}\right\rangle$ is

$$\begin{aligned}
\left|\overline{\beta_{01}}\right\rangle &= \frac{\left|\overline{01}\right\rangle + \left|\overline{10}\right\rangle}{\sqrt{2}} \\
&= \frac{1}{2}\left[|0101\rangle + |1010\rangle + |1100\rangle + |0011\rangle\right].
\end{aligned} \tag{4.1}$$

Consider the tensor product of two Bell states $|\beta_{01}\rangle^{\otimes 2} = |\beta_{01}\rangle \otimes |\beta_{01}\rangle$. If one labels the qubits in the first (second) pair as 1 and 2 (3 and 4), then

$$|\beta_{01}\rangle^{\otimes 2}_{12;34} = \frac{1}{2}\left[|0101\rangle + |0110\rangle + |1001\rangle + |1010\rangle\right]. \tag{4.2}$$

A simple calculation shows that the state $|\beta_{01}\rangle^{\otimes 2}_{12;34}$ is stabilized by the C_4 generators ($g_i\,|\beta_{01}\rangle^{\otimes 2}_{12;34} = |\beta_{01}\rangle^{\otimes 2}_{12;34}$, $i = 1, 2$) and so belongs to the C_4 codespace. It is straightforward to check that this state is also a simultaneous eigenvector of $\overline{X}_L$ and $\overline{Z}_S$ with respective eigenvalues 1 and -1:

$$|\beta_{01}\rangle^{\otimes 2}_{12;34} = \left|\overline{+}\right\rangle_L \left|\overline{1}\right\rangle_S. \tag{4.3}$$

If one instead labels the qubits in the first (second) pair as 1 and 3 (2 and 4), then

$$|\beta_{01}\rangle^{\otimes 2}_{13;24} = \frac{1}{2}\left[|0011\rangle + |0110\rangle + |1001\rangle + |1100\rangle\right], \tag{4.4}$$

which is found by swapping qubits 2 and 3 in Eq. (4.2). Simple calculation again shows that $|\beta_{01}\rangle^{\otimes 2}_{13;24}$ lies in the C_4 codespace and is a simultaneous eigenvector of $\overline{Z}_L$ and $\overline{X}_S$:

$$|\beta_{01}\rangle^{\otimes 2}_{13;24} = \left|\overline{1}\right\rangle_L |\overline{+}\rangle_S \,. \tag{4.5}$$

Suppose one prepares two C_4 codeblocks in the state

$$|\beta_{01}\rangle^{\otimes 2}_{12;34} \otimes |\beta_{01}\rangle^{\otimes 2}_{57;68} = |\overline{+}\rangle_L \left|\overline{1}\right\rangle_S \otimes \left|\overline{1}\right\rangle_{L'} |\overline{+}\rangle_{S'} \,. \tag{4.6}$$

Since C_4 is a CSS code [68], applying CNOT gates transversally using the LS block as the control simultaneously applies logical CNOT gates between the $L - L'$ and $S - S'$ qubits. This leads to the action

$$|\overline{+}\rangle_L \left|\overline{1}\right\rangle_S \otimes \left|\overline{1}\right\rangle_{L'} |\overline{+}\rangle_{S'} \rightarrow \left|\overline{\beta_{01}}\right\rangle_{LL'} \left|\overline{1}\right\rangle_S |\overline{+}\rangle_{S'} \,. \tag{4.7}$$

The result is that logical qubits L and L' are in the logical Bell state $\left|\overline{\beta_{01}}\right\rangle_{LL'}$ and the spectator qubits are in the unentangled state $\left|\overline{1}\right\rangle_S |\overline{+}\rangle_{S'}$.

Similarly, if one prepares the C_4 codeblocks in the state

$$|\beta_{01}\rangle^{\otimes 2}_{13;24} \otimes |\beta_{01}\rangle^{\otimes 2}_{56;78} = \left|\overline{1}\right\rangle_L |\overline{+}\rangle_S \otimes |\overline{+}\rangle_{L'} \left|\overline{1}\right\rangle_{S'} \,, \tag{4.8}$$

and apply transversal CNOT gates using the $L'S'$ codeblock as the control, this produces the action

$$\left|\overline{1}\right\rangle_L |\overline{+}\rangle_S \otimes |\overline{+}\rangle_{L'} \left|\overline{1}\right\rangle_{S'} \rightarrow \left|\overline{\beta_{01}}\right\rangle_{LL'} |\overline{+}\rangle_S \left|\overline{1}\right\rangle_{S'} \,. \tag{4.9}$$

The 1-Preparation gadgets (1-Prep) for applying the actions in Eqs. (4.7) and (4.9) appear in Figs. 4.4a and 4.4b, respectively. Applying the logical operator $\overline{X}_S$ ($\overline{X}_{S'}$) to the LS ($L'S'$) codeblock gives the final state $\left|\overline{\beta_{01}}\right\rangle_{LL'} \otimes \left|\overline{0}\right\rangle_S |\overline{+}\rangle_{S'}$

$(\left|\overline{\beta_{01}}\right\rangle_{LL'} \otimes |\overline{+}\rangle_S \left|\overline{0}\right\rangle_{S'})$ which is used at even (odd) time steps in Knill's post–selected quantum computation [57, 62].

By applying the preparation procedure in Section 4.2.3 twice one obtains two pairs of qubits in the state $|\beta'_{01}\rangle^{\otimes 2}$. By appropriate labelling of the qubits this gives a high-fidelity ($\mathcal{O}(\epsilon^2)$) approximation to the state $|\overline{+}\rangle_L \left|\overline{1}\right\rangle_S$ or $\left|\overline{1}\right\rangle_L |\overline{+}\rangle_S$. By using these states as input to the circuits in Figure 4.4 a high-fidelity approximation to the logical Bell state $\left|\overline{\beta_{01}}\right\rangle$ in the $[4, 2, 2]$ codespace is obtained.

A 1-Preparation exRec (1-Prep exRec) is formed by applying an error detection gadget (1-ED) to each codeblock exiting the 1-Prep gadget. The output state of the 1-exRec is accepted only if no error is detected by the 1-ED gadgets. Fault-tolerance requires that a single fault in the 1-Prep exRec causes no more than one error in each of the output codeblocks. From Section 4.2.6, the input state $|\beta'_{01}\rangle^{\otimes 2} = |\beta_{01}\rangle^{\otimes 2} + \mathcal{O}(\epsilon^2)$. Thus, to $\mathcal{O}(\epsilon)$, no error is present in the input state. To this same order$\mathcal{O}(\epsilon)$, at most one fault occurs in the remainder of the 1-Prep exRec. If a single 0-gate in the 1-Prep gadget is faulty, it causes at most one error in each codeblock. Such errors will be detected by the faultless trailing 1-ED gadgets, causing the state to be rejected. If instead, the fault occurs in one of the trailing 1-ED gadgets, no more than one error will appear in the output state of the 1-exRec. Thus, in all cases, a single fault does not lead to more than one error in the output state and so the 1-Prep exRec operates fault-tolerantly.

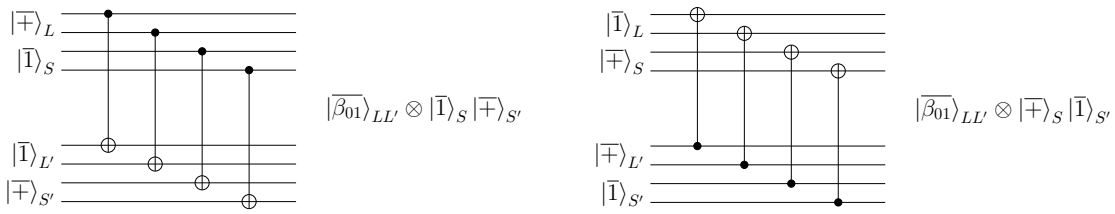

Figure 4.4: The 1-Preparation gadgets for the logical Bell state $\left|\overline{\beta_{01}}\right\rangle$. (a) This gadget leaves the logical qubits L and L' in the state $\left|\overline{\beta_{01}}\right\rangle_{LL'}$ and the spectator qubits S and S' in the state $\left|\overline{1}\right\rangle_S |\overline{+}\rangle_{S'}$. Applying $\overline{X}_S$ to the circuit output gives the final state $\left|\overline{\beta_{01}}\right\rangle_{LL'} \otimes \left|\overline{0}\right\rangle_S |\overline{+}\rangle_{S'}$ which can be used for even time step teleportation in Knill's post-selected quantum computation. (b) Here the spectator qubits are output in the state $|\overline{+}\rangle_S \left|\overline{1}\right\rangle_{S'}$. Applying $\overline{X}_{S'}$ to the lower codeblock gives the final state $\left|\overline{\beta_{01}}\right\rangle_{LL'} \otimes |\overline{+}\rangle_S \left|\overline{0}\right\rangle_{S'}$ which can be used for odd time step teleportation.

4.3.2 C_4 logical Bell state preparation with single codeblock

Here I show how to prepare a C_4 codeblock in the logical Bell state $\left|\overline{\beta_{01}}\right\rangle$, leveraging our NOC preparation procedure for the physical Bell state $|\beta_{01}\rangle$.

To begin, note that $\left|\overline{\beta_{01}}\right\rangle$ is a common eigenvector of $\overline{X}_L\overline{X}_S$ and $-\overline{Z}_L\overline{Z}_S$, both with eigenvalue 1. I showed in Section 4.3.1 that the state $|\beta_{01}\rangle_{12;34}^{\otimes 2}$ is in the C_4 codespace. Consequently, the logical projection operators

$$\prod(-\overline{Z}_L\overline{Z}_S) = \frac{1}{2}(I - \overline{Z}_L\overline{Z}_S);$$
$$\prod(\overline{X}_L\overline{X}_S) = \frac{1}{2}(I + \overline{X}_L\overline{X}_S)$$

can be used to prepare the logical Bell state $\left|\overline{\beta_{01}}\right\rangle$:

$$\left|\overline{\beta_{01}}\right\rangle = N \prod(-\overline{Z}_L\overline{Z}_S) \prod(\overline{X}_L\overline{X}_S) \, |\beta_{01}\rangle_{12;34}^{\otimes 2}\,, \tag{4.10}$$

where N is a normalization constant. In the following I suppress the $12;34$ subscript.

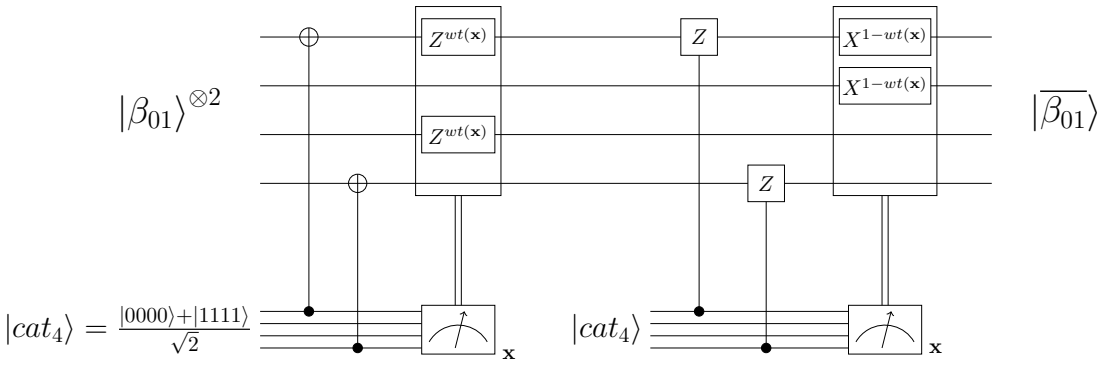

Figure 4.5: The ideal 1-Prep gadget for the logical Bell state $|\overline{\beta_{01}}\rangle$. The first (second) classically controlled gate applies $\overline{Z}_L = Z_1 I_2 Z_3 I_4$ ($\overline{X}_L = X_1 X_2 I_3 I_4$) when the measurement result gives $wt(\mathbf{x}) = 1$ ($wt(\mathbf{x}) = 0$).

The circuit in Figure 4.5 implements the action in Eq. (4.10) and serves as the ideal 1-Prep gadget for $|\overline{\beta_{01}}\rangle$. The initial state is $|\psi_0\rangle = |\beta_{01}\rangle^{\otimes 2} \otimes |cat_4\rangle$, where $|cat_4\rangle$ is the 4-physical qubit cat state (see Figure 4.5). Noting that $\overline{X}_L \overline{X}_S = X_1 I_2 I_3 X_4$, the CNOT gates apply a controlled-$\overline{X}_L \overline{X}_S$ gate to the codeblock. The qubit state after these gates is

$$\begin{aligned} |\psi_1\rangle =& \frac{1}{\sqrt{2}} \left(|\beta_{01}\rangle^{\otimes 2} \otimes |0000\rangle + \overline{X}_L \overline{X}_S |\beta_{01}\rangle^{\otimes 2} \otimes |1111\rangle \right) \\ =& \frac{1}{2} \left[\prod (\overline{X}_L \overline{X}_S) |\beta_{01}\rangle^{\otimes 2} \otimes \sum_{wt(\mathbf{x})=0} |x_1 \cdots x_4\rangle \right. \\ & \left. + \prod (-\overline{X}_L \overline{X}_S) |\beta_{01}\rangle^{\otimes 2} \otimes \sum_{wt(\mathbf{x})=1} |x_1 \cdots x_4\rangle \right]. \end{aligned} \tag{4.11}$$

Here $x_i = 0, 1$ labels the eigenvalues/eigenvectors of the X-Pauli operator: $X |x_i\rangle = (-1)^{x_i} |x_i\rangle$; $\mathbf{x} = (x_1, \cdots, x_4)$ and $wt(\mathbf{x}) = x_1 \oplus \cdots \oplus x_4$ with $\oplus$ representing the modulo 2 addition. The circuit then measures each ancilla qubit in the X-basis,

which (discarding the ancilla qubits) leaves the codeblock in the state

$$|\psi_2\rangle = \begin{cases} N \prod (\overline{X}_L \overline{X}_S) \, |\beta_{01}\rangle^{\otimes 2} & (wt(\mathbf{x}) = 0) \\ N \prod (-\overline{X}_L \overline{X}_S) \, |\beta_{01}\rangle^{\otimes 2} & (wt(\mathbf{x}) = 1), \end{cases} \tag{4.12}$$

where N is a normalization constant.

The first half of the ideal 1-Prep gadget correctly applies $\prod(\overline{X}_L \overline{X}_S)$ to $\left|\overline{\beta_{01}}\right\rangle^{\otimes 2}$ when $wt(\mathbf{x}) = 0$, and incorrectly applies $\prod(-\overline{X}_L \overline{X}_S)$ otherwise. If $\overline{Z}_L$ is applied to the codeblock when $wt(\mathbf{x}) = 1$, the projection is corrected to $\prod(\overline{X}_L \overline{X}_S)$. Thus the codeblock state after the classically controlled-$\overline{Z}_L$ gate is

$$|\psi_3\rangle = N \prod (\overline{X}_L \overline{X}_S) \, |\beta_{01}\rangle^{\otimes 2} = \frac{1}{\sqrt{2}} \left[\left|\overline{\beta_{01}}\right\rangle + \left|\overline{\beta_{00}}\right\rangle \right] \tag{4.13}$$

A similar analysis shows that the remainder of the circuit applies $\prod(-\overline{Z}_L \overline{Z}_S)$ so that the ideal 1-Prep gadget leaves the codeblock in the state

$$|\psi_{final}\rangle = N \prod (-\overline{Z}_L \overline{Z}_S) \, |\psi_3\rangle = \left|\overline{\beta_{01}}\right\rangle \tag{4.14}$$

as desired. As in Section 4.3.1, the NOC state preparation protocol can be used to produce the state $|\beta'_{01}\rangle^{\otimes 2}$ which is a high-fidelity approximation to $|\beta_{01}\rangle^{\otimes 2}$. Inputting $|\beta'_{01}\rangle^{\otimes 2}$ into the ideal 1-Prep gadget, a high-fidelity ($\mathcal{O}(\epsilon^2)$) approximation to the logical Bell state $\left|\overline{\beta_{01}}\right\rangle$ is obtained.

In reality, the circuit elements appearing in Figure 4.5 will be faulty and introduce errors into the circuit's operation. It is thus necessary to follow a non-ideal 1-Prep gadget for $\left|\overline{\beta_{01}}\right\rangle$ with a 1-ED gadget. The output of the 1-ED gadget is accepted only if no error is detected. Errors can appear through the input states, as well as through the 0-gates and 0-measurements. As the 0-gates are applied

transversally, these gates are fault-tolerant. It is showed in Section 4.3.1 that the input state $|\beta'_{01}\rangle^{\otimes 2} = |\beta_{01}\rangle^{\otimes 2} + \mathcal{O}(\epsilon^2)$ and so, to $\mathcal{O}(\epsilon)$, is exactly $|\beta_{01}\rangle^{\otimes 2}$. The cat state must be verified so that to $\mathcal{O}(\epsilon)$ it is free of bit-flip errors which would spread to the codeblock through the CNOT and controlled-Z gates. A procedure for doing this is well-known [11].

A 0-measurement error can occur either because of a faulty 0-measurement or due to a phase error in the cat state. Fault-tolerance requires that the measurement be repeated twice and the result accepted only if the two measurement results agree. Requiring $wt(\mathbf{x}_1) = wt(\mathbf{x}_2) \equiv wt(\mathbf{x})$ insures that either both measurements are incorrect (with probability $\mathcal{O}(\epsilon^2)$), or both are correct (with probability $1-\mathcal{O}(\epsilon^2)$). To $\mathcal{O}(\epsilon)$ then, both measurements are correct and the result for $wt(\mathbf{x})$ can be accepted. In light of these remarks, the 1-Prep exRec for $\left|\overline{\beta_{01}}\right\rangle$ implements the following protocol based on Figure 4.5: (1) Apply the CNOT gates; measure $\mathbf{x}$; and apply a 1-ED gadget to the codeblock. (2) Repeat Step (1) and accept the codeblock if the two measurement results agree and neither 1-ED gadget detects an error. Apply $\overline{Z}_L^{wt(\mathbf{x})}$ to the codeblock if it is accepted. (3) If the codeblock in Step (2) was accepted, apply the controlled-Z gates; measure $\mathbf{x}$; and apply a 1-ED gadget to the codeblock. (4) Repeat Step (3) and accept the codeblock if the two measurement results agree and neither 1-ED gadget detected an error. Apply $\overline{X}_L^{(1-wt(\mathbf{x}))}$ to the codeblock if it is accepted. To $\mathcal{O}(\epsilon)$, the protocol insures that an accepted codeblock contains at most one error and is thus fault-tolerant.

Chapter 5: Conclusion

In this thesis I described the application of the neighboring optimal control theory to quantum computation. I first applied the general theory of neighboring optimal control to improve the quantum gate performance, and illustrated the theory by applying it to improve all gates in a universal set $\mathcal{G}_U$ produced using a form of non-adiabatic rapid passage known as TRP. Here I stress that the NOC approach introduced here is not limited to this family of starting gates—any other good quantum gate, or set of gates, could serve as input for the method.

I also presented results from numerical simulations of applying the control modification determined by the NOC strategy to improve the gate performance, both for ideal and non-ideal control. For ideal control, I showed that the improvements are substantial : (i) for all one-qubit gates in the universal set, the gate error probabilities were reduced by *four orders-of-magnitude* ($10^{-4} \rightarrow 10^{-8}$); and (ii) for the two-qubit gate in the set, by *two orders-of-magnitude* ($10^{-3} \rightarrow 10^{-5}$).

I examined the bandwidth required to implement the ideal controls and showed that for gate times $1\mu\text{s} \leq T \leq 5\mu\text{s}$, the bandwidth Δf for all gates was in the range $130\text{MHz} \leq \Delta f \leq 820\text{MHz}$, which is within the capabilities of commercially available arbitrary waveform generators. I examined the robustness of these performance

improvements to two important sources of non-ideal control: (i) control parameters with finite precision; and (ii) timing/phase jitter resulting from clock errors in the control electronics. I found that the NOC performance gains require arbitrary waveform generators with 14-bit (17-bit) vertical resolution for the one-qubit (two-qubit) gates. I also showed that timing/phase jitter can significantly impact the NOC performance gains. It can be seen that for 5ps timing jitter (comparable to that in commercially available AWGs), the gate error probability satisfies $P_e \sim 10^{-5}$ for all the gates in the universal set, an order-of-magnitude lower than the accuracy threshold target value of 10^{-4}.

For convenience, I summarized the results for ideal control and for imperfect control with a timing jitter of $5.03ps$ in Table 5.1. For comparison I include the TrP upper bound on the gate error probability P_e for all gates with and without the neighboring optimal control improvements.

Finally, I showed that if timing jitter can be reduced to $\sigma_t = 1.26$ps, the error probability for all one-qubit gates in $\mathcal{G}_U$ drops to $P_e \sim 10^{-6}$, while the two-qubit gate error probability remains unchanged at 5.21×10^{-5}. All gates thus operate with an error probability 1–2 *orders-of-magnitude* below the target threshold of 10^{-4}. Although I focused on a target accuracy threshold $P_a = 10^{-4}$ in this thesis, I note that for surface and color quantum error correcting codes, the accuracy threshold satisfies $P_a \sim 10^{-3}$ [69–73]. For these codes, the NOC improved gates *all* operate 2–3 *orders-of-magnitude* below threshold, even for non-ideal control.

The availability of a universal set of quantum gates operating so far below threshold would have a significant impact on efforts to realize fault-tolerant quan-

Table 5.1: Simulation results for all target gates in the universal set $\mathcal{G}_U$ for ideal control and for imperfect control with a timing jitter of $5.03ps$. The first column lists the target quantum gates. The second/third columns list the $Tr\,P$ upper bound for the gate error probability P_e for gates under ideal control, whose performance has/has not been improved using neighboring optimal control (NOC). The fourth columns lists the $Tr\,P$ upper bound for gates under the timing jitter with NOC applied.

Target Gate	$P_e \leq TrP$ ideal with NOC	$P_e \leq TrP$ ideal without NOC	$P_e \leq TrP$ with timing jitter with NOC
NOT	$\leq 8.58 \times 10^{-9}$	$\leq 6.27 \times 10^{-5}$	$(2.04 \pm 1.80) \times 10^{-5}$
Hadamard	$\leq 1.04 \times 10^{-8}$	$\leq 1.12 \times 10^{-4}$	$(2.11 \pm 1.64) \times 10^{-5}$
Modified $\pi/8$	$\leq 1.06 \times 10^{-8}$	$\leq 2.13 \times 10^{-4}$	$(2.92 \pm 1.96) \times 10^{-5}$
Modified phase	$\leq 1.08 \times 10^{-8}$	$\leq 4.62 \times 10^{-4}$	$(3.04 \pm 2.16) \times 10^{-5}$
Modified controlled-phase	$\leq 5.21 \times 10^{-5}$	$\leq 1.27 \times 10^{-3}$	$(5.21 \pm 0.00) \times 10^{-5}$

tum computing as it would greatly reduce the resources needed to implement such a computation. It is hoped that the NOC gate performance improvements found in this paper might encourage an attempt to produce these high-fidelity gates experimentally.

In Chapter4 I adapted the NOC theory to create a two-step procedure for logical state preparation, and I illustrated this procedure by using it to prepare a logical Bell state $\left|\overline{\beta_{01}}\right\rangle$. The NOC theory was applied in Step 1 of the procedure to prepare a high-fidelity approximate physical Bell state $|{\beta_{01}}^a\rangle$ in a single shot. Numerical simulation results were presented for both ideal and non-ideal control. I

showed that this single-shot NOC approach is able to achieve a preparation error probability of $\epsilon \sim 10^{-6}$ for ideal control. This required a bandwidth of 1.44 GHz given a control operation time of $5\,\mu s$, and a vertical resolution of 14-bit for control parameters, all within the range of commercially available arbitrary waveform generators (AWG) [51, 52]. In Section4.2.5 I showed that when the control is subject to timing jitter error, the NOC performance would be impacted, while the resulting error probabilities remain extremely small: $\epsilon \lesssim 2 \times 10^{-5}$ for the level of timing jitter noise that is typical for commercially available AWGs. In Step 2, I took copies of the high-fidelity physical Bell states $|\beta_{01}\rangle$ prepared via Step 1, and sent them through a simple quantum circuit which fault-tolerantly prepares the logical Bell state $\left|\overline{\beta_{01}}\right\rangle$ using the C_4 quantum error detection code.

Throughout this thesis, I assumed that the qubit longitudinal (T_1) and transverse (T_2) relaxation times are long compared to the gate operation time T_{gate} for achieving the gate performance improvement, and the control operation time $T_{control}$ for preparing the approximate physical Bell state $|\beta_{01}{}^{a}\rangle$. This assumption is essential for any discussion of fault-tolerant quantum computing and error correction as it insures that the qubit state does not decohere before the error-syndrome extraction circuit can be applied, and errors identified. When $T_1, T_2 \gg T_{gate}, T_{control}$, control imperfections are expected to be the primary source of errors during the control operation, and the qubit environment a secondary source. On the other hand, when $T_1, T_2 \lesssim T_{gate}, T_{control}$, the qubits are of sufficiently poor quality that errors from the qubit environment can be expected to be (at least) as bad as the types of errors I have examined in this thesis. The NOC strategy presented in this thesis for improv-

ing quantum gate performance and for high-fidelity physical state preparation does not remove the need for high-quality qubits as the object of the control operations.

Appendix A: Twisted Rapid Passage: A Few Results

I illustrated the general theory developed in Chapter 2 by using it in Chapter 3 to improve the performance of a universal set of quantum gates. The gates are using a form of non-adiabatic rapid passage known as twisted rapid passage (TRP) [38]- [44]. In Section 3.1 I provided a brief introduction to TRP. Here I review TRP. Appendix A.1 presents a derivation of the dimensionless one- and two-qubit Hamiltonians used to drive the quantum gates produced using TRP. Appendix A.2 derives an expression for the gate error probability, as well as a convenient upper bound for it. I stress that the NOC approach to improving a good quantum gate (or set of gates) is not limited to this TRP-generated family of gates. Any good gate could provide the starting point for the method.

A.1 One- and two-qubit Hamiltonians

(a) For the one-qubit gates studied in this paper, the qubit is assumed to couple to an external control field $\mathbf{F}(t)$ through the Zeeman-interaction,

$$H_0^1(t) = -\boldsymbol{\sigma} \cdot \mathbf{F}(t), \tag{A.1}$$

where $\mathbf{F}(t)$ has the TRP profile,

$$\mathbf{F}(t) = at\hat{\mathbf{z}} + b\cos\phi_4(t)\hat{\mathbf{x}} + b\sin\phi_4(t)\hat{\mathbf{y}}. \tag{A.2}$$

For a quartic twist, $\phi_4(t) = (1/2)Bt^4$ for $-T/2 \leq t \leq T/2$. The Schrodinger equation for the propagator $U(t, -T/2)$ is

$$i\hbar\frac{dU(t)}{dt} = \left[-at\sigma_z - b\cos\phi_4(t)\sigma_x - b\sin\phi_4(t)\sigma_y\right]U(t), \tag{A.3}$$

where I have suppressed the $-T/2$ dependence in $U(t, -T/2)$. It is useful to express Eq. (A.3) in dimensionless form. To that end I define: (i) the dimensionless time $\tau = (a/b)t$; (ii) the dimensionless inversion rate $\lambda = \hbar a/b^2$; and (iii) the dimensionless twist strength $\eta_4 = \hbar B b^2/a^3$. In terms of these parameters, Eq. (A.3) becomes

$$i\frac{dU(\tau)}{d\tau} = H_0^1(\tau)U(\tau), \tag{A.4}$$

where the dimensionless one-qubit Hamiltonian is

$$H_0^1(\tau) = \frac{1}{\lambda}\left[-\tau\sigma_z - \cos\phi_4(\tau)\sigma_x - \sin\phi_4(\tau)\sigma_y\right], \tag{A.5}$$

and $\phi_4(\tau) = (\eta_4/2\lambda)\tau^4$. This is the nominal one-qubit Hamiltonian discussed in Section 3.2 that drives the numerical simulation of all one-qubit gates considered in this paper.

(b) I next derive the dimensionless nominal two-qubit Hamiltonian $H_0^2(\tau)$ discussed in Section 3.2 and which drives the numerical simulations of the two-qubit modified controlled phase gate. Although a more general discussion is possible, it proves convenient to adopt the language of NMR which was the original experimental setting for TRP [39, 74].

The two-qubit Hamiltonian contains terms that Zeeman-couple each qubit to an external control field $\mathbf{F}(t)$, and an Ising interaction term that couples the two qubits. Note that alternative two-qubit interactions can easily be considered by straightforward modification of the following arguments. Our starting point is thus the Hamiltonian

$$\frac{\overline{H}^{2}_{0}(t)}{\hbar} = -\frac{1}{2}\sum_{i=1}^{2} \gamma_i \, \boldsymbol{\sigma}^i \cdot \mathbf{F}(t) - \frac{\pi}{2} J \, \sigma_z^1 \sigma_z^2, \tag{A.6}$$

where γ_i is the gyromagnetic ratio for qubit i, and J is the Ising interaction coupling constant. In the lab frame, $\mathbf{F}(t)$ has a static component $B_0 \, \hat{\mathbf{z}}$ and a time-varying component $2B_{rf} \cos \phi_{rf}(t) \, \hat{\mathbf{x}}$. In the rotating wave approximation $\mathbf{F}(t)$ reduces to

$$\mathbf{F}(t) = B_0 \, \hat{\mathbf{z}} + B_{rf} \cos \phi_{rf}(t) \, \hat{\mathbf{x}} - B_{rf} \sin \phi_{rf}(t) \, \hat{\mathbf{y}}. \tag{A.7}$$

Introducing $\omega_i = \gamma_i B_0$ and $\omega_i^{rf} = \gamma_i B_{rf}$ $(i = 1, 2)$, and inserting Eq. (A.7) into Eq. (A.6) gives

$$\begin{aligned} \frac{\overline{H}^{2}_{0}(t)}{\hbar} \;=\; & \sum_{i=1}^{2} \left[-\frac{\omega_i}{2}\sigma_z^i - \frac{\omega_i^{rf}}{2} \left\{ \cos \phi_{rf} \sigma_x^i - \sin \phi_{rf} \sigma_y^i \right\} \right] \\ & -\frac{\pi}{2} J \, \sigma_z^1 \sigma_z^2. \end{aligned} \tag{A.8}$$

Transformation to the detector frame is done via the unitary operator

$$U_{det}(t) = \exp \left[\, (i\phi_{det}(t)/2) \left(\sigma_z^1 + \sigma_z^2 \right) \right].$$

The Hamiltonian in the detector frame is then [45]

$$\begin{aligned}\frac{\tilde{\mathrm{H}}_0^2(t)}{\hbar} &= U_{det}^{\dagger}\left(\frac{\overline{H}_0^2(t)}{\hbar}\right)U_{det} - iU_{det}^{\dagger}\frac{dU_{det}}{dt} \\ &= \sum_{i=1}^{2}\Big[\Big(-\frac{\omega_i}{2}+\dot{\phi}_{det}\Big)\sigma_z^i \\ &\quad -\frac{\omega_i^{rf}}{2}\left\{\cos\left(\phi_{det}-\phi_{rf}\right)\sigma_x^i\right. \\ &\quad \left.+\sin\left(\phi_{det}-\phi_{rf}\right)\sigma_y^i\right\}\Big] \\ &\quad -\frac{\pi}{2}\,J\,\sigma_z^1\sigma_z^2. \end{aligned} \tag{A.9}$$

To produce a TRP sweep in the detector frame it is necessary to sweep $\dot{\phi}_{det}$ and $\dot{\phi}_{rf}$ through a Larmor resonance frequency [39, 74]. I choose (somewhat arbitrarily) to sweep through the Larmor frequency ω_2:

$$\begin{aligned}\dot{\phi}_{det} &= \omega_2 + \frac{2at}{\hbar} + \Delta \\ \dot{\phi}_{rf} &= \dot{\phi}_{det} - \dot{\phi}_4. \end{aligned} \tag{A.10}$$

Here $\phi_4(t) = (1/2)Bt^4$ is the twist profile for quartic TRP, and I have introduced a frequency shift parameter Δ whose value is determined by the sweep parameter optimization procedure described in Ref. [42]. Inserting Eqs. (A.10) into Eq. (A.9), and introducing $\delta\omega = \omega_1 - \omega_2$ and $b_i = \hbar\omega_i^{rf}/2$ $(i = 1, 2)$ yield

$$\begin{aligned}\frac{\tilde{\mathrm{H}}_0^2(t)}{\hbar} &= \left[-\frac{(\delta\omega+\Delta)}{2}+\frac{at}{\hbar}\right]\sigma_z^1 + \left[-\frac{\Delta}{2}+\frac{at}{\hbar}\right]\sigma_z^2 \\ &\quad -\frac{b_1}{\hbar}\left[\cos\phi_4\,\sigma_x^1 + \sin\phi_4\,\sigma_y^1\right] \\ &\quad -\frac{b_2}{\hbar}\left[\cos\phi_4\,\sigma_x^2 \sin\phi_4\,\sigma_y^2\right] \\ &\quad -\frac{\pi}{2}\,J\,\sigma_z^1\sigma_z^2. \end{aligned} \tag{A.11}$$

Here both qubits are acted on by a quartic TRP sweep in the detector frame.

In keeping with my earlier choice of sweeping through the Larmor resonance of the second qubit, I use b_2 in the definitions of the dimensionless time τ, inversion rate λ, and twist strength η_4:

$$\tau = \left(\frac{a}{b_2}\right) t \tag{A.12}$$

$$\lambda = \frac{\hbar a}{(b_2)^2} \tag{A.13}$$

$$\eta_4 = \left(\frac{\hbar B}{a^3}\right) (b_2)^2 . \tag{A.14}$$

Since $\tilde{\mathrm{H}}_0^2(t)/\hbar$ has units of inverse-time, and b_2/a has units of time (Eq. (A.12)), multiplying Eq. (A.11) by b_2/a and using Eqs. (A.12)–(A.14) gives the dimensionless two-qubit Hamiltonian $\tilde{\mathrm{H}}_0^2(\tau)$:

$$\begin{aligned}\tilde{\mathrm{H}}_2(\tau) = & \left[-\frac{(d_1+d_2)}{2}+\frac{\tau}{\lambda}\right]\sigma_z^1+\left[-\frac{d_2}{2}+\frac{\tau}{\lambda}\right]\sigma_z^2 \\ & -\frac{d_3}{\lambda}\left[\cos\phi_4\,\sigma_x^1+\sin\phi_4\,\sigma_y^1\right] \\ & -\frac{1}{\lambda}\left[\cos\phi_4\,\sigma_x^2+\sin\phi_4\,\sigma_y^2\right] \\ & -\frac{\pi}{2}\,d_4\,\sigma_z^1\sigma_z^2,\end{aligned} \tag{A.15}$$

where

$$\begin{aligned} d_1 &= \left(\frac{\delta\omega}{a}\right) b_2 \\ d_2 &= \left(\frac{\Delta}{a}\right) b_2 \\ d_3 &= \frac{b_1}{b_2} \\ d_4 &= \left(\frac{J}{a}\right) b_2. \end{aligned} \tag{A.16}$$

As noted in Section 3.2, $\tilde{\mathrm{H}}_2(\tau)$ has a degeneracy in the resonance frequency of the energy level pairs $(E_1 \leftrightarrow E_2)$ and $(E_3 \leftrightarrow E_4)$. To break this degeneracy I add

the term

$$\Delta H = c_4 \, |E_4(\tau)\rangle\langle E_4(\tau)| \tag{A.17}$$

to $\tilde{\mathrm{H}}_0^2(\tau)$, where $|E_4(\tau)\rangle$ is the instantaneous energy eigenstate of $\tilde{\mathrm{H}}_0^2(\tau)$ with eigenvalue $E_4(\tau)$. Thus

$$H_0^2(\tau) = \tilde{\mathrm{H}}_0^2(\tau) + \Delta H \tag{A.18}$$

which is the Hamiltonian given in Eq. (3.10). The Hamiltonian $H_0^2(\tau)$ depends on the TRP sweep parameters (λ, η_4), as well as on the parameters $(d_1, \ldots, d_4)$ and c_4. Eq. (A.16) shows that d_1, d_2, d_3, and d_4 are the dimensionless versions of, respectively, the Larmor frequency difference $\delta\omega = \omega_1 - \omega_2$, the frequency shift parameter Δ, the ratio $b_1/b_2 = \gamma_1/\gamma_2$, and the Ising coupling constant J.

For a derivation of the one-qubit TRP Hamiltonian (Eq. (A.1)) based on an NMR experimental implementation, see the Appendix of Ref. [38].

A.2 Gate error probability

The following argument is for an N-dimensional Hilbert space. As in Section 3.2, let U_a denote the actual unitary operation produced by a given set of TRP sweep parameters, and U_{tgt} a target unitary operation we would like TRP to approximate as closely as possible. Introducing the operators $D = U_a - U_{tgt}$ and $P = D^\dagger D$, and the normalized state $|\psi\rangle$, I define $|\psi_a\rangle = U_a|\psi\rangle$ and $|\psi_{tgt}\rangle = U_{tgt}|\psi\rangle$. Now choose an orthonormal basis $|i\rangle$ $(i = 1, \ldots, N)$ such that $|1\rangle \equiv |\psi_{tgt}\rangle$ and define

the state $|\xi_\psi\rangle$ via

$$|\psi_a\rangle = |\psi_{tgt}\rangle + |\xi_\psi\rangle \quad (A.19)$$

$$= |1\rangle + |\xi_\psi\rangle \ . \quad (A.20)$$

Inserting $|\xi_\psi\rangle = \sum_{i=1}^{N} e_i|i\rangle$ into eq. (A.20) gives

$$|\psi_a\rangle = (1+e_1)\,|1\rangle + \sum_{i\neq 1} e_i|i\rangle \ . \quad (A.21)$$

Since $|\psi_{tgt}\rangle = |1\rangle$ is the target state, it is clear from Eq. (A.21) that the error probability $P_e(\psi)$ for U_a (i. e. TRP) is

$$P_e(\psi) = \sum_{i\neq 1} |e_i|^2 \ . \quad (A.22)$$

I now define the error probability P_e for the TRP gate to be

$$P_e \equiv \max_{|\psi\rangle} P_e(\psi) \ . \quad (A.23)$$

From Eq. (A.19),

$$|\xi_\psi\rangle = D|\psi\rangle$$

and

$$\langle\xi_\psi|\xi_\psi\rangle = \langle\psi|D^\dagger D|\psi\rangle$$

$$= Tr\rho_\psi P \ , \quad (A.24)$$

where $\rho_\psi = |\psi\rangle\langle\psi|$. On the other hand,

$$\langle\xi_\psi|\xi_\psi\rangle = \sum_{i=1}^{N} |e_i|^2$$

$$= |e_1|^2 + P_e(\psi) \ . \quad (A.25)$$

Combining Eqs. (A.24) and (A.25) gives

$$P_e(\psi) = \langle \xi_\psi | \xi_\psi \rangle - |e_1|^2 \tag{A.26}$$

$$\leq \langle \xi_\psi | \xi_\psi \rangle = Tr \rho_\psi P \ . \tag{A.27}$$

Since $P = D^\dagger D$ is Hermitian it can be diagonalized: $P = O^\dagger d\, O$ and $d = diag(d_1, \ldots, d_N)$. Thus

$$P_e(\psi) \leq Tr\, \overline{\rho}_\psi d \ , \tag{A.28}$$

where $\overline{\rho}_\psi = O \rho_\psi O^\dagger$. Let $d_* = \max(d_1, \ldots, d_N)$, then direct evaluation of the trace gives

$$Tr\, \overline{\rho}_\psi d = \sum_{i=1}^{N} d_i \left(\overline{\rho}_\psi\right)_{ii} \tag{A.29}$$

$$\leq \sum_{i=1}^{N} d_* \left(\overline{\rho}_\psi\right)_{ii} = d_*\, Tr\, \overline{\rho}_\psi = d_* \ , \tag{A.30}$$

where I have used that $Tr\, \overline{\rho}_\psi = 1$. Thus $P_e(\psi) \leq d_*$ for *all* states $|\psi\rangle$. From Eq. (A.23), it follows that

$$P_e \leq d_* \ , \tag{A.31}$$

so that the largest eigenvalue d_* of P is an upper bound for the gate error probability P_e. Finally, notice that $P = D^\dagger D$ is a positive operator so that $d_i \geq 0$ for $i = 1, \ldots, N$. Thus $d_* \leq Tr\, P$ and so

$$P_e \leq d_* \leq Tr\, P \ . \tag{A.32}$$

Although $Tr\, P$ need not be as tight an upper bound on P_e as d_*, it is much easier to calculate and so is more convenient than d_* for use in my numerical simulations.

Appendix B: Modeling phase noise effects

In this Appendix I present the noise model that I used to study the impact of phase noise on the NOC improved TRP gates presented in Section 3.3 and the NOC prepared physical Bell state presented in Section 4.2.5. Appendix B.1 introduces the noise model and establishes key relations between the noise parameters; while Appendix B.2 describes how a realization of phase noise with arbitrary power is generated, as well as the protocol used to simulate the noisy Schrodinger gate dynamics.

B.1 Noise model

I start with a few basic facts about stationary random processes. The rate at which a noise field $N(t)$ can do work (*i.e.* noise power) is [75],

$$P = N^2(t),$$

and the energy that can be delivered in a time interval dt is,

$$dE = N^2(t)\, dt.$$

Consider power-type noise for which the time-averaged noise power

$$\overline{P} = \lim_{T\to\infty} \frac{1}{T} \int_{-T/2}^{T/2} N^2(t)\, dt \tag{B.1}$$

is finite. The total noise energy

$$E = \int_{-\infty}^{\infty} dt\, N^2(t) \tag{B.2}$$

diverges for this class of noise. The divergence is due to the occurrence of an infinite number of noise fluctuations in the time interval $-\infty < t < \infty$. The energy of an individual fluctuation is, however, finite.

The time-averaged noise power $\overline{P}$ can be related to the noise correlation function,

$$\overline{N(t)N(t-s)} \equiv \lim_{T\to\infty} \frac{1}{T} \int_{-T/2}^{T/2} dy\, N(y)N(y-s). \tag{B.3}$$

Comparing Eqs. (B.1) and (B.3) yields,

$$\overline{P} = \overline{N^2(t)}. \tag{B.4}$$

The Weiner-Khintchine theorem [76] shows that the noise correlation function and the power spectral density $S_N(f)$ form a Fourier transform pair:

$$\overline{N(t)N(t-s)} = \int_{-\infty}^{\infty} df\, S_N(f)\, e^{-2\pi i f s}. \tag{B.5}$$

Thus, it follows from Eqs. (B.4) and (B.5) that

$$\overline{P} = \int_{-\infty}^{\infty} df\, S_N(f), \tag{B.6}$$

which identifies $S_N(f)$ as the mean noise power available in the frequency interval $(f,\, f + df)$.

In the remainder of this Appendix I focus on phase noise $\delta\phi(\tau)$, where τ is the dimensionless time introduced in Appendix A. I model this noise as shot noise which is a common type of electronic noise. The presentation extends earlier work

in Ref. [67]. It is straight-forward to adapt the following development to treat other forms of noise.

As shot noise, the phase noise $\delta\phi(\tau)$ is produced by a sequence of randomly occurring noise fluctuations $F(t)$. The fluctuations: (1) occur independently of each other at average rate $\overline{n}$ per unit time; (2) are uniformly distributed over the time interval $[-\tau_0/2, \tau_0/2]$ of the TRP inversion; and (3) have a peak value x which is Gaussian distributed with mean $\overline{x} = 0$, variance $\overline{x^2} = \sigma^2$, and temporal width $2\tau_f$ which is the fluctuation lifetime. I assume that $2\tau_f$ is much shorter than the TRP inversion time τ_0. The bandwidth of $F(\tau)$ is thus $\Delta\omega \sim 1/2\tau_f$. Thus a realization of the phase noise has the form

$$\delta\phi(\tau) = \sum_{i=1}^{\mathcal{N}_f} F(\tau - \tau_i), \tag{B.7}$$

where $\mathcal{N}_f$ denotes the number of noise fluctuations present (a stochastic variable), i labels the noise fluctuations, and τ_i specifies the center of the ith fluctuation.

The mean number of fluctuations $\overline{\mathcal{N}_f}$ occurring in the time interval $[-\tau_0/2, \tau_0/2]$ is $\overline{\mathcal{N}_f} = \overline{n}\,\tau_0$. It is well-known that for noise with these properties, the actual number of fluctuations n that occur in a time τ_0 is governed by the Poisson distribution [77]:

$$p(n) = \frac{(\overline{\mathcal{N}_f})^n}{n!}\, e^{-\overline{\mathcal{N}_f}}.$$

The energy present in a single fluctuation is:

$$\varepsilon = \int_{-\infty}^{\infty} F^2(\tau)\, d\tau. \tag{B.8}$$

Let $F(\tau) = xh(\tau)$, where $h(\tau)$ is any convenient function of finite support with

normalization

$$\int_{-\infty}^{\infty} d\tau\, h^2(\tau) = 2\tau_f. \tag{B.9}$$

As mentioned above, x is Gaussian distributed with mean $\overline{x} = 0$ and variance $\overline{x^2} = \sigma^2$. From Eq. (B.8), $\varepsilon = 2x^2\,\tau_f$, and the mean energy per fluctuation $\overline{\varepsilon}$ is,

$$\overline{\varepsilon} = 2\,\overline{x^2}\,\tau = 2\sigma^2\,\tau. \tag{B.10}$$

For shot noise, the power spectral density for $\delta\phi(\tau)$ is [78]

$$S_\phi(f) = \overline{n}\,|g(f)|^2, \tag{B.11}$$

where $g(f)$ is the Fourier transform of the fluctuation profile $F(t)$. Thus, using Eqs. (B.6), (B.11), and Paresval's theorem gives,

$$\overline{P} = \overline{n} \int_{-\infty}^{\infty} d\tau\, F^2(\tau). \tag{B.12}$$

Finally, using Eqs. (B.8) and (B.10) gives,

$$\overline{P} = 2\,\overline{n}\,\sigma^2\,\tau_f. \tag{B.13}$$

Thus the noise model I used is characterized by any three of the parameters $\overline{P}$, $\overline{n}$, σ^2, and τ_f.

I close this section by deriving an important connection between the mean noise power $\overline{P}$ and the phase jitter σ_ϕ introduced in Section 3.4.2. From Eq. (B.7), we have

$$\delta\phi^2(\tau) = \sum_{i,j=1}^{\mathcal{N}_f} F(\tau - \tau_i)F(\tau - \tau_j). \tag{B.14}$$

Averaging over the noise gives

$$\overline{\delta\phi^2(\tau)} = \overline{\mathcal{N}_f}\,\overline{F^2(\tau)}, \tag{B.15}$$

where I have used the statistical independence of distinct noise fluctuations, and that $2\tau_f \ll \tau_0$. As in the proof of Campbell's theorem [79], it is possible to show that

$$\overline{F^2(\tau)} = \int_{-\infty}^{\infty} \frac{d\tau}{\tau_0}\, \sigma^2\, h^2(\tau), \tag{B.16}$$

where, recall $F(\tau) = xh(\tau)$, and $\overline{x^2} = \sigma^2$. Inserting Eq. (B.16) and $\sigma_\phi = \sqrt{\overline{\delta\phi^2(\tau)}}$ into Eq. (B.15) gives

$$\sigma_\phi^2 = \frac{\overline{\mathcal{N}_f}}{\tau_0}\sigma^2 \int_{-\infty}^{\infty} d\tau\, h^2(\tau). \tag{B.17}$$

Finally, inserting Eqs. (B.9) and (B.13), and $\overline{\mathcal{N}_f} = \overline{n}\tau_0$ into Eq. (B.17) gives

$$\sigma_\phi = \sqrt{\overline{P}}. \tag{B.18}$$

Thus the phase jitter σ_ϕ is simply another way to represent the phase noise power $\overline{P}$. Using Eq. (3.16), I can also express the timing jitter σ_t in terms of $\overline{P}$:

$$\sigma_t = \frac{\sqrt{\overline{P}}}{(2\pi f_{clock})}. \tag{B.19}$$

B.2 Noisy simulation protocol

The numerical simulations that I used to study the impact of phase jitter on the NOC improved TRP gates constructs a realization of phase noise as follows. I first sample a positive integer $\mathcal{N}_f$ according to the Poisson distribution with mean $\overline{\mathcal{N}_f} = \overline{n}\,\tau_0$, where τ_0 is the (dimensionless) TRP inversion time. N_f corresponds to the number of fluctuations present in the noise realization. The noise model assume these fluctuations occur independently with probability $dp_f = (1/\tau_0)d\tau$. I sample $\mathcal{N}_f$ numbers τ_i $(i = 1, \cdots, \mathcal{N}_f)$ from the interval $(-\tau_0/2, \tau_0/2)$. The τ_i give the temporal

centers of the $\mathcal{N}_f$ fluctuations. For simplicity, I assume that the fluctuation profile $h(\tau)$ is a square pulse of duration $2\tau_f$. I next carry out $\mathcal{N}_f$ samples x_i $(i = 1, \cdots, \mathcal{N}_f)$ of a Gaussian distribution with mean $\overline{x}_i = 0$ and variance $\overline{x_i^2} = \sigma^2$. Here x_i is the peak value of the ith fluctuation. These sample results produce the noise realization $\delta\Phi(\tau)$:

$$\delta\Phi(\tau) = \sum_{i=1}^{\mathcal{N}_f} x_i \left[\frac{\mathrm{sgn}(\tau - \tau_{il}) - \mathrm{sgn}(\tau - \tau_{ir})}{2} \right], \tag{B.20}$$

where $\tau_{il} = \tau_i - \tau_f$, and $\tau_{ir} = \tau_i + \tau_f$. To produce noise realizations with arbitrary mean noise power $\overline{P}$ is needed. I do this by the following normalization procedure. First I calculate the mean noise power $\overline{\mathcal{P}}$ of the noise realization $\delta\Phi(\tau)$ just produced:

$$\overline{\mathcal{P}} = \frac{1}{\tau_0} \int_{-\tau_0/2}^{\tau_0/2} d\tau\, \delta\Phi^2(\tau). \tag{B.21}$$

Then, if the desired value for the noise power is $\overline{P}$, I rescale $\delta\Phi(\tau)$ in Eq. (B.20) so that $\delta\Phi(\tau) \to \delta\phi(\tau) \equiv \sqrt{\overline{P}/\overline{\mathcal{P}}}\,\delta\Phi(\tau)$. The result is a noise realization $\delta\phi(\tau)$ with mean noise power $\overline{P}$.

The simulation takes as inputs the mean noise power $\overline{P}$, the standard deviation $\sqrt{\overline{x_i^2}} = \sigma$, and τ_f which is half the fluctuation lifetime. The fluctuation rate $\overline{n}$ then follows from Eq. (B.13): $\overline{n} = \overline{P}/(2\sigma^2\tau_f)$. In all the one (two) qubit gate simulations, I used $\sigma = 0.1$ (0.1) and $\tau_f = 0.3$ (0.1). All one-qubit gates were run at mean noise power $\overline{P} = 0.001, 0.008$ corresponding to timing jitter $\sigma_t = 5.03\text{ps}, 14.2\text{ps}$, respectively. The Hadamard gate was run at seven other values of $\overline{P}$ to produce the data displayed in Figure 3.12. The two-qubit gate was run at $\overline{P} = 0.001, 0.005$ corresponding to timing jitter $\sigma_t = 5.03\text{ps},\ 11.3\text{ps}$.

For a given target gate, and given values of $(\overline{P}, \sigma, \tau_f)$, ten phase noise realizations $\delta\phi(\tau)$ were generated. For each realization, the phase noise was added to the TRP twist phase $\phi_4(\tau)$, and the resulting noisy twist phase $\phi_4'(\tau)$ caused the noisy TRP control field $\mathbf{F}_0'(\tau)$ to twist incorrectly, as described in Section 3.4.2. For each noise realization: (i) the state trajectory $U(\tau)$ was determined by numerically simulating the Schrodinger dynamics generated by the noisy control field $\mathbf{F}'(\tau) = \mathbf{F}_0'(\tau) + \Delta\mathbf{F}(\tau)$ (see Section 3.4.2); and (ii) used to determine the $Tr\,P$ upper bound for the gate error probability P_e. Using the ten values of $Tr\,P$ obtained from the simulations, the average $\langle Tr\,P\rangle$ and standard deviation $\sigma(TrP)$ were then calculated and the noise-averaged NOC gate performance was then approximated by $P_e \leq \langle Tr\,P\rangle \pm \sigma(TrP)$. The results of these simulations appear in Section 3.4.2.

In the following I present a sample `Matlab` code that I used to generate the noisy phase $\phi(\tau) = \phi_{0,TRP}(\tau) + \delta\phi(\tau)$, where $\phi_{0,TRP}(\tau)$ is the jitter-free TRP quartic phase, and $\delta\phi(\tau)$ is the random phase noise. It follows from Eqs. (B.19) that a phase noise power $\overline{P} = 0.001$ corresponds a timing jitter of 5.03 ps, for a clock frequency $f_{clock} = 1\,\text{GHz}$. As discussed in Section 3.4.2 and 4.2.5, I then used the noisy phase $\phi(\tau)$ in place of the noiseless phase $\phi_{0,TRP}(\tau)$ to give rise to the noisy TRP control field $\mathbf{F}_0'(\tau)$, which, together with the NOC modification obtained from the noiseless TRP trajectory $U_0(\tau)$, determines the noisy state trajectory $U'(\tau)$.

```
pbar = 0.001; % time-averaged phase noise power, corresponding a
                timing jitter of 5.03 ps
sigma = 0.1; % standard deviation of the phase noise strength
               (phase jitter)
tau = 0.1; % 2*tau is the life time of each noise
nbar = pbar/(2*sigma^2*tau); % number of noise fluctuations per
                                unit time
Nf = poissrnd(120*nbar); % total number of noise fluctuations; a
                           Poisson random number with mean 120*nbar
h = normrand(0,sigma,Nf,1); % strength of each fluctuation,
                         following a normal distribution N(0,sigma)
tf = unifrnd(-60,60,Nf,1); % temporal center of each fluctuation,
                              distributing uniformly on [-60,60]
tl = tf - tau; % start time of each fluctuation
tr = tf + tau; % end time of each fluctuation
dphi = 0;
for i = 1:Nf
   dphi = dphi +h(i)*(sign(t-tl(i)) - sign(t-tr(i)))/2;
   % the phase noise
end
phi = phi0 + dphi; % the noisy phase
```

Bibliography

[1] C. M. Papadimitriou, *Computational Complexity*, Addison-Wesley, Reading, Massachusetts (1994).

[2] M. R. Garey and D. S. Johnson, *Computers and Intractibility*, W. H. Freeman and Company, New York (1979).

[3] R. Crandall and C. Pomerance, *Prime Numbers: A Computational Perspective*. Springer (2006).

[4] R. L. Rivest, A. Shamir, and L. M. Adleman, Comm. ACM **21**(2), 120 (1978).

[5] P. W. Shor, in *Proceedings,* 35^{th} *Annual Symposium on Foundations of Computer Science*, 124, IEEE Press, Los Alamitos, CA (1994).

[6] J. I. Cirac and P. Zoller, Phys. Rev. Lett. **74**, 4091 (1995).

[7] J. L. O'Brien, Science **318**(5856), 1567 (2007).

[8] N. A. Gershenfeld and I. L. Chuang, Science **275**, 350 (1997).

[9] A. A. Houck et al., Phys. Rev. Lett. **101**, 080502 (2008).

[10] M. A. Nielsen and I. L. Chuang, *Quantum Computation and Quantum Information*, Combridge University Press, Cambridge (2000).

[11] P. W. Shor, in *Proceedings,* 37^{th} *Annual Symposium on Fundamentals of Computer Science*, 56, IEEE Press, Los Alamitos, CA (1996).

[12] P. W. Shor, Phys. Rev. A **52**, 2493 (1995).

[13] https://en.wikipedia.org/wiki/Qubit

[14] J. S. Bell, *On the Einstein Podolsky Rosen Paradox* (1964).

[15] C.H. Bennet et al., Phys. Rev. Lett. **70**, 1895 (1993).

[16] A. Barenco et al., Phys. Rev. A **52**, 3457 (1995).

[17] E. Knill, arXiv:quantph/9508006.

[18] P. O. Boykin et al., arXiv: quant-ph/9906054,

[19] D. Gottesman, Ph. D. thesis, California Institute of Technology, Pasadena, CA (1997).

[20] E. Knill, R. Laflamme, and W. H. Zurek, Proc. R. Soc. Lond. A **454**, 365 (1998).

[21] D. Aharonov, Ph. D. thesis, The Hebrew Univesity, Jerusalem, (1999).

[22] D. Aharanov and M. Ben-Or, in *Proceedings of the Twenty-Ninth ACM Symposium on the Theory of Computing*, 176 (1997).

[23] A. Y. Kitaev, Russ. Math. Surv. **52**, 1191 (1997).

[24] A. Y. Kitaev, in *Quantum Communication, Computing, and Measurement*, 181, Plenum Press, New York (1997).

[25] P. Aliferis, Ph. D. thesis, California Institute of Technology, Pasadena, CA (2007).

[26] E. Knill, R. Laflamme, and W. H. Zurek, Science **279**, 342 (1998).

[27] J. Preskill, Proc. R. Soc. Lond. A **454**, 385 (1998).

[28] F. Gaitan, *Quantum error correction and fault-tolerant quantum computing*, CRC Press, Boca Raton, FL (2008).

[29] A. Y. Kitaev, arXiv:quant-ph/9707021.

[30] J. P. Palao and R. Kosloff, Phys. Rev. Lett. **89**(18), 188301 (2002).

[31] Robert F. Stengel, *Optimal control and estimation*, Dover Publications, Inc., New York (1994).

[32] I will spell out what I mean by "good approximation" in Chapter 3.

[33] Value functions can also be considered with optimal assignments producing maximum value.

[34] R. Li, M. Hoover, and F. Gaitan, Quantum Info. Comp. **7** 594 (2007).

[35] For our purposes, it is sufficient that $Q(t)$ be a positive Hermitian matrix.

[36] As will be discussed in Section 3.2 and 3.3, the numerical simulations transform the dimensionful Schrodinger equation into dimensionless form so that the time parameter in the simulations is dimensionless. When discussing Strategy 1 in Section 2.5.1 the time t is actually dimensionless time. Thus when I say that the one-qubit numerical simulations have $T = 160$ I am making a statement about the dimensionless time parameter. The connection between dimensionful and dimensionless parameters is explained in Section 3.2.

[37] R. E. Kalman and R. S. Bucy, J. Basic Engrg. **83**(1), 95 (1961).

[38] F. Gaitan, Phys. Rev. A **68**, 052314 (2003).

[39] J. W. Zwanziger, U. Werner-Zwanziger, and F. Gaitan, Chem. Phys. Lett. **375** 429 (2003).

[40] F. Gaitan, J. Mod. Opt. **51**, 2415 (2004).

[41] R. Li and F. Gaitan, Optics and Spectroscopy **99**, 257 (2005).

[42] R. Li, M. Hoover, and F. Gaitan, Quantum Info. Comp. **9** 290 (2009).

[43] R. Li and F. Gaitan, Quantum Info. Comp. **10**, 936 (2010).

[44] R. Li and F. Gaitan, J. Mod. Opt. **58**, 1922 (2011).

[45] A. Abragam, *Principles of nuclear magnetism*, Oxford University Press, New York (1961).

[46] F. Gaitan, J. Mag. Reson. **139** 152(1999).

[47] R. P. Feynman and A. R. Hibbs, *Quantum mechanics and path integrals*, McGraw-Hill, New York (1965).

[48] To achieve this level of gate performance required TRP sweep parameter values with 17-bits of precision. Ref. [43] modified the optimization cost function to reward both gate robustness and low error probability, and found TRP sweep parameter values that produced one-qubit TRP gates with $P_e < 4.62 \times 10^{-4}$, while only requiring sweep parameters with 14-bits of precision. This approach improved gate robustness at the cost of a small increase in the gate error probability. By showing how to inter-leave a TRP sweep with a suitable dynamical decoupling sequence, Ref. [44] was able to reduce the gate error probability for the two-qubit modified controlled phase gate to $P_e < 8.87 \times 10^{-5}$, while only requiring TRP sweep parameters with 14-bits of precision. This improved performance was achieved at the cost of a more complicated control field.

[49] The accuracy threshold theorem (ATT) requires $P_e < P_a$ for every application of a quantum gate. By defining P_e to be the worst-case value of $P_e(\psi)$ I insure that if $P_e < P_a$, then for every initial state ψ (and thus for every gate application), $P_e(\psi) < P_a$ as demanded by the ATT. However, if P_e is defined as an average-case value, states could exist for which $P_e(\psi) > P_a$ even though $P_e < P_a$. Such states would violate a core requirement of the ATT, and thus nullify its conclusion. It is not enough to satisfy the conditions of the ATT on average. Thus, in the context of fault-tolerant quantum computing, it is more appropriate to define the gate error probability as a worst-case value rather than as an average-case value.

[50] Note that Refs. [34]– [44] have a factor of two error in the quoted value of τ_0 for the one-qubit gates. The correct value for these gates is $\tau_0 = 160$, as given here.

[51] For example, the Agilent M8190A 12 GSa/s Arbitrary Waveform Generator provides 5 GHz bandwidth.

[52] For example, the Tektronix AWG5000B arbitrary waveform generator provides 14-bit vertical resolution.

[53] For example, the Tektronix AWG5000 arbitrary waveform generator has 5ps timing jitter.

[54] A. Steane, Phys. Rev. Lett. **78**, 2252 (1997); arXiv:quant-ph/9611027.

[55] D. Gottesman and I. Chuang, Nature **402**, 390 (1999); arXiv:quant-ph/9908010.

[56] E. Knill, quant-ph/0312190 (2003).

[57] E. Knill, quant-ph/0402171v1 (2004).

[58] E. Knill, Nature **434**, 39-44 (2005).

[59] See, for example, Ref. [10], pp. 25.

[60] Y. Zhang, *Advanced Quantum Mechanics*, Science Press, Beijing (2010), pp. 33.

[61] See Ref. [10], Section 11.3.

[62] P. Aliferis, D. Gottesman and J. Preskill, Quant. Inf. Comput. **8** (2008) 181-244.

[63] B. Reichardt, Algorithmica **55**(3), 517-556 (2009).

[64] W. H. Press, *Numerical recipes: The art of scientific computing, 3rd ed.*, Cambridge university press, NY (2007).

[65] The `Matlab` function `simulannealbnd` was used to find the dimensionless control parameter assignment that minimizes Eq. (4.22).

[66] Y. Peng and F. Gaitan, Phys. Rev. A **90**, 022311 (2014); arXiv:1407.8074.

[67] F. Gaitan, Int. J. Quantum Inform. **4**, 483 (2006).

[68] A. R. Calderbank, P. W. Shor, Phys. Rev. A **54**(2), 1098 (1996); A. Steane, Proc. Roy. Soc. Lond. A **452**, 2551 (1996).

[69] E. Dennis, A. Kitaev, A. Landahl, and J. Preskill, J. Math. Phys. **43**, 4452 (2002).

[70] R. Raussendorf and J. Harrington, Phys. Rev. Lett. **98**, 190504 (2007).

[71] H. G. Katzgraber, H. Bombin, and M. A. Martin-Delgado, Phys. Rev. Lett. **103**, 090501 (2009).

[72] D. S. Wang, A. G. Fowler, C. D. Hill, and L.C.L. Hollenberg, Quant. Inf. Comp. **10**, 780 (2010).

[73] J. Ghosh, A. G. Fowler, and M. R. Geller, Phys. Rev. A **86**, 062318 (2012).

[74] J. W. Zwanziger, S. P. Rucker, and G. C. Chingas, Phys. Rev. A **43**, 3232 (1991).

[75] J. B. Thomas, *Statistical Communication Theory* (Wiley, New York, 1969).

[76] F. Rief, *Fundamentals of Statistical and Thermal Physics*, McGraw-Hill, New York (1965).

[77] A. W. Drake, *Fundamentals of Applied Probability Theory*, McGraw-Hill, New York (1967).

[78] S. O. Rice, Bell Sys. Tech. J. **23**, 282 (1944).

[79] See Ref. [78], Section 1.3.